Politecnico di Torino

Master's Degree in Mechanical Engineering

a.y. 2023/2024

Graduation session October 2024

Computational analysis of a confined capillary interface under the influence of a perturbative rotating impulse

Supervisors:
Prof. Domenic D'Ambrosio
Prof. Francisco Cruz Mazo

Candidate:
B.Sc. Livio Michele Mösch

Abstract

The following thesis discusses two separate microfluidic applications analysed with ANSYS Fluent 2022R1.

For a rotating capillary tube of a diameter of 2 mm and height of 10 mm that is filled with air on the top half and water on the bottom half ($Bo_g = \frac{\Delta \varrho g L^2}{\sigma} \approx 0.543$) applying different rotational velocity profiles to the cylinder wall was found to not have a significant impact on the fluid interface. The geometry was replicated with a 2D axisymmetric model and analysed with and without the effect of gravity, trying different stabilization methods and settings. For constant time stepping the instability region was identified, for adaptive time stepping the results showed an almost complete independence from the imposed wall speed. To instable setups the addition of stabilization mechanisms strong enough to overcome known issues within the software led to unphysical results. A liquid combination with densities and viscosities lying closer to one another showed a similar behaviour. It was not possible to replicate the results leading to this research showing capillary breakup through different mode shapes and thereby an aerosol formation. The methods to possibly replicate the simulations, also in a three-dimensional approach, were elaborated.

For a glass substrate of a diameter typical for the semiconductor industry of 40 mm, the apparent contact angle between the liquid droplet and solid was estimated from literature and simulations performed for both cases of static and dynamic spin coating. By rotating around 0.1 s all three analysed liquids being Oil, Water, and Ethanol were entirely spun off the surface without leaving a liquid film behind. A method to quantify the maximum radial extension of the fluid as well as the angle of the liquid-air interface through Fluent macros and MATLAB was presented. It was found that for the same angular speed ω and rotational Bond number Bo_r Water droplets are the most prone to fingering instabilities, followed by Ethanol and then Oil. This phenomenon was characterized through three dimensionless numbers describing the problem, being Bo_r, We and Oh. While the island detachment in fingering instability seems to be independent of Oh in the static case, there was found to be optimization potential in terms of combinations of Bo_r and We in the dynamic one. Higher angular speeds generally lead to quicker detachments, while the right droplet impact velocities could be able to counter this effect. The initial phase of the liquid spreading was found to depend solely on We, hence being uncoupled from the substrate's angular speed. The specific interval of $10^1 < Bo_r < 10^3$ was elaborated for static spin coating with Ethanol droplets of different diameters at varying angular speeds. The obtained results within this interval present a good fit with dimensionless results from previous experimental data. They also point towards a horizontal shift of the curves relating the dimensionless diameter to Bo_r for the same liquid at different rotational speeds.

Acknowledgements

Contents

List of Figures

List of Tables

Acronyms

VOF	Volume of fluid
CFL	Courant-Friedrichs-Lewy
ν_t	Turbulent viscosity
C	Courant number
rpm	Revolutions per minute
MRF	Moving reference frame
ADSA	Axisymmetric Drop Shape Analysis
TUI	Text-user-interface

Subscripts and Superscripts

acc	acceleration
rot	rotational
ts	time step
g	gravitational
char	characteristic
eq	equilibrium
dyn	dynamic
adim	dimensionless

0. Introduction

This research-based thesis work consists of two parts

i.   The determination of rotational acceleration patterns leading to capillary breakup within a tube filled with two different fluids

ii.   The investigation of the dynamics of a sessile droplet spreading on a spinning plate with constant rotational speed, e.g. in the process of spin coating

The first investigated problem is based on results obtained by Prof. F. Cruz Mazo which currently still underly an embargo as they are in the process of getting published in a high-profile paper. They presented a great opportunity for a research-based thesis, but the replicability was in question from the start and in the end led to significant complications which will be explained in their dedicated chapters.

The second problem aims to get insights on the dynamics of spin coating processes in terms of the dimensionless Bond, Ohnesorge, and Weber numbers. The results are compared to literature and show promising behaviour.

Both are performed as VOF simulations using the commercial finite volume solver ANSYS Fluent. To be able to gain a substantial amount of understanding of the applied equations and made considerations it will be necessary to consult and discuss some literature.

1. Convective breakup in a capillary tube

The first part is based on the analysis of a capillary tube filled partially with a liquid, and partially with air. This tube filled with two fluid phases is accelerated by turning it around its main axis applying different velocity profiles as portrayed in Figure 1 and Figure 2.
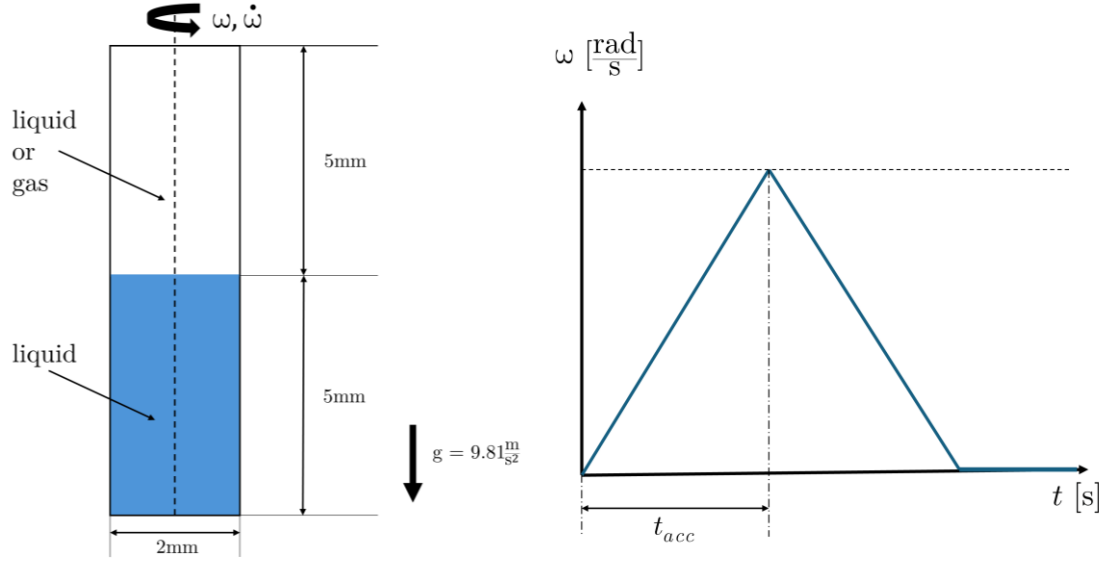
Figure 1: 2D representation of the capillary tube   Figure 2: Generic applied velocity profile

This is done in order to try to achieve different mode shapes dominating the fluid surface, ultimately expecting to lead to convective breakups of fluid droplets which can be used in various applications as e.g. aerosols. The scientific basis for this analysis is given by research performed by Prof. F. Cruz Mazo, who was able to simulate different mode shapes and breakups using self-developed code based on the motion equations explained in the following paragraphs.

In essence, to resolve the flow field under the hypothesis of incompressibility and ignoring effects of temperature we need to solve the continuity equation

$$\nabla \cdot \boldsymbol{v} = 0 \tag{1}$$

as well as the momentum equation

$$\varrho \frac{\delta \boldsymbol{v}}{\delta t} + \varrho(\boldsymbol{v} \cdot \nabla)\boldsymbol{v} = -\nabla p + \mu \nabla^2 \boldsymbol{v} + \varrho \boldsymbol{v} + \boldsymbol{f}_i \tag{2}$$

The crucial part for the modelling the effect of the spinning outer wall on the fluids is the addition of the inertial force term $\boldsymbol{f}_i$. This force per volume is based on the rotational acceleration $\overrightarrow{a_{\text{rot}}}$, experienced by the fluid due to the moving walls and can be expressed as follows [1]

$$\overrightarrow{a_{\text{rot}}} = \underbrace{-\overrightarrow{\omega_{\text{rot}}} \wedge \overrightarrow{\omega_{\text{rot}}} \wedge \overrightarrow{r_{radial}}}_{acc_{\text{Centripetal}}} - \underbrace{\frac{d\overrightarrow{\omega_{\text{rot}}}}{dt} \wedge \overrightarrow{r_{radial}}}_{acc_{\text{Coriolis}}} \qquad (3)$$

The part related to the Coriolis-acceleration leads to the conclusion that it must be dealt with non-symmetrical accelerations and hence forces.
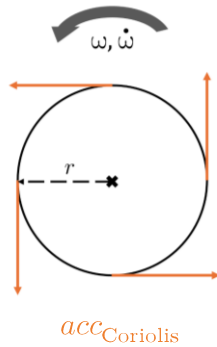
As the acceleration is

1. $\perp$ to the angular velocity of the rotating tube
2. $\perp$ to $\overrightarrow{r_{radial}}$

The code developed specifically for this analysis was neither presented nor explained to me, as its complexity would have gone far beyond the scope of a M.Sc. thesis. As a matter of fact, this first part of the thesis is concerned with trying to replicate these mathematical results through simulations with the commercial finite volume solver ANSYS Fluent 2022R2/2024R1, where all these considerations should be correctly implemented over the imposed boundary conditions.

The goal of this work was to investigate the different mode shapes of different fluid combinations (e.g. air-oil, oil-water, water-oil...) by changing the power energy inserted into the system, being the integral under the curve portrayed in Figure 2. Due to reasons connected with copyright and publishing procedures, these not yet published results obtained by Prof. F. Cruz Mazo cannot be presented in this work. In an effort to depict the expected results, Figure 3 lists three exemplary situations. It should be noted that the liquid combination and top-bottom orientation can vary with respect to the example in Figure 2; as a matter of fact exploring the difference between e.g. oil on top and water on the bottom, as well as water on the top and oil on the bottom with the gravity always pulling from top to bottom was a central part of the investigation. For this reason, the sketch shows only the interface between two arbitrary fluids.
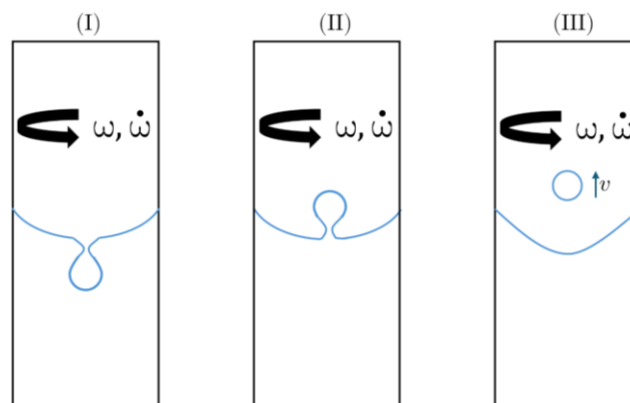
Figure 3: Exemplary depiction of two possible mode shapes (I) and (II) as well as an example of capillary breakup into an aerosol (III)

1.1. Solver settings

The idea is to track the liquid-gas interface throughout the acceleration and deceleration of the tube. As the two fluids are regarded as immiscible, the Multiphase "Volume of Fluid" (VOF) method allows us to solve a single set of momentum and continuity equations and through the addition of a surface reconstruction algorithm track the volume fraction of each of the fluids [2]. This method which is based on a Eulerian approach is preferred as the mathematical formulation explicitly captures the fluid interface, that in our case is clearly defined and the centre of the analysis. It is also less complex than the full Eulerian model which solves a set of n momentum and continuity equations for each of the n phases and couples them accordingly to the chosen scheme and interface exchange coefficients [2]. To be able to justify our assumptions and interpret the results, it is important to understand and outline the governing equations and followed numerical procedure.

1.1.1. Solution method of the transient VOF model

The volume fraction of each of the q phases within a cell volume is defined as α_q. Through this formulation the variables and properties of each cell can be expressed by adjusting them according to their respective volume fraction.

- $\alpha_q = 0$: There is no q^{th} fluid in the cell
- $\alpha_q = 1$: There is only q^{th} fluid in the cell
- $0 < \alpha_q < 1$: The cell contains the interface between the qth fluid and the other(s)

Applying this, the continuity equation can be written as

$$\frac{1}{\varrho_q}\left[\frac{\delta}{\delta t}\left(\alpha_q \varrho_q\right) + \nabla \cdot \left(\alpha_q \varrho_q \overrightarrow{v_q}\right) = S_{a_q} + \sum_{p=1}^{n}\left(\dot{m}_{pq} - \dot{m}_{qp}\right)\right] \tag{4}$$

In our case the source term is zero, and m_{pq} referring to the mass flow from the liquid to the air phase, m_{qp} the other way round, also zero. To be able to use the "most accurate" [2] interface modelling scheme called "GEO-reconstruct" based on a geometric reconstruction approach, picking the explicit formulation for the solver is strictly necessary within the software [3].

$$\frac{\alpha_q^{n+1}\varrho_q^{n+1} - \alpha_q^n \varrho_q^n}{\Delta t} V + \sum_f \left(\varrho_q U_f^n \alpha_{q,f}^n\right) = 0 \tag{5}$$

Where

$\alpha_{q,f}$	Face value of the qth volume fraction
U_f	Volume flux through the face, based on normal velocity
V	Volume of the cell

As here each new step only depends on the current state, the explicit method involves one arithmetic operation, making it less computationally intensive per step. The drawback though is that usually smaller timestep sizes are required, as a calculation based only on the previous condition requires the Courant-Friedrichs-Lewy condition to be respected. This condition generally states that the timestep must be below a certain threshold given a spatial increment generally defined through the flow speed and grid size and will be further elaborated in the following. This simulation was performed setting a maximum of 40 iterations per timestep (the solution might converge earlier), despite using an explicit formulation. This helps to increase numerical stability and accuracy even further by decreasing residuals. As the total simulation time lies around one second, considering the computational power provided by the University, these choices were considered suitable at the time of choosing.

To calculate the velocity field in the first place, a single momentum equation in incompressible form is solved for the whole domain, the resulting velocity field is shared among the two phases, and subsequently coupled to the continuity equation through a PISO algorithm. It will be dependent on the volume fractions α_q of both phases through the density ϱ and viscosity μ/ν [2] depending how the Navier-Stokes equation gets written. This so-called shared fields approximation may lead to a less accurate computation of velocities near the interface if the velocities between the two phases are very different from one another [2]. It is thus a general limitation of Fluent's implementation of the VOF model that has to be considered when troubleshooting. To be coherent in the following explanation the formulation used in [4] will be utilized.

$$\frac{\partial \boldsymbol{v}}{\partial t} + \boldsymbol{v}(\nabla \boldsymbol{v}) = \nu \nabla \cdot (\nabla \boldsymbol{v}) - \frac{1}{\varrho} \nabla p - \boldsymbol{g} + \frac{1}{\varrho} \boldsymbol{F} \tag{6}$$

The momentum equation is solved based on the RANS approach. Here the flow variables being pressure and velocity are split into an average and fluctuating value.

$$p = \overline{p} + p' \tag{7}$$

$$v = \overline{v} + v' \tag{8}$$

Where the mean values are evaluated through the temporal averaging

$$\overline{p}(t) = \frac{1}{\Delta t} \int_{t-\frac{\Delta t}{2}}^{t+\frac{\Delta t}{2}} p(t^*) dt^* \tag{9}$$

and analogously

$$\overline{v}(t) = \frac{1}{\Delta t} \int_{t-\frac{\Delta t}{2}}^{t+\frac{\Delta t}{2}} v(t^*) dt^* \tag{10}$$

To consider the Navier-Stokes equation on a large time scale, the equations (7) and (8) are substituted into (6) and then the entire equation is averaged [4]. The algebraic

transformations and considerations needed to perform them in are omitted in the scope of this work, and the result, which is relevant for the further passage, is discussed.

$$\frac{\partial \overline{\boldsymbol{v}}}{\partial t} + \overline{\boldsymbol{v}} \cdot (\nabla \overline{\boldsymbol{v}}) + \nabla \cdot \left(\overline{\boldsymbol{v}'\boldsymbol{v}'}\right) = \nu \nabla \cdot (\nabla \overline{\boldsymbol{v}}) - \frac{1}{\varrho}\nabla \overline{p} - \boldsymbol{g} + \frac{1}{\varrho}\boldsymbol{F} \tag{11}$$

The only undefined term is $\nabla \cdot \left(\overline{\boldsymbol{v}'\boldsymbol{v}'}\right)$ containing a product of non-averaged values. In other words it is responsible for the dissipation of impulse differences between fluid particles, meaning faster ones get slowed down and slower ones accelerated, hence acting as a type of friction [4]. We can consequently parametrize this term in a manner to bring the small-scale effects onto a global scale

$$\nabla \cdot \left(\overline{\boldsymbol{v}'\boldsymbol{v}'}\right) = -\nu_t \nabla \cdot (\nabla \overline{\boldsymbol{v}}) \tag{12}$$

Here ν_t represents a parametrized turbulent viscosity, ultimately allowing to write the completed form of the RANS equation as

$$\frac{\partial \overline{\boldsymbol{v}}}{\partial t} + \overline{\boldsymbol{v}}(\nabla \overline{\boldsymbol{v}}) - (\nu + \nu_t)\nabla \cdot (\nabla \overline{\boldsymbol{v}}) = -\frac{1}{\varrho}\nabla p - \boldsymbol{g} + \frac{1}{\varrho}\boldsymbol{F} \tag{13}$$

There are plenty different ways to describe ν_t and close the RANS equations, the most commonly used ones are approaches based on the findings and assumptions of Boussinesq in 1877, finally developed into zero/one/two equation models that are now usable in CFD software [5]. As far as the cases analysed in this work are concerned, choosing an appropriate model was not necessary, as the assumption of laminar flow had been made from the beginning.

The surface tension will be implemented into the problem as a source term in the momentum equation according to the Young-Laplace equation relating the pressure drop across the surface to the surface tension coefficient σ and the surface curvature measured by radii in two orthogonal directions R_1 and R_2 [2]

$$p_2 - p_1 = \sigma \left(\frac{1}{R_1} + \frac{1}{R_2}\right) \tag{14}$$

In Fluent this is called the "Continuum Surface Force Model".

1.1.2. Residuals

The topic of residuals itself is a non-trivial dive into the numerical schemes used to compute the transport, continuity and in this case also swirl equation. CFD solvers like Fluent use an iterative approach for the solution solving matrices which follows a similar pattern for the flow variables ϕ

$$\boldsymbol{A}\,\phi - \boldsymbol{B} = r \tag{15}$$

Where $\boldsymbol{A}$ and $\boldsymbol{B}$ are matrices depending on the specific equation and boundary conditions, and ϕ the vector of the flow variable that the algorithm is trying to solve. The residual vector

r will correspond to how much the current solution vector ϕ does not match the exact solution yet. Fluent then scales these residuals with respect to the biggest residual obtained within the first five iterations. This makes the residuals dependent on the initial values which can have advantages and disadvantages.

$$R_{\text{scaled}} = \frac{R_{\text{Iteration}_\text{N}}}{\max\left(R_{\text{Iteration}_{1-5}}\right)} \tag{16}$$

The value of this scaled residual was set to 10^{-5} for all the performed simulations, which is significantly lower compared to the standard value proposed by Fluent at 10^{-3} [2]. We want to assure that the solution iteratively converges to this tolerance within the maximum of 40 iterations per time step also imposed by us.

1.1.3. Spatial discretization near the interface / Geometric reconstruction

When a cell is completely filled with one phase or the other, Fluent's standard interpolation schemes are being used to calculate the convection and diffusion fluxes through the control volume [2], being a second-order upwind scheme for the momentum equation in our case. This is necessary as the flow variables φ are stored in the cell centre, but face values φ_f are required for the calculation of convective terms and have hence to be interpolated.

In the used geometric reconstruction approach, Fluent uses a special interpolation mechanism for cells near the interface between two phases. In essence, Fluent follows an approach proposed by Youngs in 1982 [6] where the volume fractions of nine cells are used to determine the slope of the interface in the centre cell.
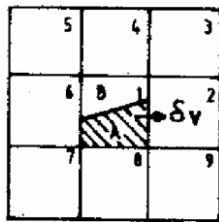
Figure 4: Cell in question with 8 surrounding ones [6]
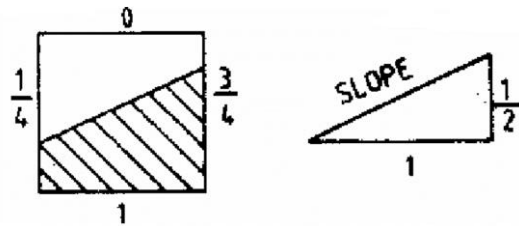
Figure 5: Example of calculated side fractions and slope [6]

Neither the paper cited by the Theory Guide that should explain the background nor the Theory Guide itself describe clearly and fully how the algorithm is carried out in total. For the sake of this work, it is important to note that this method will reconstruct the real interface with straight lines in each cell, which is of substance for the interpretation and computation of inclination angles described in the following chapters. Again, Fluent explicitly states that this is the "most accurate" [2] scheme for interface modelling available, making it the obvious choice for this work.

The specific settings applied here were keeping the Local Courant-Number at the predefined value of 0.25 as well as keeping the cutoff for the calculation of the volume fraction at 1e-6.

1.1.4. Temporal discretization

As already mentioned, the transient formulation of the problem paired with the explicit formulation requires the CFL condition to be respected [7]. It assures that the information in terms of flow variables within a cell travels no further than to the directly neighbouring cell within one time step. Forgetting to assure that might result in straight up wrong solutions and possibly divergence.

$$C = \frac{u\Delta t}{\Delta x} = \frac{\Delta t}{\Delta t_{\text{char}}} \leq 1$$

(17)

For the analysis performed in this work, the Global Courant number which is used for solving the transport equations was set to 0.9 down from the default 2. The default setting for the Local Courant number at 0.25 was kept. The time step for the VOF Geometric Reconstruction calculations done close to the interface is hence lower, leading to a number of sub time steps of almost four. When adaptive time stepping has been, used Fluent automatically adjusts the time step size for the transport equations according to this criterion; with manual time stepping, it must be ensured beforehand that the time step is below this criterion even in the worst-case scenario. Significant complications have come up when performing the simulations regarding this topic and are discussed in the following chapters.

1.1.5. Implementation of swirl components

By setting a symmetry axis as described in 1.2 Boundary conditions we can make use of the axisymmetric swirl option. With our circumferentially symmetric geometry this allows us to model the out-of-plane swirl velocities, under the assumption that there are no circumferential gradients within themselves. The addition of this equation to the momentum equations is described in Fluent's Theory Guide where it is also stated explicitly for the case of flows driven by wall rotation and is executed automatically when choosing an axisymmetric swirl problem.

$$\frac{\delta}{\delta t}(\varrho w) + \frac{1}{r}\frac{\delta}{\delta x}(r \varrho v w) = \frac{1}{r}\frac{\delta}{\delta x}\left[r\mu\frac{\delta w}{\delta x}\right] + \frac{1}{r^2}\frac{\delta}{\delta r}\left[r^3\mu\frac{\delta}{\delta r}\left(\frac{w}{r}\right)\right] - \varrho\frac{vw}{r}$$

(18)

Where

x	Axial coordinate
r	Radial coordinate
u	Axial velocity
v	Radial velocity
w	Swirl velocity

1.2. Boundary conditions

The boundary conditions used are best represented with a full sketch, as displayed in Figure 7. The two-dimensional representation already presented before is added to highlight that the full computational domain is the green area shown in Figure 6. The wall rotates around the symmetry axis with a varying angular speed ω. The contact angle between the fluids and the wall must be set in advance and was chosen as $\frac{\pi}{4} = 45°$ [1]. The static pressure at the outlet is set to relative 0bar, the symmetry axis is the x-axis at $y = 0$.
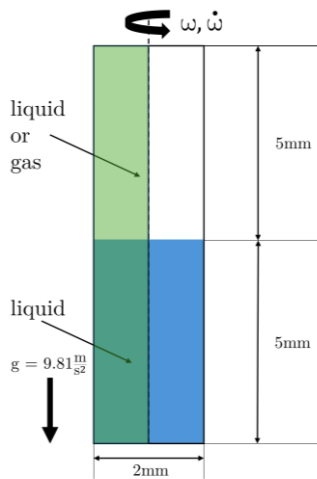
Figure 6: Green part represents the calculation domain
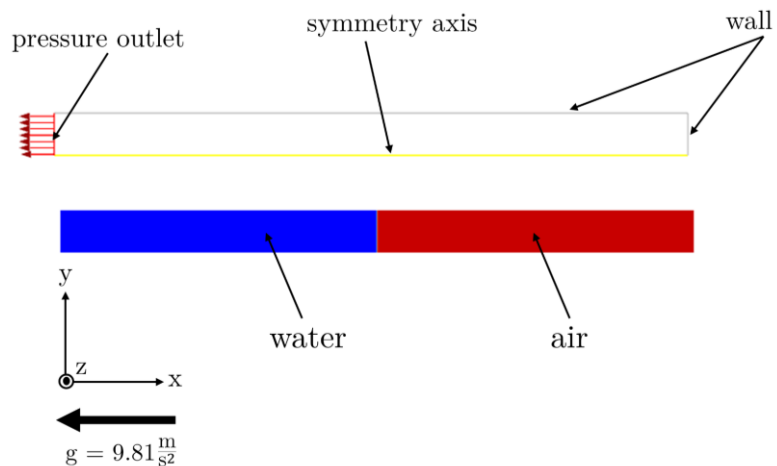
Figure 7: Full calculation domain with boundary conditions, direction of gravity, and fluid filled parts of the tube

The symmetry condition leads to an advantage and a disadvantage: whilst the computational time needed for the simulation, which for VOF simulations is directly related to the total cell number [2], should decrease significantly, the ability of the simulation to factor in eventual asymmetrical effects around the rotating axis is taken away. As the results leading to this research lead to believe that there could be some asymmetrical effects, the first goal was to try to run the simulation without implying an axis symmetry. Unfortunately, after various different attempts trying to work around Fluent's limitations, it became apparent that this was not possible when opting for a rotating wall. The computational domain is two-dimensional, and the rotation implies a swirl around the rotational axis with velocities outside of the 2D $x - y$ plane. Imposing this through a rotating wall in Fluent is possible, but solely for rotations around an axis of symmetry which will always have to be the x-axis with the full calculational domain being above $y = 0$. Due to this trying to replicate the full geometry by laying a part of it below the y-axis or setting a different origin of the axis is not possible when setting the wall as rotating [3]. If non-axis symmetric swirl is chosen, Fluent will automatically rotate the body around the z-axis. Trying to do a workaround like setting up the geometry in the xz plane was tried but does not work, as during the integration of the Mesh the solver will simply interpret the z-axis as the y-axis to conform with the 2D formulation.

1.3. Meshing

To achieve significant results reaching a time step and mesh independence is crucial. For cases like this the general approach could be to track at least one local and one global flow variable and check how they behave with decreasing time steps and mesh sizes. Before this, a general approach of meshing needs to be selected. As the zone of interest lies around the interface in the centre of the domain, this part has been equipped with a higher concentration of cells, while the outer parts have been chosen coarser to save computational time. Apart from the region where the tighter mesh merges into the coarser one, the cells were set as perfect squares in an effort to optimize mesh metrics. The final result can be viewed in Figure 8, Figure 9 and Figure 10.

Figure 8: Mesh of the full computational domain as shown in Figure 7
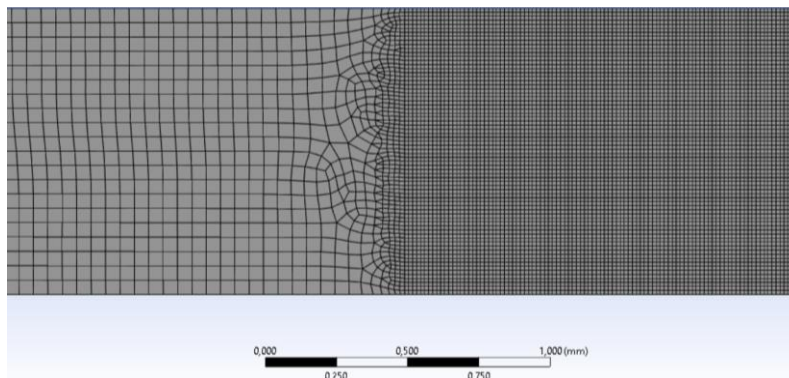
Figure 9: Zoomed in part of the transition zone
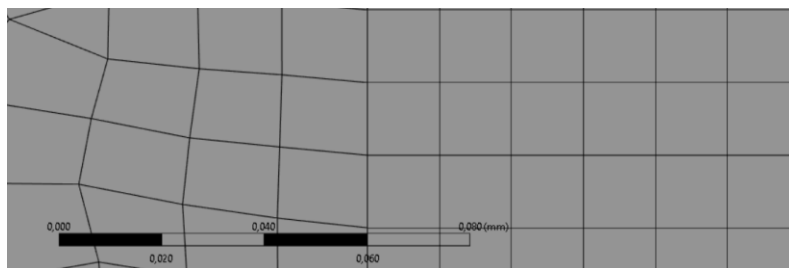
Figure 10: Zoomed in part of the transition zone for size comparison; central cells have a side length of 15 µm

This leads to a mesh with a total cell count of 29942 which is the highest possible value given the computational power, a minimum orthogonal quality of 0.529, and a maximum aspect ratio of 5.372. While these values that should both lie as close to one as possible are not optimal, their location is in one of the bigger skewed cells in the boundary region between the fine resolution in the middle and the coarser outer part. In the actual interface area of interest where the mesh consists of solely perfect squares the mesh metrics orthogonal quality, aspect ratio and skewness are ideal.

1.4. 2D Simulations

After the solver settings, boundary conditions and the mesh have been decided on, preliminary simulations were conducted. These solutions were tried to be further refined in the process.

1.4.1. Without wall rotation

As an initial approach the motion of the fluid within the stationary capillary tube was analysed. To be able to get a feeling of what happens on a more macroscopic timescale, the simulation was set up in a manner to see the effect of gravity empty out the whole capillary tube. Experiments on flow times in capillary tubes with and without the effect of gravity have been carried out extensively, but mostly investigate time needed for the capillary force to drag the fluid into the tube, with or without the effect if gravity [8], [9]. Carrying out a small experiment to check the numerical results would have been desirable but was not possible at the time due to the lack of laboratory equipment.

Table 1: Data of used fluids at 25 °C [10]

Physical quantity	Water	Air
Density ϱ	$998.2\,\frac{\text{kg}}{\text{m}^3}$	$1.225\,\frac{\text{kg}}{\text{m}^3}$
Surface tension coefficient σ	$0.072\,\frac{\text{N}}{\text{m}}$ [11]	
Dynamic viscosity μ	$0.001003\,\frac{\text{kg}}{\text{ms}}$	$1.7894\text{e-}05\,\frac{\text{kg}}{\text{ms}}$

At this part another consideration that needs to be made in the boundary conditions has to be stated. As in this case the bottom part is open and there is no water reservoir beneath it, it can be assumed that the gravity will pull the water out of the tube until it is completely filled with the surrounding air. However, as we're dealing with capillary forces at low speeds, it is possible that there will be some sort of backflow at the designated pressure outlet; this is not an issue and known to Fluent for cases of capillary VOF simulations [2]. The backflow material itself needs to be specified in the software in advance and was set as air in this case. This is since the experimental setup would've led to the same thing and some choice had to be made. This backflow can be seen at the outlet on the bottom at some instants, but should not influence the interface which is the zone most interesting for the analysis too much, as the computational domain was chosen bigger on purpose to mitigate such effects.

These preliminary calculations were performed using adaptive time stepping, which automatically adjusts the time step based on the given Courant number, depending on mesh size and flow speeds. They were performed on a full calculational domain that was not more

refined towards the centre and had a cell grid of about 65 µm × 65 µm. This mesh and setup was later discarded due to Fluent's limitations to set a moving wall with this geometry described in 1.2 Boundary conditions. The results were still regarded as useful, as they give the opportunity to compare the result from the symmetric setup with the full 2D domain.

Please note that the lighter fluid (air, in a last case oil) is henceforth always the phase on top, while water is the phase on the bottom.
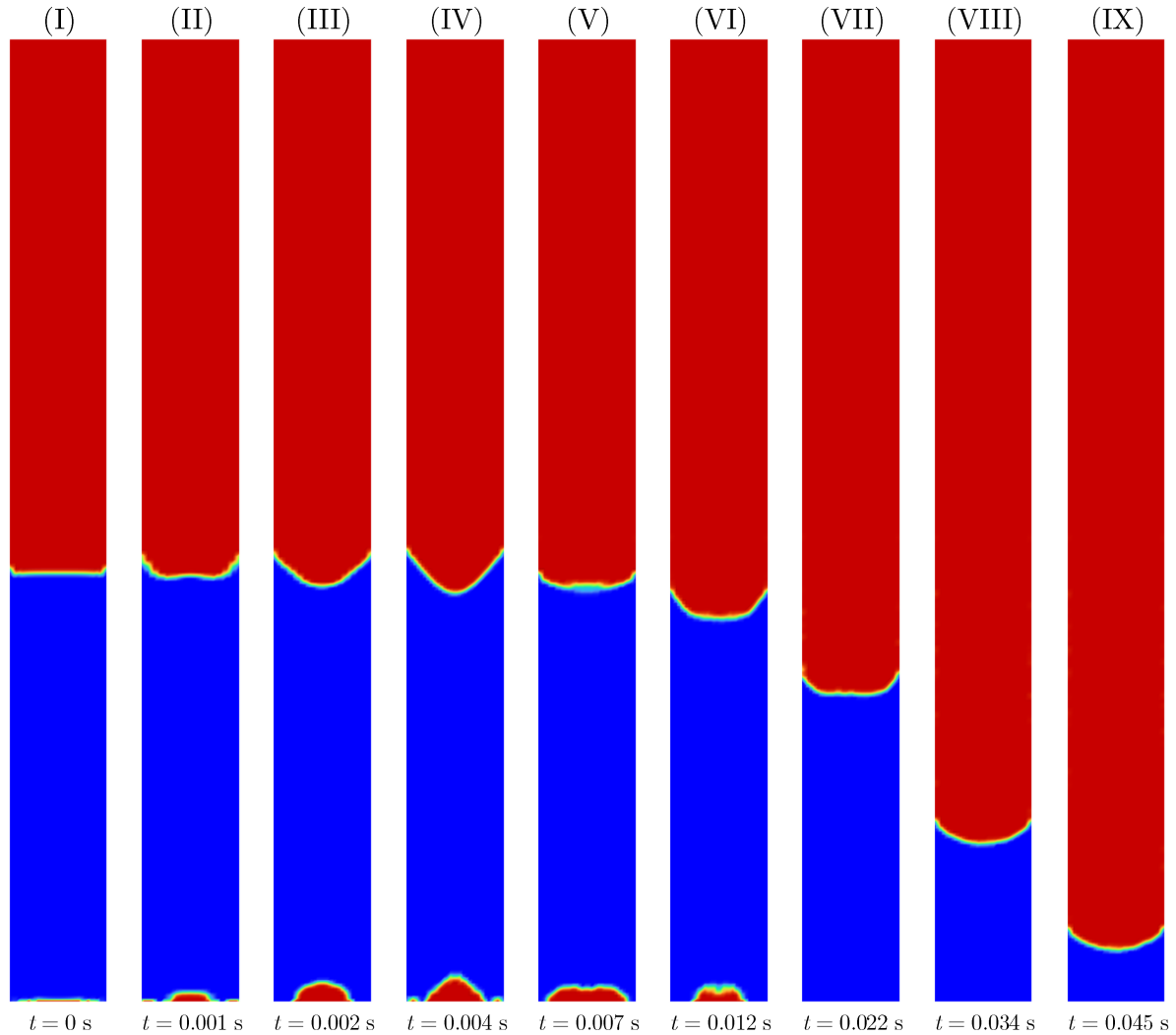
Figure 11: Transient simulation results of a stationary capillary tube ($\omega = 0$ rad/s); blue is water, red is air

At the initial condition $t = 0$ s the water and air domains are split by a straight line, while at $t = 0.001$ s the cells right next to the wall show the imposed contact angle with the wall as well as some rising of the liquid borders due to capillary forces. The central part performs a sort of wave pattern between $t = 0$ s and $t = 0.002$ s which will be analysed more in detail later. During and after this it can be observed that the central part continues to undulate up and down with decreasing amplitude, whilst the contact point of the liquid with the walls moves down continuously. Starting from around $t = 0.032$ s this undulation becomes even less dominant, after around 0.052 s the 5 mm of water column left the capillary tube completely apart from some droplets shooting up the wall due to numerical struggles.

Now the next step is the analysis of the interface in a more precise manner by using a mesh refined in the centre and the symmetric half-domain as shown in Figure 8. Preliminary tests showed that with this mesh the software adjusts the time step to minimum values of around $\Delta t_{ts} = $ 2.4e-5 s and settles around $\Delta t_{ts} = $ 6e-5 s based mainly on the CFL condition, so setting a constant time step of $\Delta t_{ts} = $ 1e-5 s seemed like a conservative approach allowing an even finer temporal resolution and allowing better post-processing. This allowed for a fine temporal resolution around the part of the initial wave undulation taking around 1ms of 100 time steps per millisecond, necessary to display the transient phenomenon in question. As expected, a significant increase in computational time was experienced. The results from the halved calculation domain can be pasted together in postprocessing, creating an axisymmetric end result showing the entire tube instead of only one half for better clarity.
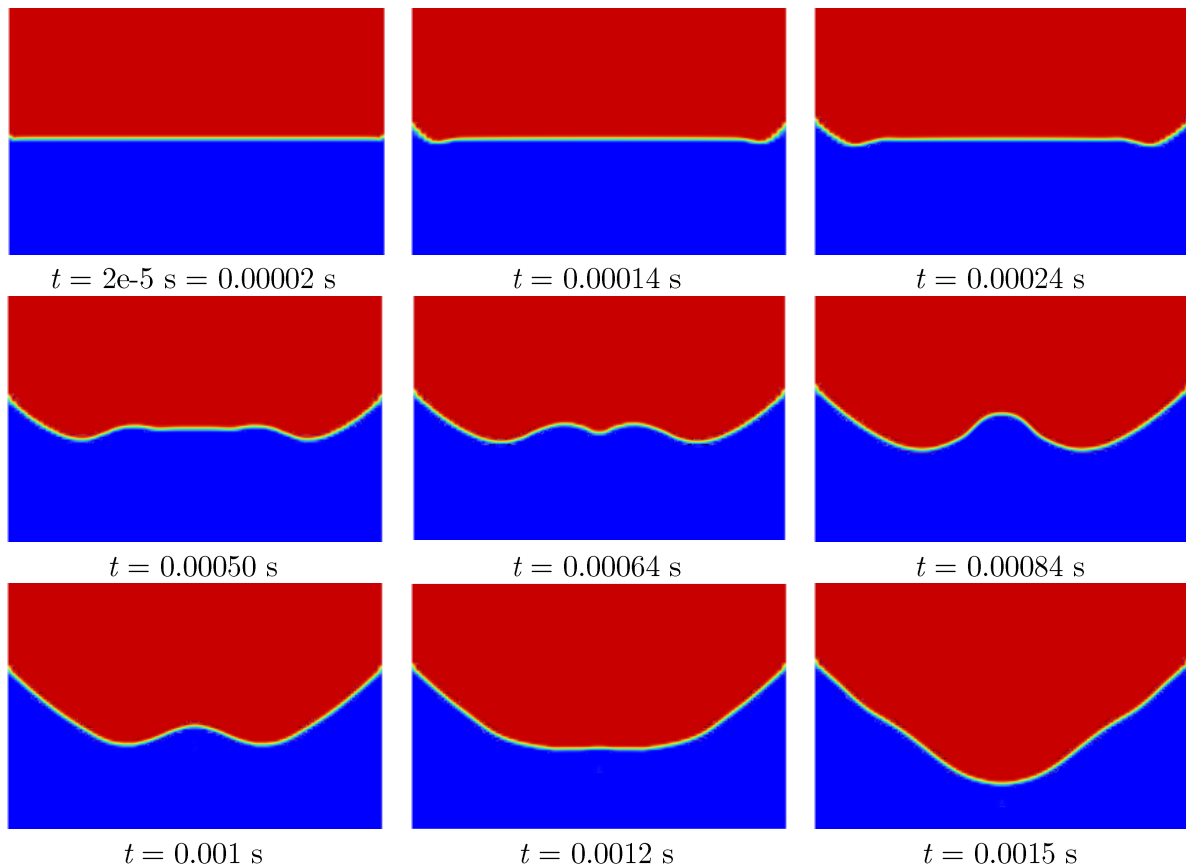
Figure 12: Close up of more refined transient simulation results of a stationary capillary tube ($\omega = 0$ rad/s); blue is water, red is air

These initial results were quite promising. A gradual buildup of liquid towards the centre is visible, with two separate peaks around $t = 0.00064$ s. They then combine each other leading to the buildup of one main peak that reached its maximum height around $t = 0.00084$ s. After this the peak flats out, and the surface transforms into a convex shape. This lead to believe that perhaps by inserting energy in terms of rotational acceleration capillary breakup as described in the beginning in Figure 3 could be possible, and hence further investigations were conducted.

To further characterize our flow some dimensionless numbers were examined for this specific case, namely being the Bond and Ohnesorge numbers. In general, a high value of the Bond number indicates that a two-phase flow is strongly affected by the gravitational body force and little affected by surface tension [12]

$$Bo_g = \frac{\Delta \varrho g L^2}{\sigma} = \frac{997 \frac{\text{kg}}{\text{m}^3} \cdot 9.81 \frac{\text{m}}{\text{s}^2} \cdot \ 0.002 \text{m}^{\ 2}}{0.072 \frac{\text{N}}{\text{m}}} \approx 0.543 \tag{19}$$

As we are left with a Bond number of 0.543 which is relatively low, the flow should be mainly driven by the surface tension and less by the gravitational force. Repeating the setup from Figure 12 with the difference of barring the gravitational force from the momentum equations supports this consideration.

$t = \text{2e-5 s} = 0.00002$ s $t = 0.00014$ s $t = 0.00024$ s

$t = 0.00050$ s $t = 0.00064$ s $t = 0.00084$ s
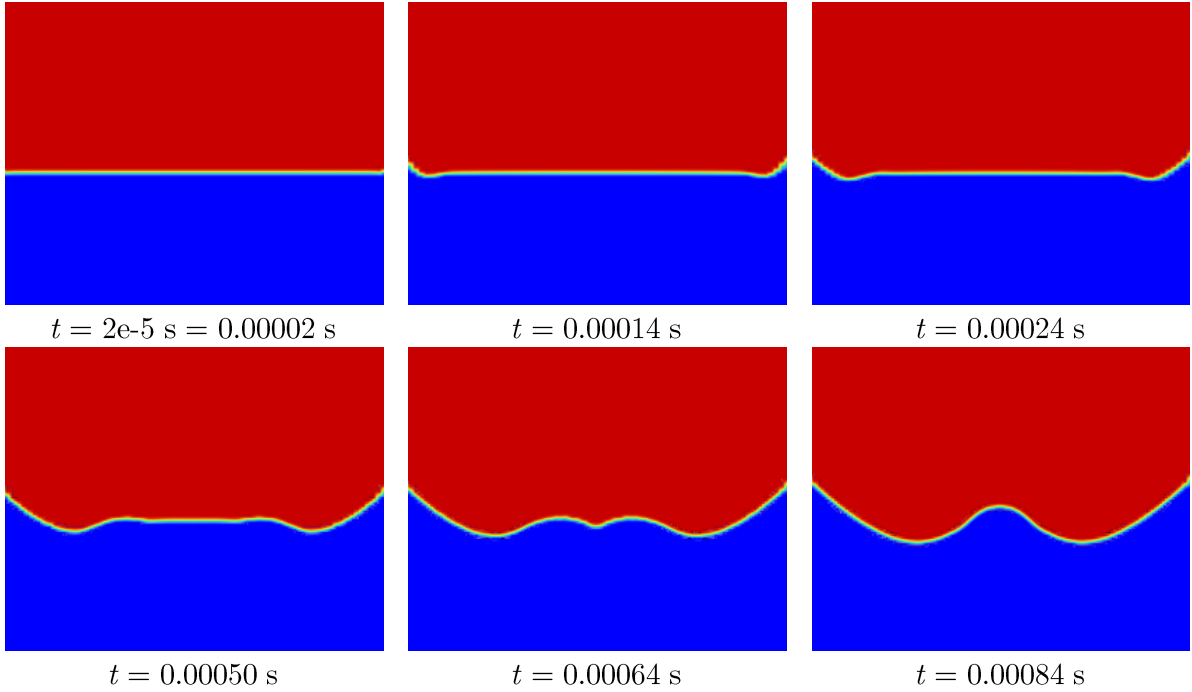
Figure 13: Close up of more refined transient simulation results of a stationary capillary tube ($\omega = 0$ rad/s) setting the gravity to 0 m/s²; red is air, blue is water

The initial phase most important for this work behaves similarly to the solution where the gravitational force is added. Compared to the case with gravity, the peak at $t = 0.00084$ s seems to have a bigger curvature radius and the symmetry at $t = 0.00064$ s also seems to behave slightly differently.

$$t = 0.022 \text{ s}$$

$$t = 0.036 \text{ s}$$

$$t = 0.054 \text{ s}$$
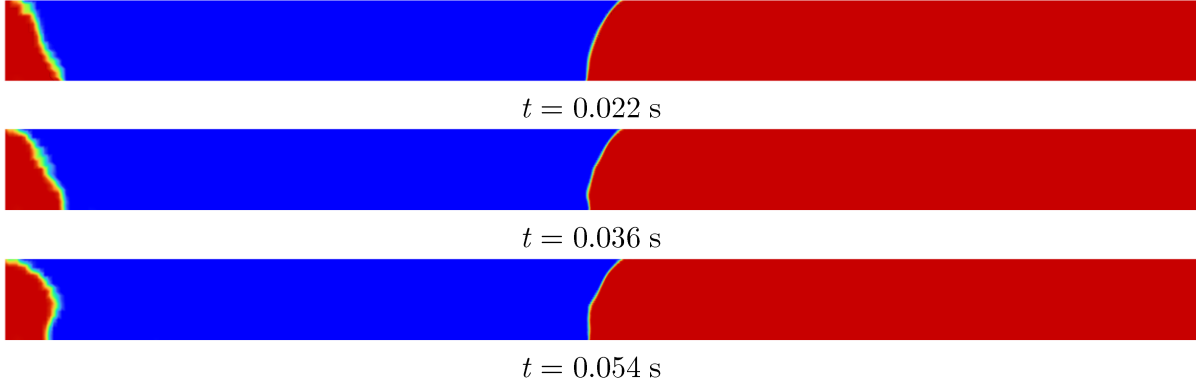
Figure 14: Evolution over a longer time period without gravity

After some time the water and air interface becomes somewhat stationary, which is coherent with the physics as there are no outer forces applied to the fluids. The maximum height the water has risen to within the capillary tube remains constant, the central part continues to show slight fluctuations.

Another interesting number in this context is the so-called Ohnesorge number [1]. It relates the effect of the viscous forces to the inertia and surface tension and can be calculated as follows

$$Oh = \frac{\sqrt{We}}{Re} = \frac{\mu}{\sqrt{\varrho \sigma L}} \sim \frac{\text{viscous forces}}{\sqrt{\text{inertia} \cdot \text{surface tension}}} \tag{20}$$

With the Weber and Reynolds numbers being

$$We = \frac{\varrho v^2 L}{\sigma} \tag{21}$$

$$Re = \frac{\varrho v L}{\mu} \tag{22}$$

For the currently analysed case the Ohnesorge number would be calculated with respect to the properties of water, leading to

$$Oh = \frac{\mu_w}{\sqrt{\varrho_w \sigma L}} = \frac{0.001003 \frac{\text{kg}}{\text{ms}}}{\sqrt{998.2 \frac{\text{kg}}{\text{m}^3} \cdot 0.072 \frac{\text{N}}{\text{m}} \cdot 0.002 \text{m}}} \approx 0.00698$$

In the literature Ohnesorge numbers are oftentimes connected to inkjet printing and fluid films in general, where the length L would rather be a droplet diameter [13], [14].

1.4.2. Imposing a constant rotational speed

Even though not the final objective, analysing the behaviour of the fluid at a constant wall rotation speed was of general interest. As stated before it is important to assure that the result is independent from the chosen mesh and time step size to minimize discretization errors. A mesh refinement study based on local and global flow and mesh variables takes time and was planned to be carried out with the results from simulations with active wall rotations. As a basis the extremely refined mesh shown in Figure 8 with a cell size of 15 µm × 15 µm in the central part was chosen.

As far as the temporal discretization goes, the first approach was to set it to adaptive again to have the software adapt it in function of the Courant number, and then make manual adjustments based on these results. The smallest time step adopted by the software lies around $\Delta t_{\text{ts}} = $ 6e-5 s, which surprisingly was higher than the one found in the case without wall rotation. Based on the Courant number explained in 1.1.4 that should be the main criterion for the determination of this value this is counterintuitive. As Fluent's algorithms for these types of determinations are neither fully explained nor comprehensible, this has to be taken as it is. To be able to keep the next results comparable with the previous ones, the time step size was manually set to the same value of 1e-5 s, which should lead to significant results being lower by a factor of six compared to the value conforming with the $C = 0.9$ condition.

Keeping all the settings equal to the case analysed in Figure 12 without wall rotation, but now imposing an angular speed of 70 rad/s the results were disappointing.

<div align="center">

$t = $ 2e-5s $= 0.00002$ s $t = 0.0008$ s $t = 0.00014$ s

$t = 0.00064$ s $t = 0.00084$ s $t = 0.001$ s
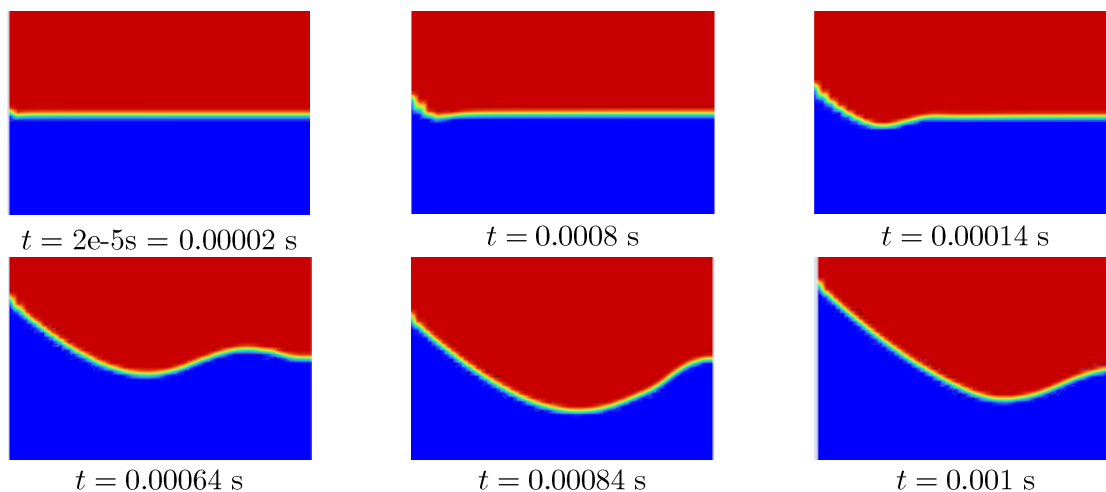
Figure 15: Results at $\omega = 70$ rad/s

</div>

The results seem to be identical to the ones obtained without a wall motion in Figure 12.

The way to judge that is not solely based on eyeballing the contours, the total amount of water phase over the sum of all cell volumes can be tracked. At two identical time instants this variable differed for the two solutions: this means that the rotation had some effect on the solution, but from the contours it is evident that the effect comes from the amount and way that air is being sucked back in through the outlet on the bottom.

$t = 0.00084$ s	$t = 0.00084$ s	$t = 0.00084$ s,	$t = 0.00014$ s,	$t = 0.00014$ s,
$\omega = 0$ rad/s	$\omega = 1$ rad/s	$\omega = 400$ rad/s	$\omega = 70$ rad/s	$\omega = 400$ rad/s
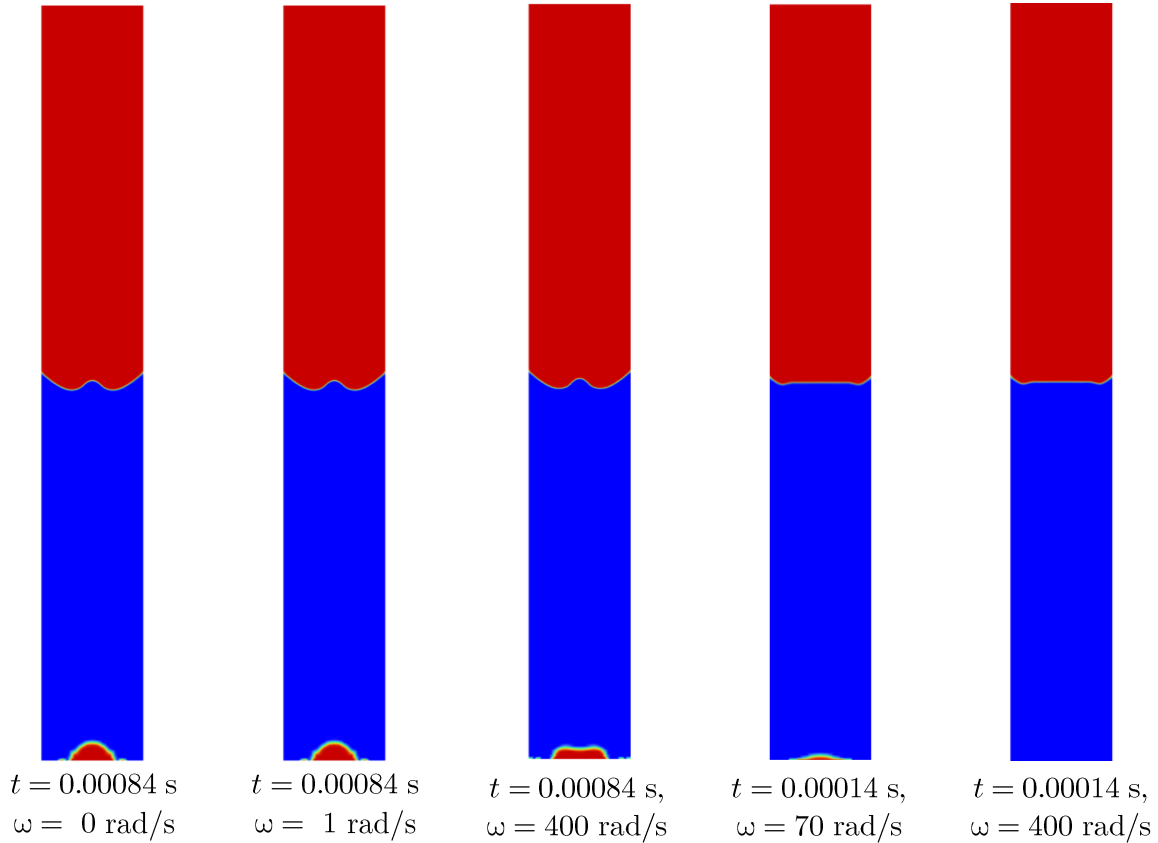
Figure 16: Results for different rotational speeds with the same constant time step of 10 µs

This led to two separate conclusions at the point. The first being that due to the notably changing backflow behaviour Fluent does take the imposed wall rotation into consideration. To rule out this being a user error, the simulations have been repeated and post-processed thoroughly. The second one that seemingly there is no effect on the interface, neither with respect to the droplet formed in the central part nor the outer parts in close contact with the rotating wall. The rotational speeds imposed are relatively high, as the radius of 1mm leads to speeds up to $v_{\text{rot}} = \omega \times r = 0.4 \frac{\text{m}}{\text{s}}$ or $v_{\text{rpm}} = \omega \cdot \frac{30}{\pi} \approx 3920$ rpm, and therefore not seeing any effect of the wall rotation in form of fluid disturbance near this region is not what was expected.

To rule out problems of the 15µm mesh, the calculations for $\omega = 70$ rad/s have been repeated for a mesh with a cell side length of 10 µm (-33 %) and one of 45 µm (+200 %) in the central part. This did not result in significantly different results and is not surprising, as the chosen mesh is already extremely fine in the central region.

As changing the imposed angular speed for the wall motion had no apparent effect on the fluid interface, the next step was to check whether the temporal discretization had an effect on the solution whilst keeping the rotational speed constant at $\omega = \text{const} = 1$ rad/s. Too big time steps could be smoothing out transient phenomena, too small ones should generally only lead to a higher computational time. The first step was taking a value that lied below the $C = 0.9$ threshold that was evaluated by Fluent to be around $\Delta t_{\text{ts}} = 6\text{e-}5$ s. Going with a constant $\Delta t_{\text{ts}} = 5\text{e-}5$ s the simulation presented a completely different behaviour. Please note that in order to increase legibility, only the real calculated flow domain is represented in a horizontal manner. Mirroring it on the x-axis will be done wherever it helps to understand the physics of the problem.

$t = 1\text{e-}4$ s $= 0.0001$ s

$t = 2\text{e-}4$ s $= 0.0002$ s
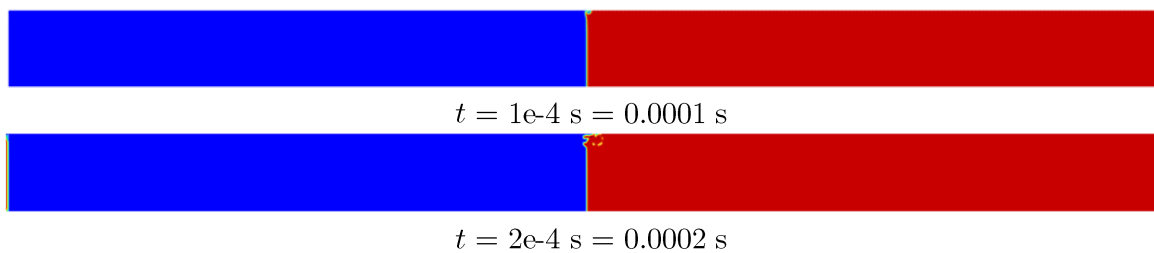
Figure 17: Flow profiles with constant $\Delta t_{\text{ts}} = 5\text{e-}5$ s rotating at $\omega = \text{const} = 1$ rad/s; water is blue on the left, air is red on the right

$t = 1\text{e-}4$ s $= 0.0001$s $t = 2\text{e-}4$ s $= 0.0002$ s
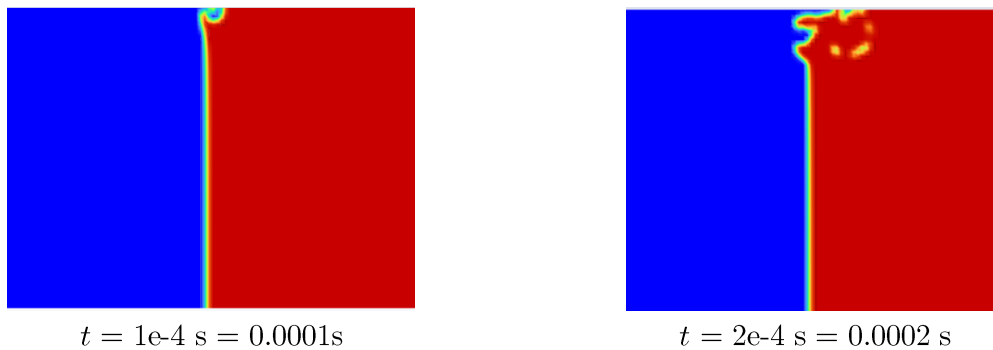
Figure 18: Close up of the central part for flow profiles with constant $\Delta t_{\text{ts}} = 5\text{e-}5$ s

No further temporal instants are displayed, as the solution diverged at the next time step. Trying to get better insights into what might have happened, it was decided to draw the contours of the swirl velocities too. Before the divergence the results looked as expected. The swirl speed at the furthermost part of the boundary is equal to $v_{\text{rot}} = \omega \times r = 0.001 \frac{\text{m}}{\text{s}}$, and the part with the air phase gets accelerated quicker through the radial coordinate due to the lower inertia. The apparent drop of swirl speed in the right part of the water phase comes from the more refined mesh leading to better results close to the wall for the central region.
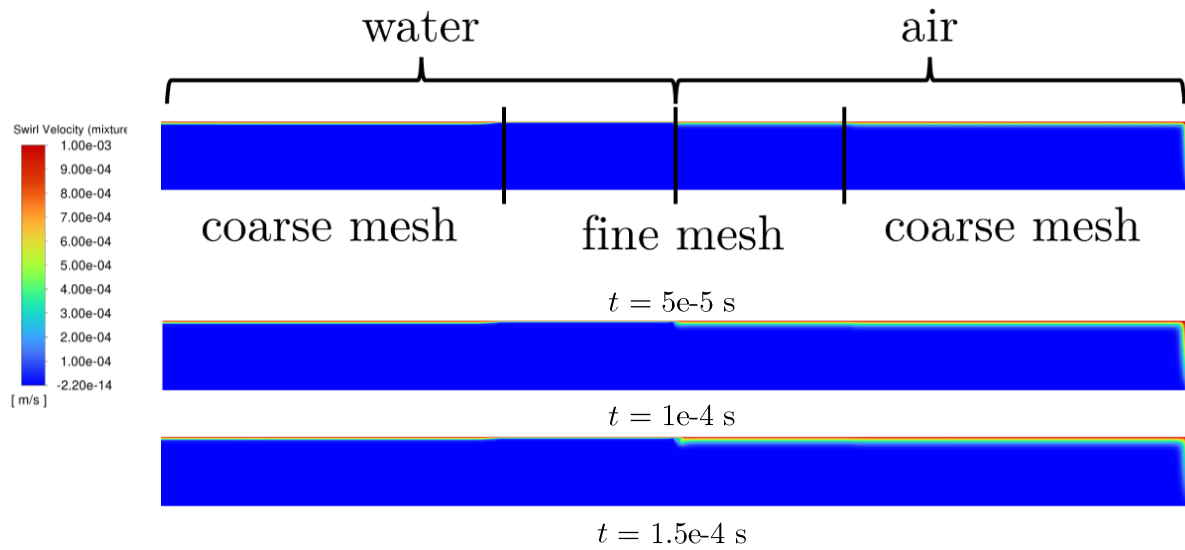
Figure 19: Contours of swirl velocities at different instants

The divergence occurs after the last time step, and here an unphysical distribution of swirl velocities can be observed.
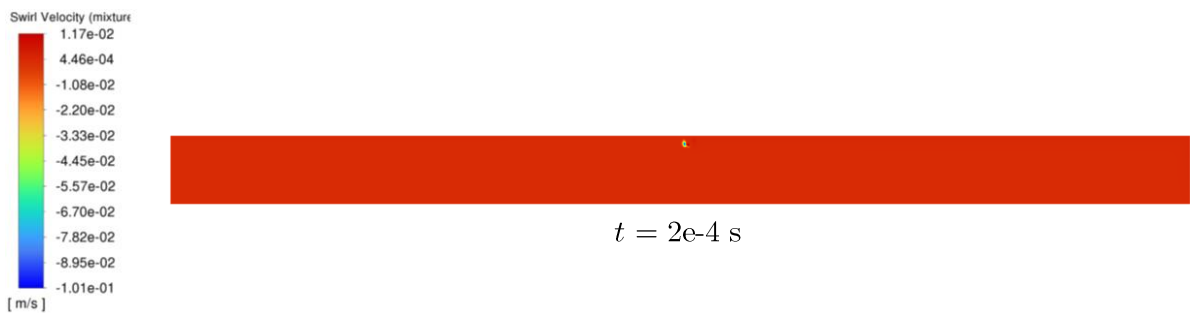
Figure 20: Contours of swirl velocity in the last instant before divergence

This behaviour can be replicated by setting the same initial conditions. As this might be an issue connected to this precise $\Delta t_{\text{ts}} = 5\text{e-}5$ s, setting different time steps was tried out. Making it bigger leads to divergence straight away, it was not possible to gain any new insights from this. Bringing it down by the factor five to $\Delta t_{\text{ts}} = 1\text{e-}5$ s would mean repeating the results reassumed in Figure 16; so the next steps were the analysis of the cases in between. They are reassumed in the following Table 2.

Table 2: Outcomes depending on the chosen Δt_{ts} with an angular speed of $\omega = 1$ rad/s

Δt_{ts} [s]	outcome
>5e-5s	almost instant divergence
5e-5s	almost instant divergence
4e-5s	almost instant divergence
3e-5s	early divergence
2e-5s	late divergence
1e-5s	simulation runs through
1e-6s	simulation runs through

The diverging cases all have in common that local swirl velocities get very high.

To make an example, during the simulation of $\Delta t_{\mathrm{ts}} = 3$e-5 s swirl velocities in the order of magnitude of $10^9 \frac{\mathrm{m}}{\mathrm{s}}$ shortly before divergence were witnessed on the virtual machine. Running the case on the virtual machine or on another local computer led to different results, but re-running it on the respective machines themselves consistently led to the same outcome.

$t = 3.6$e-4 s
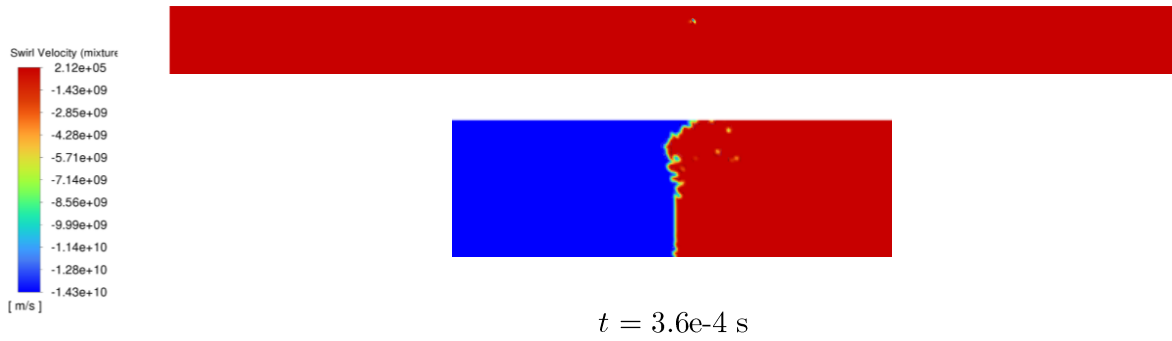
Figure 21: Frame before divergence for $\Delta t_{\mathrm{ts}} = 3$e-5 s run on virtual machine provided by the UPM $\omega = 1$ rad/s, swirl and phase contours

$t = 2.4$e-4 s
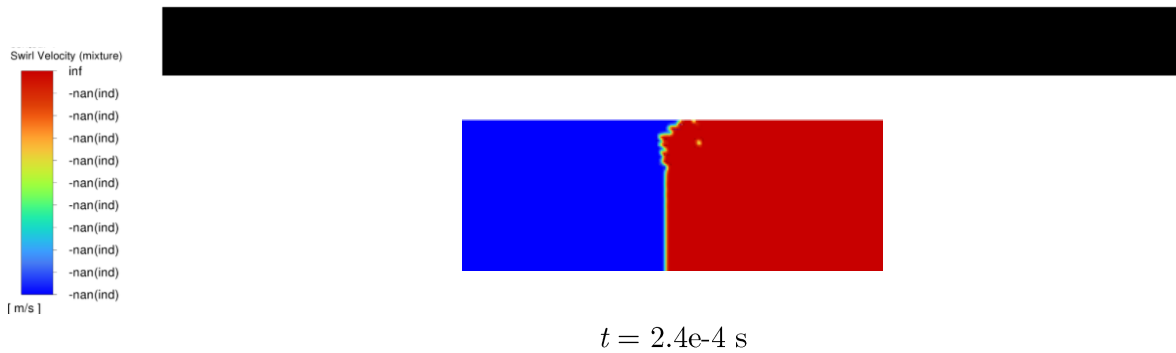
Figure 22: Frame before divergence for $\Delta t_{\mathrm{ts}} = 3$e-5 s run on a Thinkpad with AMD Ryzen 4000, $\omega = 1$ rad/s, swirl and phase contours

For the sake of comparison, at this point trying to set the same time step of $\Delta t_{\text{ts}} = 3\text{e-}5$ s for a non-rotating wall was tried.

$$t = 2.4\text{e-}4 \text{ s}$$
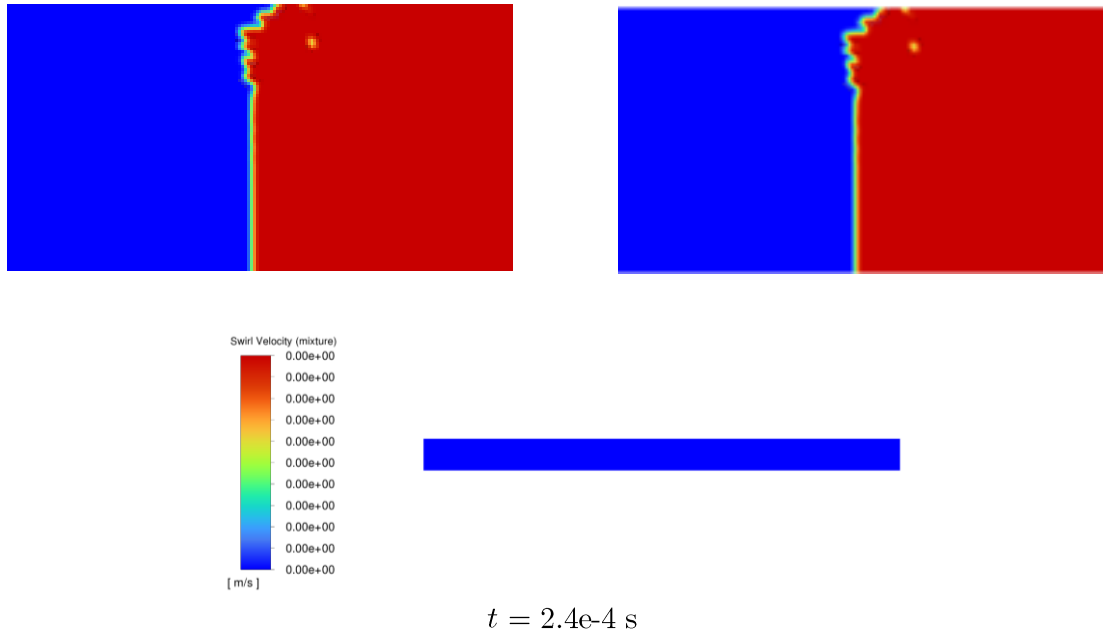
Figure 23: Frame before convergence on virtual machine (left) and local Thinkpad (right), $\omega = 0$ rad/s

The results on the virtual machine and the Thinkpad are virtually identical. The swirl velocities are nil at every instant as there is no rotation imposed. These results point against the high swirl velocities leading to divergence, and rather to the flow itself dispersing in a manner that allows unphysically high swirl velocities. Performing this check was an afterthought during the post-processing and did not happen in chronological order. Another case with results worth explicitly pointing out is the one with $\Delta t_{\text{ts}} = 2\text{e-}5$ s. This case diverges shortly after the main peak in the central part has formed, while all the ones with bigger time steps diverge long before that. Plotting the contours gives something a little closer to what was hoped to be seen from the beginning.

$$\Delta t_{\text{ts}} = 2\text{e-}5 \text{ s}, \ t = 0.74 \text{ ms}$$

$$\Delta t_{\text{ts}} = 1\text{e-}5 \text{ s}, \ t = 0.74 \text{ ms}$$
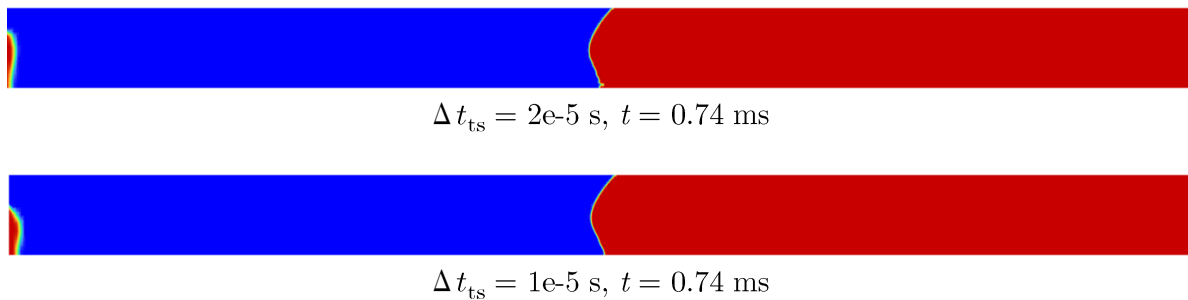
Figure 24: Contours at the same instant for two different Δt_{ts}, $\omega = 1$ rad/s

The backflow differs again in the simulation with the doubled the time step.

$\Delta t_{\mathrm{ts}} = 2\text{e-}5$ s, $t = 0.74$ ms $\Delta t_{\mathrm{ts}} = 1\text{e-}5$ s, $t = 0.74$ ms
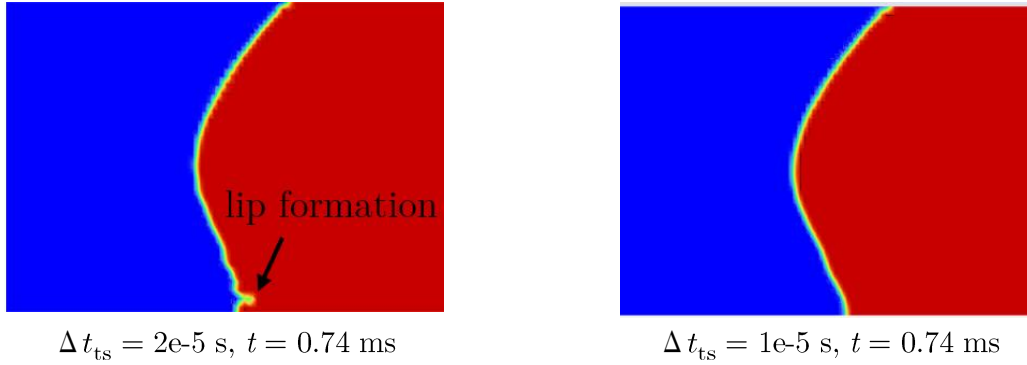
Figure 25: Close up of contours at the same instant for two different Δt_{ts}, $\omega = 1$ rad/s

There is some form of lip formation visible on this frame, very close to where the wave in the middle reaches its maximum vertical extension. In the following frame there is no detached water in the air phase. The comparison is made to prove that by halving the Δt_{ts} and reaching the identical flow time this result could not be replicated, hence there is still a strong dependence of temporal discretization on the solution.

The next idea was to decrease the Δt_{ts} by a whole order of magnitude to $\Delta t_{\mathrm{ts}} = 1\text{e-}6$ s. This resulted in the same solution as with $\Delta t_{\mathrm{ts}} = 1\text{e-}5$ s on the interface and pressure outlet. It is worth noting that with the computational power provided to me by the University, performing various sets of simulations on such a timescale would not be feasible by any means.

$\Delta t_{\mathrm{ts}} = 1\text{e-}6$ s, $t = 0.74$ ms $\Delta t_{\mathrm{ts}} = 1\text{e-}6$ s, $t = 0.84$ ms
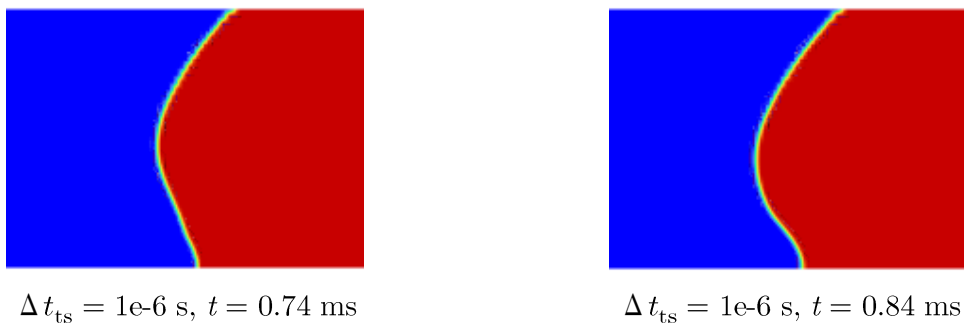
Figure 26: Phase contours around the first peak at $\Delta t_{\mathrm{ts}} = 1\text{e-}6$ s

1.4.3. Additional stabilization mechanisms

Trying to look deeper into these issues by reading documentation, contacting experts and reading through forums, the key finding was that Fluent is aware of cases where VOF simulations can lead to "unphysical acceleration of the lighter phase" [3] if the two fluid phases have densities that differ from one another by various orders of magnitude. The solutions implemented by the software to mitigate this known issue are "settings optimization", "advanced optimization" and "velocity limiting". Given that the results displayed too high swirl velocities, limiting the maximum swirl velocity to a more physical value seemed possibly helpful, but as the guides also point out doing this could inversely affect the realism of the simulation results. Hence, the amount of limiting would have to be done with care and the results carefully interpreted.

In a first approach the two optimizations (hence no velocity limiting) were applied. This should "improve solution stability without significantly compromising its accuracy" [3]. Which settings are influenced by this is reassumed in the Appendix 1. Doing so led to the following results at $t = $ 3e-4 s which is the time instant before divergence for the optimized case setup

Figure 27: Swirl contours with optimizations at $t = $ 3e-4 s with $\Delta t_{\text{ts}} = $ 3e-5 s

Figure 28: Swirl contours without optimizations at $t = $ 3e-4 s with $\Delta t_{\text{ts}} = $ 3e-5 s
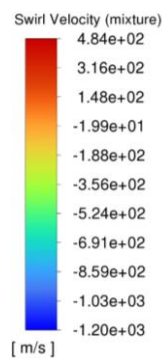
Figure 29: Colour legend corresponding to case with optimizations
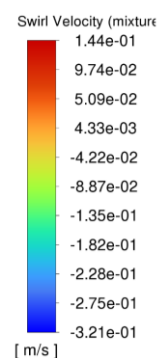
Figure 30: Colour legend corresponding to case without optimizations

The comparison shows that the problem persists, expressed by very high gradients in terms of swirl speeds at the interface between the two fluids. The swirl speeds at this time instant are not as high when considering the non-optimized case, but this is due to the fact that it ran two time steps further before diverging due to these high velocities as portrayed in Figure 21. Looking at the phase contours in this precise region leads to:
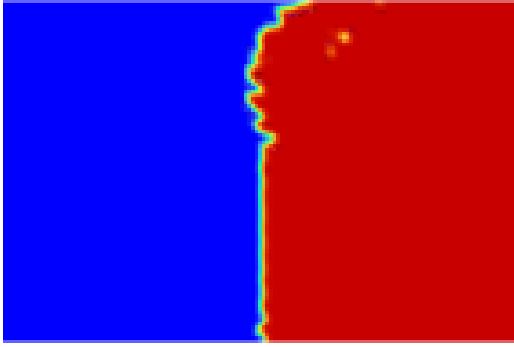
Figure 31: Phase contours with optimization at $t = $ 3e-4 s with $\Delta t_{ts} = $ 3e-5 s
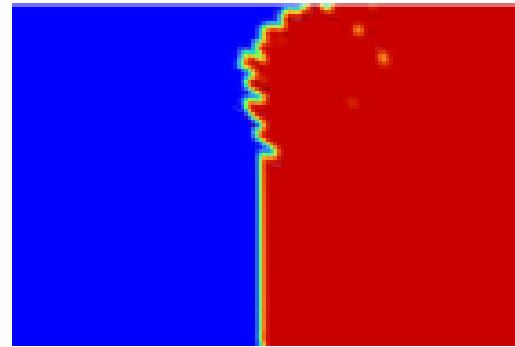
Figure 32: Phase contours without optimization at $t = $ 3e-4 s with $\Delta t_{ts} = $ 3e-5 s

The optimization is active and does change the solution, but it does not solve the problem with the unphysically high velocity gradients at the interface. Limiting the velocity is the next logical step added, as this may prevent the divergence of the solution.

With the given angular speed of $\omega = 1$ rad/s, the maximum swirl velocity right on the wall should correspond to $v_{rot} = \omega \times r = 10^{-3} \frac{m}{s}$. It is important to note that the "velocity limiter" acts solely on the swirl velocity; it was obviously introduced by Ansys as they were aware of problems of this matter. As a first conservative approach, the swirl velocity was limited to 50 $\frac{m}{s}$. The idea was to inhibit the very high speeds leading to divergence, whilst trying not to interfere with the results too much. Doing so with the case on the verge of stability of $\Delta t_{ts} = $ 3e-5 s led to the case running longer before divergence
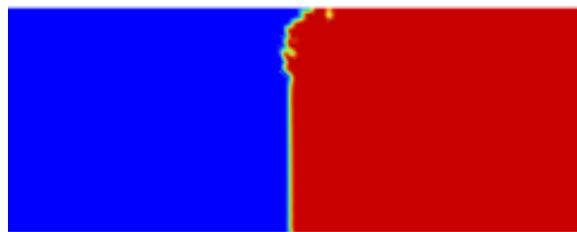
Figure 33: Phase contours of $\Delta t_{ts} = $ 3e-5 s with velocity limiting to 50 m/s at $t = $ 2.4e-4 s

Figure 34: Swirl contours at same instant as phase contours; legend on the right
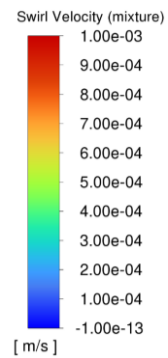
The following Figure 35 is directly compared in Appendix 5 with the other two cases in Figure 31 and Figure 32, calculated with and without optimization but without velocity limiting.
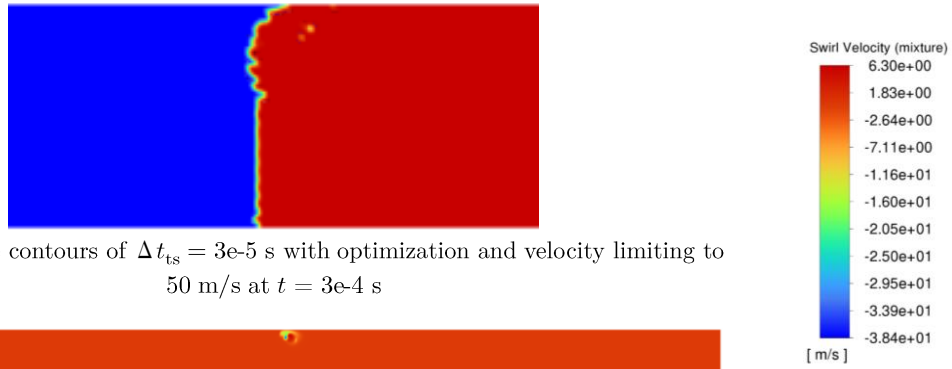
Figure 35: Phase contours of $\Delta t_{\mathrm{ts}} = $ 3e-5 s with optimization and velocity limiting to 50 m/s at $t = $ 3e-4 s

Figure 36: Swirl contours at same instant as phase contours; legend on the right

Without limiting the maximum velocity, this was the last instant before the solution diverged given the $\Delta t_{\mathrm{ts}} = $ 3e-5 s (see Figure 31). Now, with the velocity limiting, the solution is able to continue for a few more time steps. The maximum swirl velocity nevertheless starts exceeding $50 \frac{\mathrm{m}}{\mathrm{s}}$ soon though; we cycle through a bunch of swirl speed distributions similar to Figure 36 until we hit the last instant before divergence:
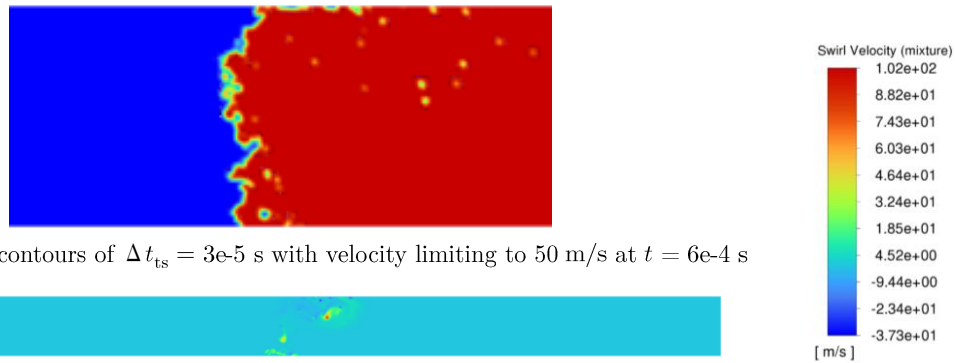
Figure 37: Phase contours of $\Delta t_{\mathrm{ts}} = $ 3e-5 s with velocity limiting to 50 m/s at $t = $ 6e-4 s

Figure 38: Swirl contours at same instant as phase contours; legend on the right

The case of $\Delta t_{\mathrm{ts}} = $ 2e-5 s which led to a sort of lip formation was analysed again. It diverged around the same time of the simulation without velocity limiting and presented the lip again.
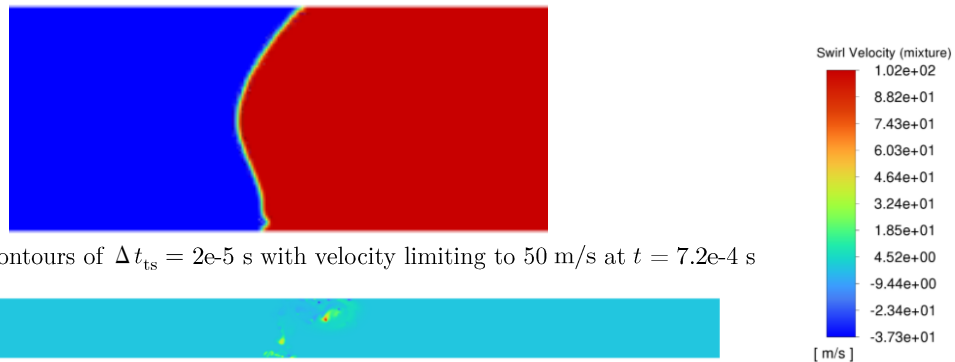
Figure 39: Phase contours of $\Delta t_{\mathrm{ts}} = $ 2e-5 s with velocity limiting to 50 m/s at $t = $ 7.2e-4 s

Figure 40: Swirl contours at same instant as phase contours; legend on the right

The lip is now visible after 0.72 ms opposed to after 0.74 ms in the case without velocity limiting and additional stabilization mechanisms.

Unfortunately, all these efforts did not bring the case to a stable solution. In an attempt to get help from software experts, I posted a description of the issues on the online forum [15] and received an answer from a dedicated employee and long-time forum expert. He sustained that the case should run fine under my assumptions and settings, and that I should try to re-run it on Fluent's new 2024R1 release. As a result of this advice, the results in the rest of this chapter 1.4.3 will be calculated with Ansys Fluent 2024R1, opposed to all the rest of this work that was done with Fluent 2022R2. To help following the new intents they are quickly resumed in Table 3.

Table 3: Calculations performed in Fluent 2024R1

#	Δt_{ts} [s]	velocity limiting [$\frac{\text{m}}{\text{s}}$]	ω [$\frac{\text{rad}}{\text{s}}$]
(a)	1e-5	50	1
(b)	1e-5	50	50
(c)	1e-5	50	50 triangular (1*)
(d)	2e-5	50	1
(e)	3e-5	1	1
(f)	3e-5	50	1

(1*) peaks at $t = 0.0005$ s; for details, please see chapter 1.4.4

Imposing angular speeds varying by the factor 50, and in the third case even with an acceleration pattern, the cases calculated with $\Delta t_{\text{ts}} =$ 1e-5 s resulted in non-divergent solutions.
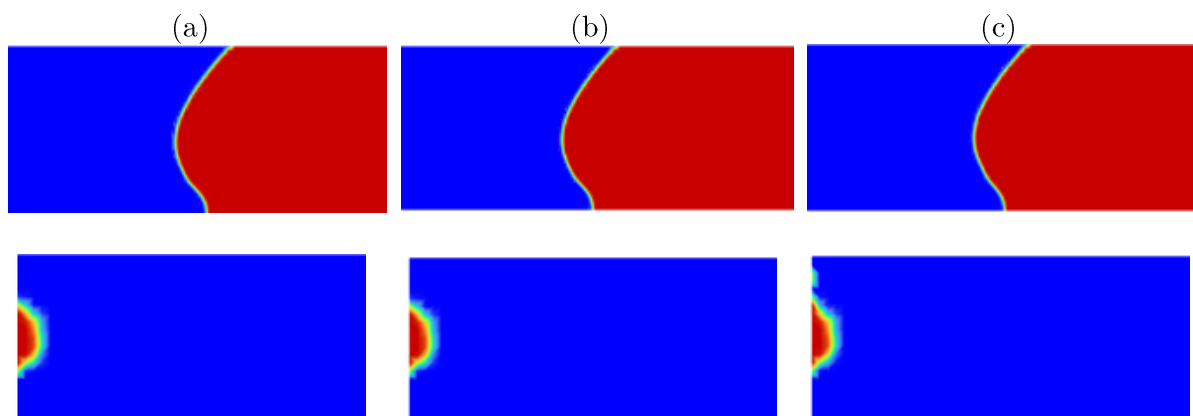
Figure 41: Contours in the central and left part evaluated at $t = 0.00084$ s

The contours of (a) and (b) look identical, the ones of (c) are identical on the interface and show a slight deviation on the backflow. Given that the wall speed peaked before this time instant it can be said that there is no substantial difference to the case with constant wall speed.

Figure 42: Case (d)

The lip is visible after 0.72 ms again and is similarly pronounced to the case before without velocity limiting. It is worth noting that with these settings this case does not diverge any longer.

When setting the time step size to $\Delta t_{ts} = $ 3e-5 s, where beforehand we had an early divergence and increasing the amount of swirl limitation, one can really start to see the velocity limiting kicking in.

(e) limited to 50 $\frac{m}{s}$, diverges

(f) limited to 1 $\frac{m}{s}$, does not diverge

$t = 0.00036$ s

$t = 0.00036$ s
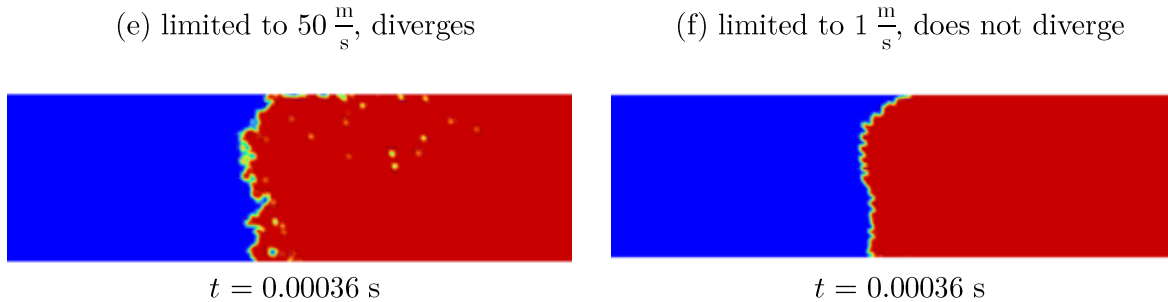
Figure 43: Comparison between different amounts of velocity limiting

Keeping everything but the degree of velocity limiting constant, the interface changes significantly. There seems to be some sort of stabilized fingering on the highly limited case (f) that leads to a similar profile outline to case (e).

It should be noted that the swirl speeds still begin to show unphysical behaviours as portrayed in Figure 19 and Figure 20 after some point.
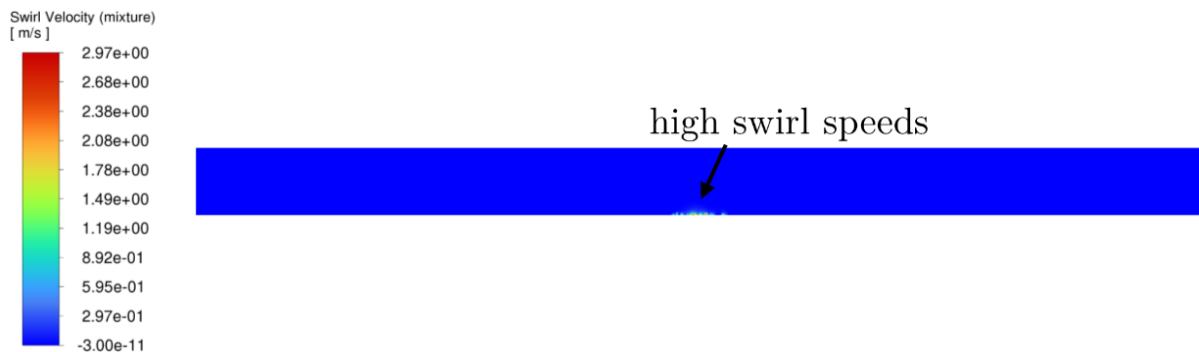
Figure 44: Swirl contours of the case limited to 1 m/s at $t = 0.00036$ s

The difference is that now these issues don't occur on the zone close to the wall, like in e.g Figure 38 and all the preceding swirl contours any longer, but on the bottom part close to the centre of the tube.

At this point, there are two possible outcomes. Either the time step was chosen so small that the wall rotation had no apparent effect at all on the fluid interface, or it was chosen big enough to be able to see an instability that was not controllable by Fluent's algorithms. Having found the instability region and went above and below this Δt_{ts} by a whole order of magnitude, after realizing that the newly introduced stability mechanisms did in fact lead to unphysical results following this approach further was deemed neither adequate nor expedient.

1.4.4. Imposing a variable rotational speed

The final goal was to impose an acceleration pattern as displayed in Figure 2: Generic applied velocity profile, and maybe accelerating the tube with a given rate instead of imposing a rotational speed straight away with the fluid at rest could have helped mitigating some of the encountered numerical issues. In order to impose a triangle-shaped velocity profile to the wall rotation, learning how to use Fluent's expression editor was necessary. As this could have led to a senseful solution and could be beneficial for further works the time was invested. The easier option would have been to set the wall rotation with a differentiable function, but this would've been only an approximation and not consistent with the previous work leading to the project. To generate a profile like this
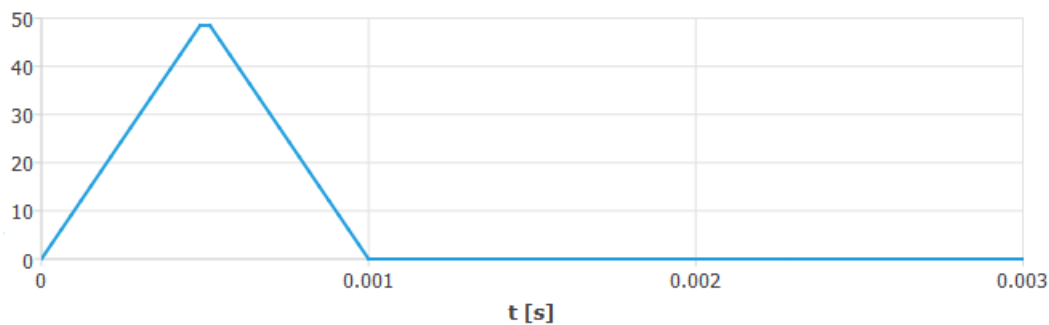
Figure 45: Example of the applied velocity profile to the wall rotation in case Figure 41 (c) as taken from Fluent

one has to set the following expression

IF(t < 0.001[s], 50e3[s^-2 rad]*t, IF(t <= 0.002[s], 50e3[s^-2 rad]*(0.002[s]-t), 0[s^-1 rad]))

It is easy to understand which values need to be modified in order to change the shape of the triangle.

A more generalized form would be

IF(t < a[s], b[s^-2 rad]*t, IF(t <= 2a[s], b[s^-2 rad]*(2a[s]-t), 0[s^-1 rad]))

Where $a = t_{\mathrm{acc}}$ and $b = \frac{\omega_{\mathrm{max}}}{t_{\mathrm{acc}}}$

The results obtained in Figure 16 were a useful guideline to set up the parameters and therefore a simulation schedule, that unfortunately due to the lack of effect on the solution had to be discarded in the end (see Figure 41)

Please note that in the profile coming out of Fluent's expression editor in Figure 45, there are no labels on the x and y-axes, and it looks like the peak of the triangle is not sharp. These issues are solely connected to the function preview window within the software, the form of the peak slightly changes when changing the y-axis delimitations. The current value at a given instant can be stated by the software and is equal to Current Value: 0 [s^-1 rad] at $t = 0$ s, hence the units are also consistent and there is no reason to believe that there are issues with that.

1.4.5. 3D Simulations

The problem persisted and could have been connected to the definition of the swirl rotation outside of the 2D simulation plane. Trying a 3D setup seemed like a suitable approach that had to be tried out and could have been at least used for a final validation of eventual findings with the 2D model. Whether the provided computational power was sufficient was doubtful from the start. Creating a tube geometry in three dimensions is straightforward, meshing it depends on the specific application, like if the mesh should be more refined towards the wall or more conformal towards the centre. A lot of research has been performed on this topic, and a recent article regarding two-phase modelling in pipes from 2017 suggests that a so-called "butterfly grid" compared to three other meshing approaches is the most versatile one producing the "best agreement" when compared to real-world applications, and is therefore "highly recommended" [16]. Hence this more elaborated technique was studied and had to be implemented manually in Fluent. To allow for an easier replicability, the geometry division as well as meshing settings are added to the Appendix
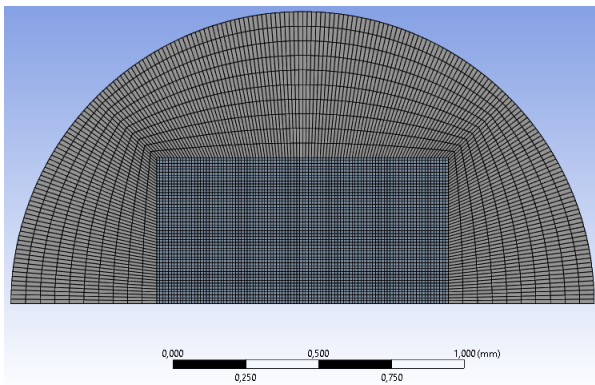
Figure 46: Front view of the 3D butterfly mesh
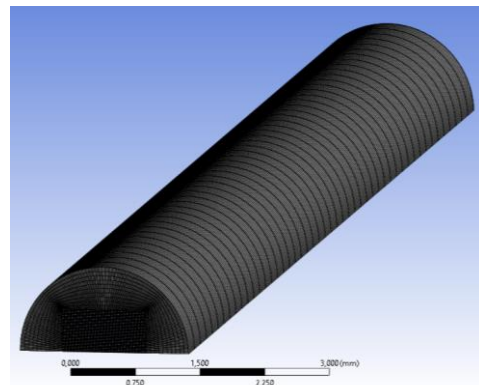
Figure 47: Side view of the 3D butterfly mesh

The boundary conditions are identical to the previously elaborated ones. The domain was split with a symmetry condition to save computation time, but even by coarsening the mesh (the cells in the centre of Figure 46 have a side length 10µm) it soon became clear that with the computational power provided, exploring a set of combinations was simply not feasible. As the in-depth analysis of the two-dimensional flow domain did not lead to any hoped-for results, the need of validation with a 3D model also vanished.
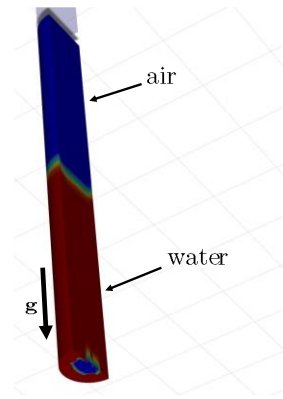
Figure 48: Sideview of the 3D solution at $t = 11.2$ ms with $\omega = 0$ rad/s

$t = 0.01$ ms $t = 0.82$ ms $t = 1.36$ ms $t = 2.06$ ms $t = 2.56$ ms $t = 3.06$ ms
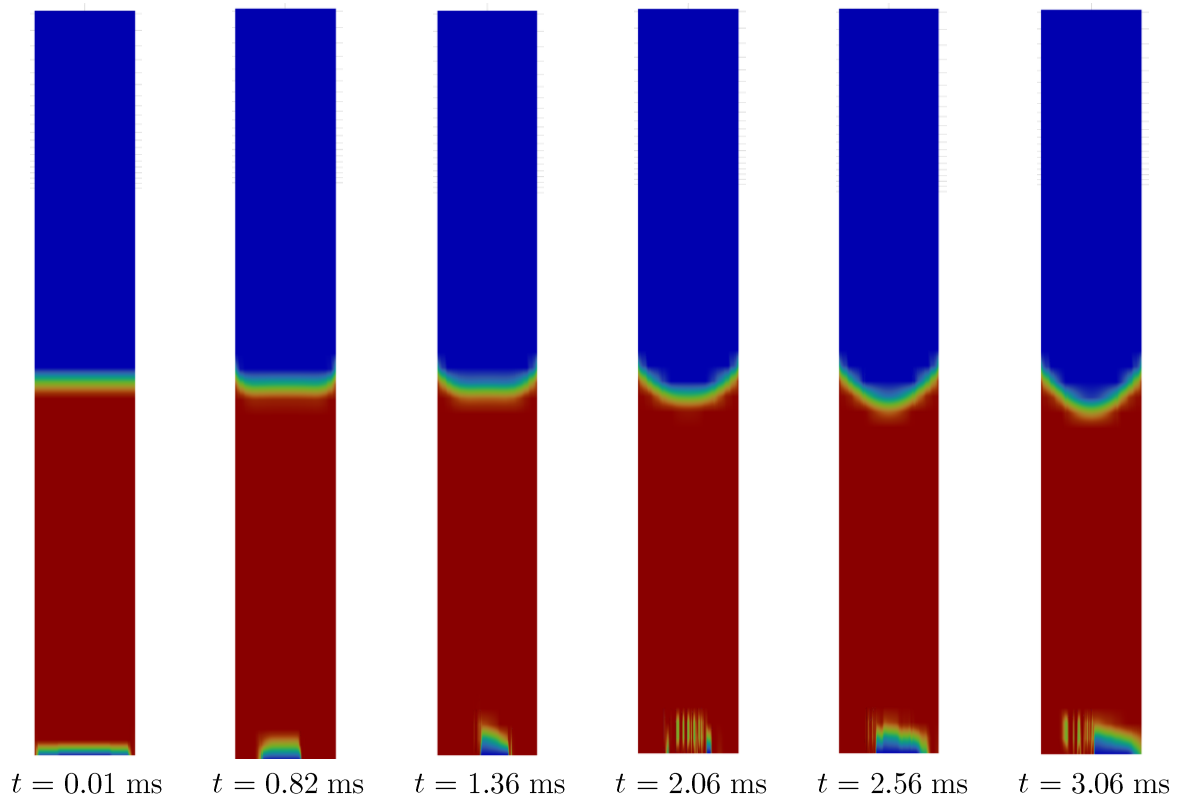
Figure 49: Bottom view of the 3D solution at different time instants with $\omega = 0$ rad/s

Please note that even if red, the bottom phase is still the water as specified at the beginning.

The solution presents numerical artefacts on the pressure outlet that don't smooth out over time. At $t = 0.82$ ms where a sort of peak usually arose the contours are smoothed out a lot to a point where no peak is clearly visible. The more smoothed out contour on the interface is something noticeable through all time steps. In conclusion, this new case setup did not lead to results useful for analysing fine undulations on the interface. Given that the overall flow field seems similar to the 2D case that did not yield positive results already and computational power was a big issue, this approach was not further pursued in the terms of this work.

1.4.6. Change of fluid phases

Investigating different fluid combinations was an objective from the beginning. The previously encountered issues linked to the stability at the interface in the case of air-water could have been connected to the significant density difference between them, as stated in the Theory Guide. Thus, choosing two incompressible fluids with densities differing from one another by a factor of less than 0.8 was the last resort for this type of simulation approach.

Table 4: Data of used fluids at 25 °C [10]

Physical quantity	Water	Oil
Density ϱ	$998.2\,\frac{\text{kg}}{\text{m}^3}$	$837\,\frac{\text{kg}}{\text{m}^3}$
Interfacial tension coefficient σ	$0.032\,\frac{\text{N}}{\text{m}}$ [17]	
Dynamic viscosity μ	$0.001003\,\frac{\text{kg}}{\text{ms}}$	$0.287\,\frac{\text{kg}}{\text{ms}}$

As stability was a constant issue, the simulations were carried out using the integrated adaptive time stepping scheme. Interestingly all three cases listed below were automatically set to the identical $\Delta t_{\text{ts}} \approx 7.1117\text{e-}06$ s after only a few iterations; this is above the minimum bound which was set to 1e-6 s by a factor of seven.

#	Angular speed ω $[\frac{\text{rad}}{\text{s}}]$	Additional change
(a)	0	-
(b)	50	-
(c)	50	no gravity

The postprocessed results after a flow time of $t = 0.014$ s look as follows:
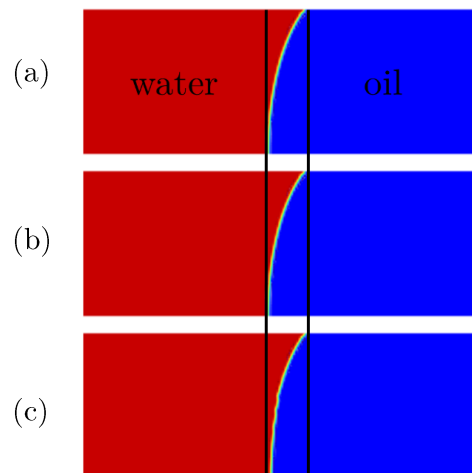
Figure 50: Comparison of Water and Oil combination at different rotational speeds and without gravity

The addition of gravity does seem to pull the water out of the capillary tube a little quicker (the part in the centre did not travel as far down in case (c)), but does not significantly change the interface between the two liquids. This change was done in an effort to troubleshoot, as eliminating additional terms could've helped the solution. Adding the wall rotation still had no apparent effect on the solution.

1.5. Conclusions and Outlook

The main issue lies in the results being seemingly not influenced by the imposed angular speed as the contour displaying the interface between the two phases does not change significantly and as one would physically expect. The settings were checked by performing tutorials concerning the free surface of a substantially bigger rotating cylinder filled with water and by spinning the cylinder used in this work around the z-axis (see Appendix 4): in these cases the addition of the rotational speed had the expected effect on the solution.

The divergence happens differently when the simulation is rerun on a different machine or even on the same one, which all leads to believe that numerical issues occur. It shall be added that also changing the direction of the gravity and in another case setting the pressure outlet as a wall in an attempt to work around bugs was tried, but did not lead to substantial changes. All these problems occurred in the central, highly refined zone of the mesh, where going further down from 10 μm cell side length regarding the spatial discretization was neither computationally feasible nor justifiable through the mesh analysis.

As about the stabilization schemes with added velocity limiting, Fluent's algorithms probably oversmooth surfaces to a point where the relatively low forces in a capillary flow get completely overruled. With nearly identical contours for problems with rotational speeds varying in form and various orders and magnitude, coupled with heavy divergence issues with topics the Fluent Theory Guide is aware of, this did not seem like the correct strategy to pursue further. A possible interpretation is that Fluent is not able to calculate the forces on such a small scale in combination with the additional terms coming from the rotating wall boundary condition going into the momentum equation.

Even though this approach was discarded due to the issues described above, there are certain things that could still be tried in future works.

The first is to apply another interpolation mechanism for cells near the interface, being the "Compressive Interface Capturing Scheme for Arbitrary Meshes (CICSAM)". It is stated to be particularly suitable for flows with high viscosity ratios between the fluids and recreates a surface that is "almost as sharp" as the one obtained through Geometric Reconstruction [2]. It is worth recalling tough that the known issue with the swirl velocity divergence was associated to high density ratios and therefore the existence of a lighter and heavier phase. Preliminary tests with CICSAM were performed, and while the solution diverged later than with the Geometric Reconstruction scheme, it still diverged and lead to unphysically looking results (phase contours under Appendix 3).

Another solution could be to approach the problem from a non-inertial, moving reference frame. Instead of moving the wall and keeping the fluid as stationary, one could move the fluid zone and set the reference frame on the wall, solving the governing equations from there. As in the end we are interested in the solution with respect to a stationary coordinate system, one must work the solution back by easily applying $U = U_r + \Omega \times r$. It was verified that Fluent is theoretically capable of solving this problem with an MRF approach, as unsteady rotational speeds can be implemented within the software.

By doing so the terms added to the momentum equation now formulated in terms of relative velocity would be

$$\Omega \times \Omega \times r \text{ (Centripetal)}$$

$$2\,\Omega \times U_r \text{ (Coriolis)}$$

$$\frac{d\,\Omega}{dt} \times r$$

Physically this should not change the result, but it might improve numerical issues and could hence be another viable way to try and look at the solution.

Finally, for the analysed two-phase flow regime trying out a Coupled Level-Set and VOF model could have been attempted. It is presented by Ansys as a combination to overcome limitations of both models. The VOF approach leads to a discontinuous surface while the Level-Set approach has a "deficiency in preserving volume conservation" [2], combining those can tackle both issues.

2. Sessile droplet on a spinning surface

The next microfluidic application analysed concerns the dynamics of a sessile droplet on a rotating glass plate. The situation can be visualized as follows
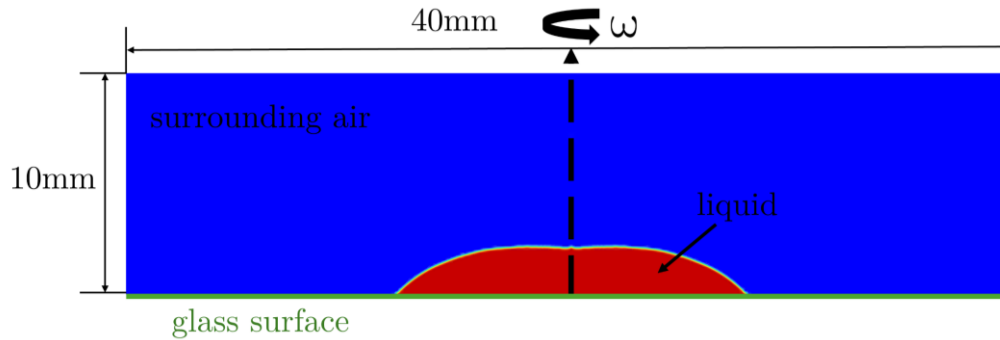
Figure 51: Depiction of a sessile droplet on a spinning glass surface

The way a liquid spreads over a spinning surface is of general importance in many different industrial applications due to the high precision and achievable uniformity, being e.g. semiconductors in this exact size range, display technology, biomedical applications, and modern organic photovoltaics. Understanding all the relevant parameters helps increasing productivity and decreasing the use of e.g. photoresist usage in the microelectronics industry ultimately leading to more environmental sustainability [18]. It depends on the properties of the liquid, the surrounding gas, the rotational speed and pattern, and, finally, the surface it is carried out on. It will be attempted to adimensionalize the problem wherever possible with the rotational Bond number Bo_r, the Ohnesorge number Oh and lastly the Weber number We.

As this topic is largely covered by academics and the industry, to gain more precise insights and draw relevant conclusions a short literature review is desirable and was therefore carried out.

2.1. Literature overview and state of research

According to a paper concerning the dimensionless groups for free surface flows of complex fluids published in 2005 by McKinley coating operations of Newtonian fluids are "fully parametrized by the values of Ca and Oh for the process of interest", however other combinations of these parameters "may also be used" [19]. The paper lists the Weber and Ohnesorge number as possible combination, noting that

$$We = Re \cdot Ca = \frac{\varrho v L}{\mu} \cdot \frac{\mu v}{\sigma} = \frac{\varrho v^2 L}{\sigma} \tag{23}$$

Other researchers have found that spin coating processes themselves do only depend on We in the initial phase where the droplet is falling onto the rotating surface from a predefined

height (dynamic spin coating) [20], which will not be relevant for the first part of this analysis where a static spin coating process is analysed. To describe a static spin coating process taking the rotational Bond number as the characteristic dimensionless group "is more appropriate" as it incorporates the angular velocity of the spinning surface and opposed to Ca does not change when the liquid is spreading [21]. This can be illustrated through the so-called thin film approximation which will not be derived.

$$Ca = \frac{\mu v}{\sigma} \sim \left(\frac{\varrho V \omega^2}{\sigma}\right)\left(\frac{H}{R}\right) = Bo_r \left(\frac{H}{R}\right) \tag{24}$$

Here, H is the height of the liquid film, while R would be its radial extension on the spinning surface [21]. The fact that there is and one therefore could encounter multiple definitions for the capillary numbers is related to the nature and quantification of the resulting macroscopic forces remaining controversial, with publications listing a collection of at least 41 of them [22].

Reassuming the obtained results and conventional notations the dimensionless numbers used in this work will be defined as follows

$$Bo_r = \frac{\varrho V \omega^2}{\sigma} = \frac{\text{centrifugal effects}}{\text{capillary effects}} \tag{25}$$

$$Oh = \frac{\mu}{\sqrt{\varrho \sigma L}} = \frac{\text{viscous forces}}{\text{inertial forces} \cdot \text{surface tension forces}} \tag{26}$$

As defined in the original work by Wolfgang von Ohnesorge [23]

And finally for cases where dynamic spin coating gets analyzed

$$We = \frac{\varrho v^2 L}{\sigma} = \frac{\text{intertial forces}}{\text{surface tension forces}} \tag{27}$$

Using dimensionless numbers to characterize the problems is of big general interest, but measuring the values contained in them in the first place is too. To be able to make predictions numerical models are being refined [20] and validated with various techniques, the most successful one right one being Axisymmetric Drop Shape Analysis (ADSA). Methods measuring the drop shape directly have many advantages over indirect ones like the Wilhelmy plate method, as they do not rely on adjustable parameters for the determination of the contact angle, can capture transient phenomena in the form of images, and only require little amounts of liquid [24]. With cameras providing the crucial factor of increasing image quality at lower prices over the last decades, the development of algorithms to post-process these images has become of always bigger importance. The followed scheme is always similar and is described in Figure 52.
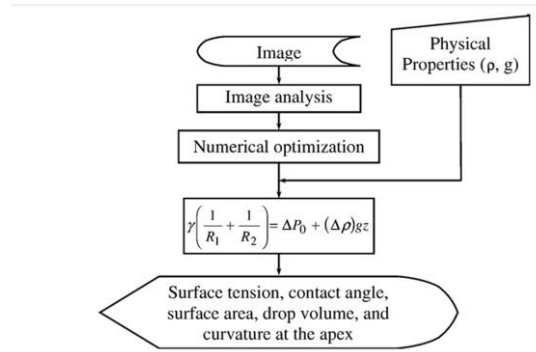
Figure 52: General procedure of ADSA [24]

It is worth noting that the Laplace equation relating the surface tension to the curvature of the interface and the pressure difference across the interface is the same that is used by Fluent (14). Image analysis and the numerical optimization are more significant as it may seem at first glance, as some methods produced inconsistent results for nearly spherical shaped droplets, and the whole ADSA method is getting "scrutinized" since then [24]. The measurement of the contact angle through CFD solvers is done through taking the inclination of the VOF surface (in our case done with a Geometric Reconstruction approach) and is hence independent of image quality, but even more so of cell size and a sharp interface resolution.

To set up physically senseful simulations it is also important to understand what typical speed and size ranges work best for spin coating processes involving different fluids and surfaces. Depending on the liquid properties some Bo_r and spreading radii have been found to lead to so-called fingering instability which is represented in Figure 53 and Figure 54.
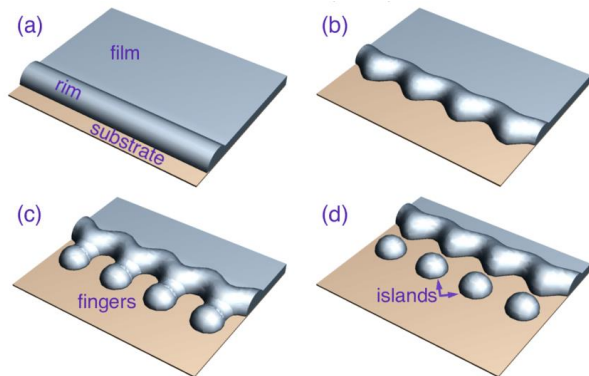
Figure 53: Depiction of fingering instability evolution [25]
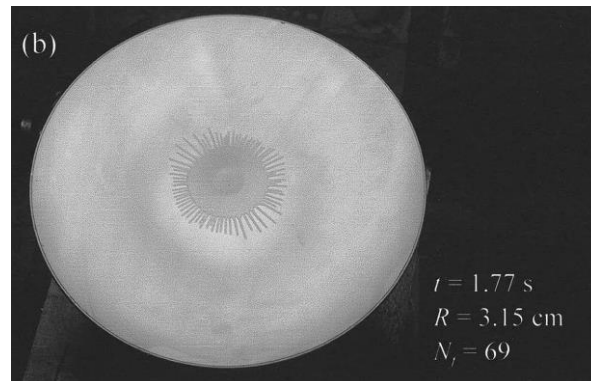
Figure 54: Picture of fingering instability occurring; no visible islands [21]

Typical spin rates used in the industry e.g. for the coating of glass substrates exhibiting self-sterilizing properties lie between 1500rpm and 6000rpm, leading to deposited layers of thicknesses below 10nm [26], which is coherent with other research that has been done validating numerical models with the ADSA method [20]. Ethanol shows a surface tension similar to many organic solvents used in the industry [20] and is therefore analysed next to oil and water which show strongly differing viscosities and surface tensions as a comparison.

2.2. Solver settings

The same transient formulations for the VOF and transport equations, as well as the settings for the temporal and spatial discretization described in the chapters under 1.1 Solver settings have been utilized. There is hence no reason to describe them again and for questions regarding them one should simply refer to the abovementioned chapter. It could be added that opting for a laminar viscosity model could be more problematic in this case, as the literature suggests that turbulent effects of the air above the liquid have an effect on the solution at high spin rates [27]. Their main effect lies within evaporation and drying effects connected to the boundary layer though, so for the sake of simplicity and calculation time the laminar model was still maintained. As far as evaporation models are concerned, due to the characteristic times being in the magnitude of seconds for the cases analysed here without slow initial acceleration phases this effect can be neglected [20].

2.3. Boundary conditions

The boundary conditions are best represented by a sketch as displayed in Figure 55.
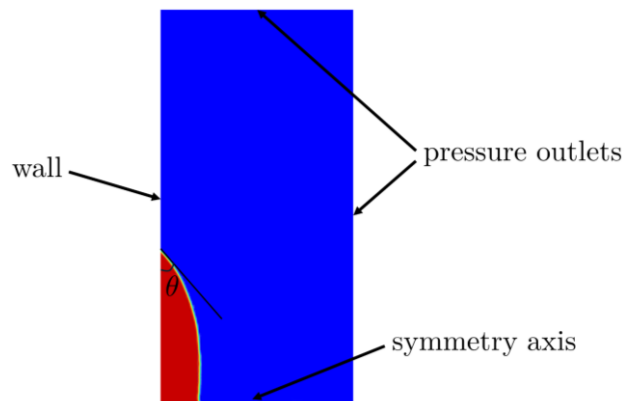
Figure 55: Boundary conditions for the simulation of a droplet on a spinning surface

Again, the pressure outlets are set to a nil gauge pressure, the symmetry axis which is also the axis around which the rotation happens has to be the x-axis at $y = 0$, and the wall imposes a no slip condition to the fluid in its direct proximity. The very interesting part here where physical assumptions must be made is the wall adhesion model. When including this model, it is possible to set a contact angle between the wall and the two phases. This boundary condition of the contact angle forces the interface to be inclined with the set angle to the boundary in the curvature calculation [2]. Fluent then combines this angle with the normally calculated surface normal one cell away from the wall for the calculation of the radii also needed for the determination of the surface tension (14). Now the question is how to determine this angle important for the simulation that must be set in advance. As the simulation result will be depending on it, there is no possibility to evaluate it with a

simulation. This leaves the options of a possible analytical formulation involving the physics and the implementation of previous experimental results into the simulated model.

The majority of publications devoted to wetting phenomena refer to the Young equation which relates the contact angle with three interfacial tensions [28]. Without additional modifications that intend to extend its validity, it can be expressed as follows

$$\cos\theta = \frac{\sigma^{SG} - \sigma^{SL}}{\sigma^{LG}} \tag{28}$$

Where

θ	Contact angle between the wall and the phase interface
σ^{SG}	Surface tension of the solid (and gas)
σ^{SL}	Interfacial tension of the solid-liquid interface
σ^{LG}	Surface tension of the liquid (and gas)
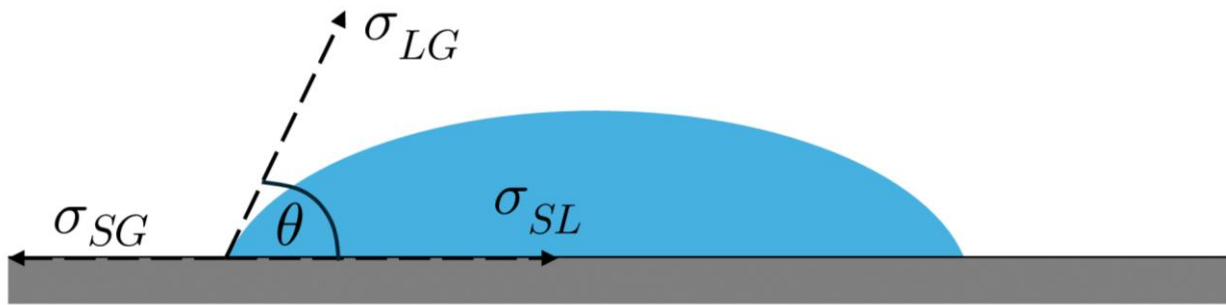
Figure 56: Depiction of a sessile droplet to visualize the different surface tensions contained within the Young-Equation, example with low wettability

Using this equation directly is not possible though, as the "most fundamental issue" of the Young equation "stems from the impossibility to measure solid-related STs [surface tensions]" [29]. The current approach used over the last 50 years is to measure the contact angle, and then with existing precise measurements of the liquid-gas surface tension σ^{LG} solutions for σ^{SG} and σ^{SL} can be evaluated, if these two unknowns are correlated with the help of an additional equation [29]. There are three separate immediate problems arising from this. Firstly, the equations correlating the two solid-related surface tensions were found to be inaccurate in some cases [30]. Second, and most importantly, this way of tackling the equation does not resolve it for the contact angle that is actually looked for in this work. Lastly, the solid-related obtained values and the contact angle connected to them is a sort of material property, but will still be "strongly" dependant on the roughness of the surface [29].

These findings led to believe that the most reliable approach to set a contact angle would be to take a value measured by other researchers and not mesh it with mathematical formulations and assumptions. The values considered for this work are reported and cited in Table 5. Please note that finding these values was difficult and they come out of different works which may use differently treated glass surfaces. The implications of this will be discussed in the conclusion.

Table 5: Measured contact angles on untreated glass for different liquid-gas combinations

Liquid-Gas combination	Contact angle [-/°]
Water-Air	50 [31]
Ethanol-Air	60 [20]
Oil-Air	40 [32]

The Oil analysed in the paper [32] has a high level of asphaltenes (11 %), making it a heavy crude oil, which is important for the determination of the liquid properties later.

At this point it should be stated that another decision that has to be made is whether the contact angle should be considered as static or dynamic. This is connected to the physical observation that the droplet will have a different contact angle when the liquid front is moving with a radial velocity [20]. This is not to be confused with different static contact angles with the wall when liquid is advancing by increasing its volume through the addition of more water, hence spreading out radially, versus when it is receding by removing it. In this case the difference lies within the three-phase contact line being between water/air/dry-surface (advancing), and water/air/wet-surface (receding) [33].

Such models that have also been validated over different sets of parameters could be dynamic contact angle models, like one extended with the Cox-Voinov theory [34]

$$\theta_{dyn} = \arccos\left[\cos\theta_{eq} - \frac{\zeta Ca}{\mu} - C_{pin}\frac{\tanh C \cdot Ca}{\gamma}\right] \tag{29}$$

Where ζ is a friction constant, C is a smoothing coefficient, and C_{pin} another coefficient that also serves for dimensional consistency, the rotational speed is implemented through the capillary number Ca. Another mathematically more complex model was introduced by Hoffmann in 1975 and has been used in studies that compared simulated to experimental results obtaining a good fit during the spreading process [20]. Theoretically, adding such a model in Fluent is possible, as the contact angle can be written as a function also depending on internal variables like radial velocity.

Some people with a lot of experience try to dismiss those formulations in Fluent's official forums, saying that some scientists go against this and see the use of dynamic contact angle models in CFD as controversial. No papers claiming this were found, but it was still chosen not to implement one of the formulations in order not to overcomplicate the work. Adding this layer of complication and additional variable did not seem suitable for the scope of the second part of a master's thesis.

2.4. Mesh refinement study

To be able to properly evaluate a solution with mesh independence, it is necessary to go through various refinements and analyse global and local flow variables whilst assuring appropriate residual curves. When approaching a VOF problem like this, the first thing coming to mind might be to incorporate some type of adaptive meshing on the cells, which is why this was tried to be added on top afterwards.

To be able to talk about the meshes the analysed cases are quickly summarized in Table 6.

Table 6: Analysed meshes

Acronym	Description	Cell side length	Cell count
(a)	coarse	0.2mm	3720
(b)	medium	0.08mm	20592
(c)	fine	0.04mm	78834
(d)	coarse adapted	0.05mm – 0.2mm	9300
(e)	medium adapted	0.04mm – 0.08mm	24342

Preliminary tests assessing the calculational time were conducted, and after a careful analysis of the produced contours and results, it was decided to further investigate the results of meshes with a side length of 0.2 mm to 0.04 mm and two strategically refined versions of the meshes with cell side lengths 0.2 mm and 0.08 mm. As the first three refinements produce the same type of mesh only one of them is presented as an example in Figure 57; the manually refined ones correspond to Figure 58 and Figure 59.

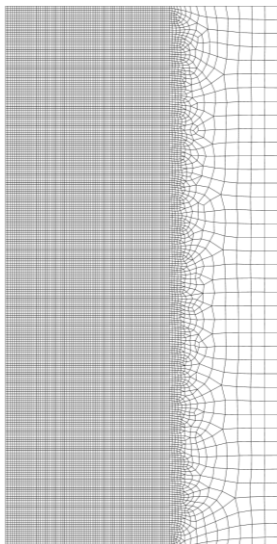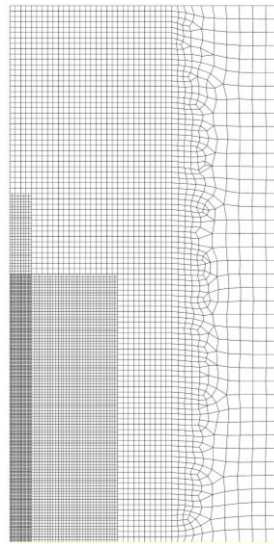Figure 57: Mesh with cell side length of 0.08 mm

Figure 58: Manually adapted mesh with cell side lengths between 0.05 mm and 0.2 mm
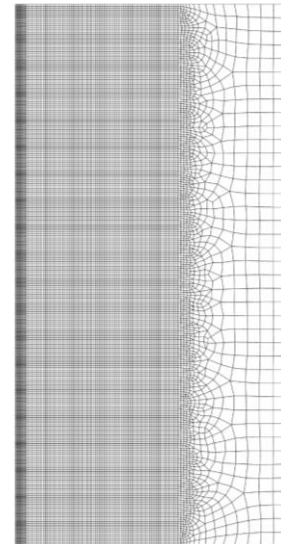
Figure 59: Manually adapted mesh with cell side lengths between 0.08 mm and 0.04 mm

The idea behind the partial static mesh refinement in Figure 58 is to increase the resolution close to the wall, which is where the energy from the rotation will be transferred to the fluid

and a thin boundary layer will be created in the end. The general idea of letting the zone close to the pressure outlet more unrefined is done to save computational time on the one hand, but also assure the calculation domain is big enough to avoid possible unphysical effects coming from the boundary conditions either. The two main parameters taken to judge the mesh independence are the global variable of force exhibited on the wall by the fluid and the local variable of the curvature of the fluid at multiple given points. As the problem is being assumed as globally laminar a discussion about the y^+ value is obsolete, as the assumption of a globally constant viscosity holds.

2.4.1. Total force exhibited on the wall

Evaluating a value that is summed over many different cells allows to get a number that does not depend only on one cell which might suffer from a numerical flaw in that instant. For this reason, evaluating the total force exerted by the fluid on the wall is an interesting metric. Fluent can output this force at every time step, and we can hence print its trend over time.
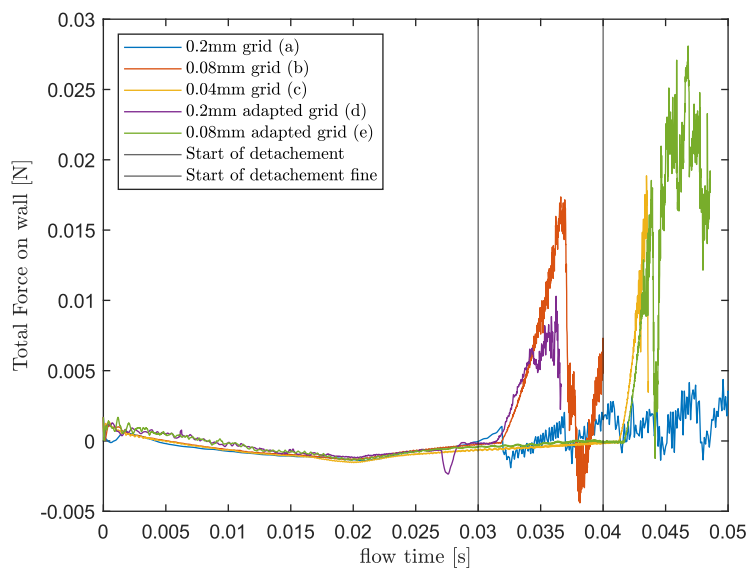
Figure 60: Total Force on wall over time

In the starting phase the coarse mesh differs strongly from the others. After around 2 ms the result gets closer to the one presented by the medium and fine mesh, while the adapted ones show higher forces. Although all cases were calculated with a constant time step size of 1e-5 s the finer meshes tend to show a more zig-zag line, while the coarser ones present a more smoothed-out behaviour at the beginning. After around 10 ms the medium and fine mesh start to slowly drift apart slightly, with the medium mesh showing a slightly higher force with a similar temporal behaviour. The coarse mesh follows this general behaviour too, although with smaller fluctuations. At around 27 ms, the coarser manually adapted mesh shows a drop of the force that is recovered quickly after. Looking at the contours at these instants does not

hint towards a change of the resolution of the zone of the mesh the fluid is finding itself in, and therefore cannot be directly explained. The instant around 30 ms is where the fluid front starts to detach in some mesh variations, exhibiting a "fingering" behaviour as shown in the literature and in Figure 53. After this, the medium and coarse adapted resolution show a similar rise pattern, while the coarsest one rises less. The fine 0.04 mm grid does not present fluid detachment yet, it comes later with a later rise in force, the same is valid for the 0.08mm grid adapted to 0.04 mm close to the wall. Looking at the contours at these instants, this behaviour is coherent with the beginning of the detachment of the islands as presented in Figure 61
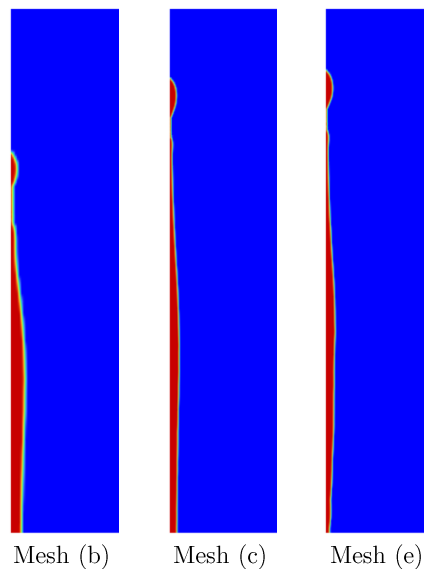
Figure 61: Contours around the instant of island creation for three different meshes
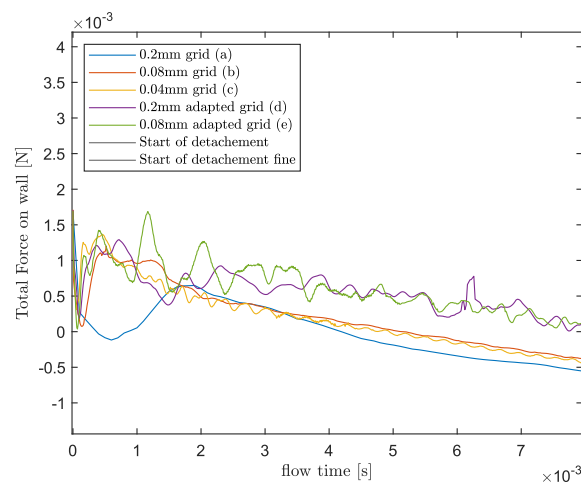
Figure 62: Total force on wall over time, initial phase zoomed in

After a short settling phase in the first few milliseconds where the effects probably building up to the detachment do not express themselves a lot, the percentual difference in force between the fine and medium mesh reaches a maximum value of around 15 %. Where both the fine medium and fine mesh show forces of around 0mN varying by less than 15 %, the adapted ones show forces around 0.48 mN and the coarse one around -0.22 mN.

2.4.2. Interface inclination at three points and general phase contours

A local variable could be the inclination angle of the two-phase interface. The problem is that this interesting solution variable is not easily accessible through the solver. Even though Fluent somehow computes the curvatures of the surfaces required for the surface tension calculation with the Young-Laplace equation (14), there is no direct way to output them. They also do not provide an explanation of how to get this angle in the documentation, but by making a few geometrical considerations a possible approach was elaborated.

We know that as for the definition of the gradient in a two-dimensional plane one can write

$$\nabla \phi = \left(\frac{\delta \phi}{\delta x}\right) \imath + \left(\frac{\delta \phi}{\delta y}\right) \jmath \tag{30}$$

Geometrically this can be visualized as follows
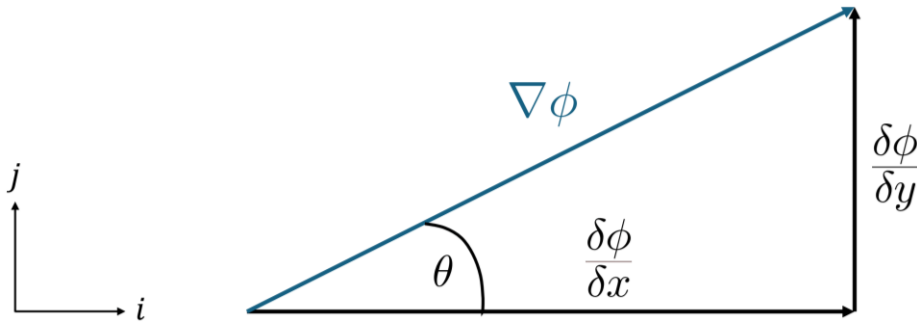
Figure 63: Visual representation of the gradient

Hence, the opposite side of the angle can be related to the hypotenuse being the gradient by taking the magnitude of both and writing

$$|\nabla \phi| \cdot \sin(\theta) = \left|\frac{\delta \phi}{\delta y}\right| \leftrightarrow \theta = \arcsin\left(\frac{\left|\frac{\delta \phi}{\delta y}\right|}{|\nabla \phi|}\right) \tag{31}$$

The gradient in y-direction and the magnitude of the gradient of the volume fraction can be computed on a straight line for every time step, in this case being $x = 0.15$ mm. For a single time instant the distributions can be seen in the next figures.
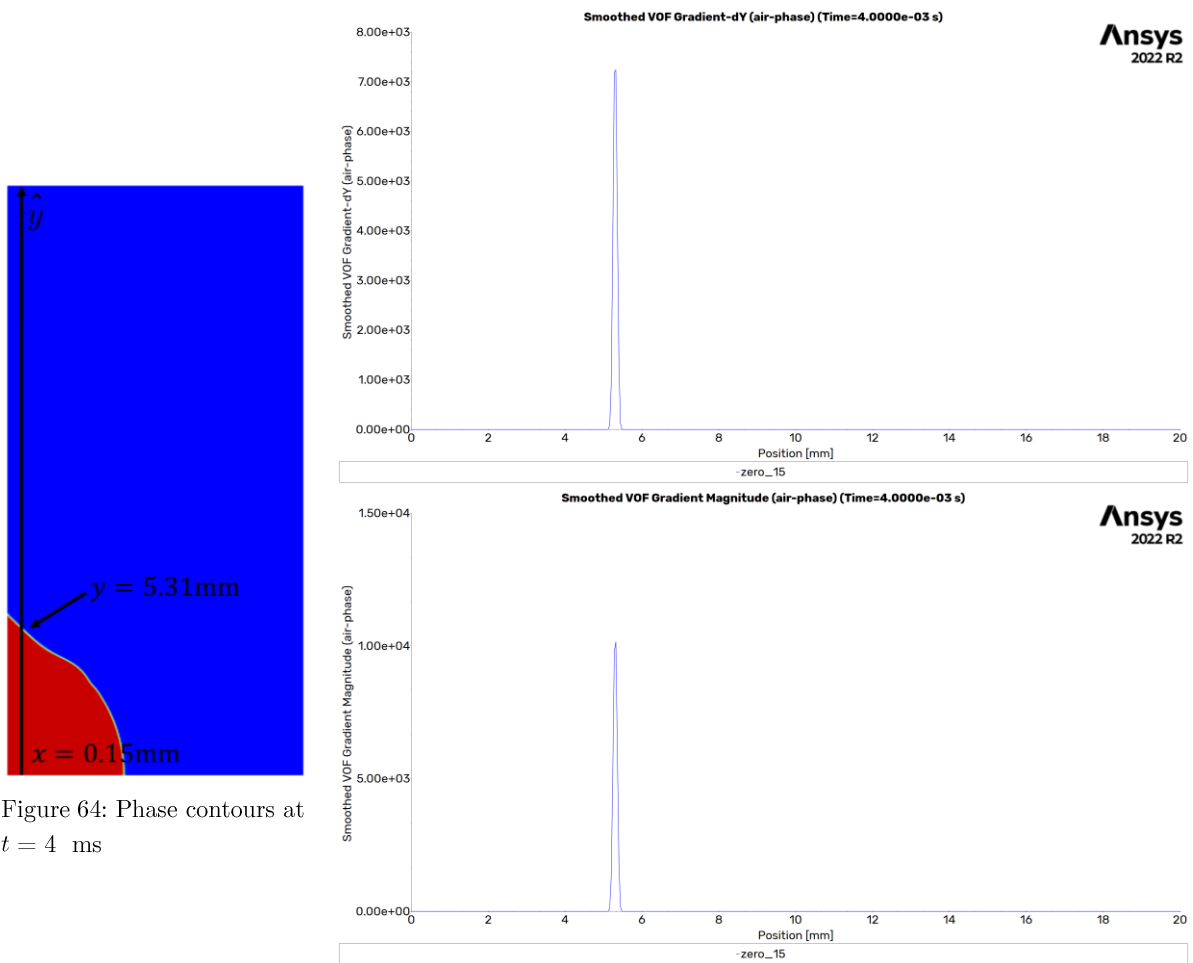
Figure 64: Phase contours at $t = 4$ ms

The manuals don't elaborate how the "Smoothed VOF Gradient" is calculated, but it is visible that the obtained peaks correspond to the central part of the interface. It is possible to output the maximum of the gradient in y-direction as well as its magnitude at every time step, and by inserting these values into (25) we are left with an angle of about

$$\theta \approx \arcsin\left(\frac{7}{10}\right) \approx 44.43°$$

Which is coherent with the graphical result visible in the contour plot. By writing a short script in MATLAB, this procedure can be automated. Applying it to all the different analysed meshes leads to the following result useful for the determination of mesh independence.

The case setup chosen to evaluate the forces and inclination angles was the one depicted in Figure 65, which includes a high-speed rotation and the effect of gravity on the not yet steady-state Water droplet.
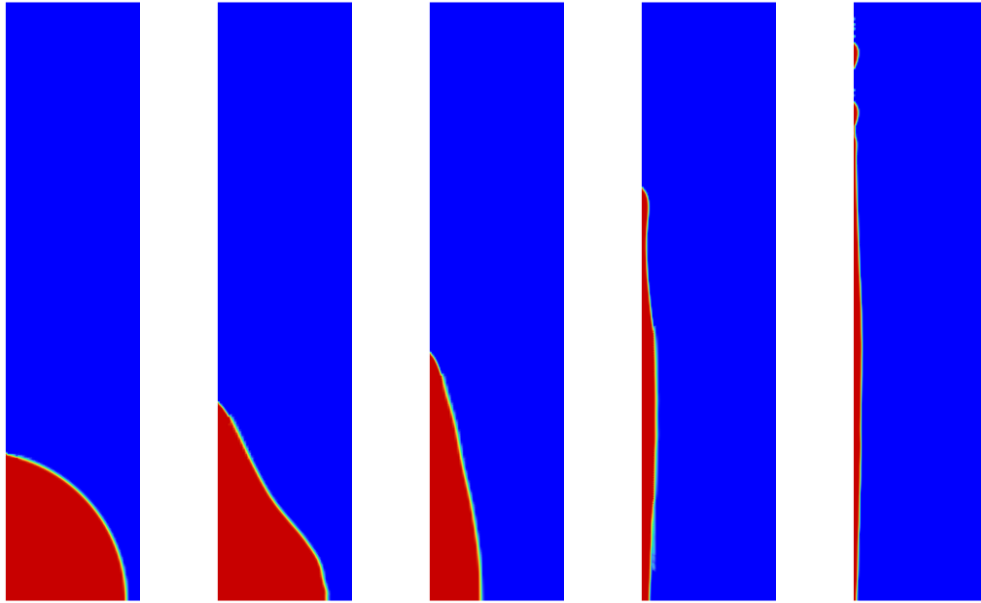
Figure 65: Simulation setup implemented for the angle detection during the mesh analysis. The liquid is Water with the wall rotating at $\omega = 250$ rad/s, going from $t = 0$ s to $t = 0.4$ s

To visualize the locations where the angles are taken from, it can be helpful to take a look at a zoomed in picture.
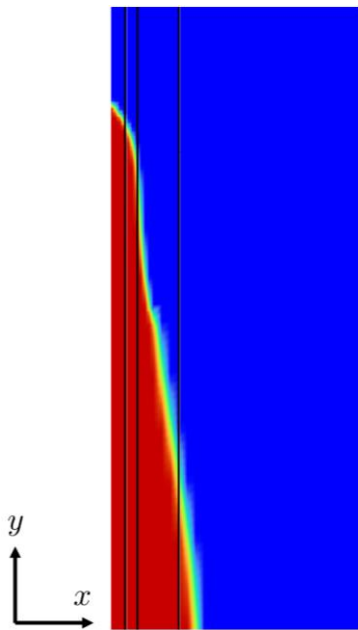
Figure 66: Zoom into the domain with three marked x-locations
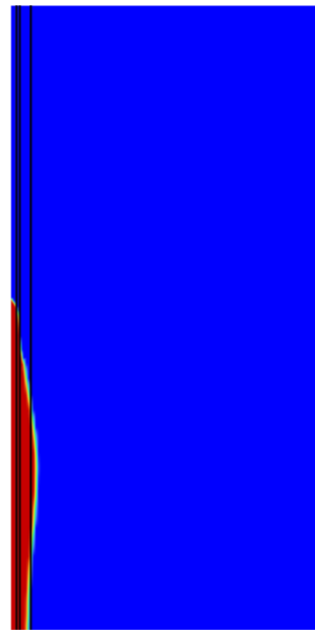
Figure 67: Full view of the domain with three marked x-locations

This helps with the interpretation of the results, even though this is not the primary point of this detected variable. If one would want to be sure not to wrongfully detect the angle of satellite droplets, or cut out the cases where the liquid volume fraction is too low, the algorithm in combination with the Fluent macro presented in 2.7 would have to be adapted and implemented into this script. As a full representation through e.g. MATLAB of the surface at every time instant is not necessary since Fluent outputs the contour plots, this would go far beyond the point of this analysis.
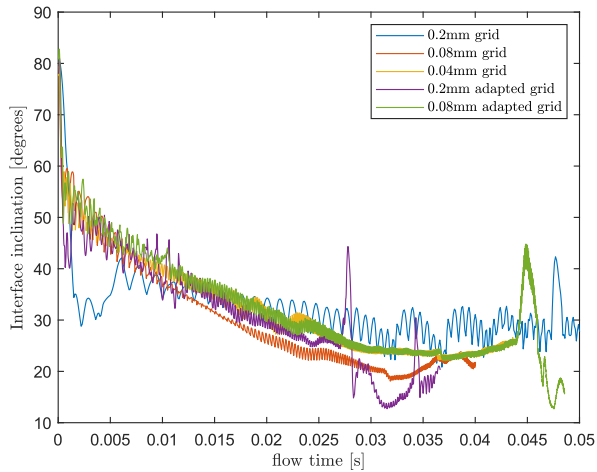
Figure 68: Angle at $x = 0.15$ mm
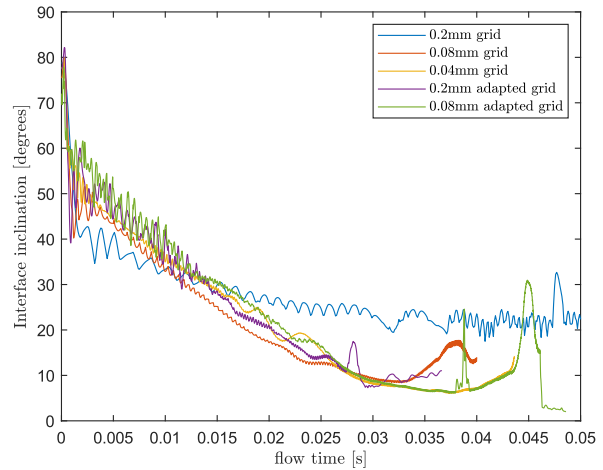
Figure 69: Angle at $x = 0.25$ mm
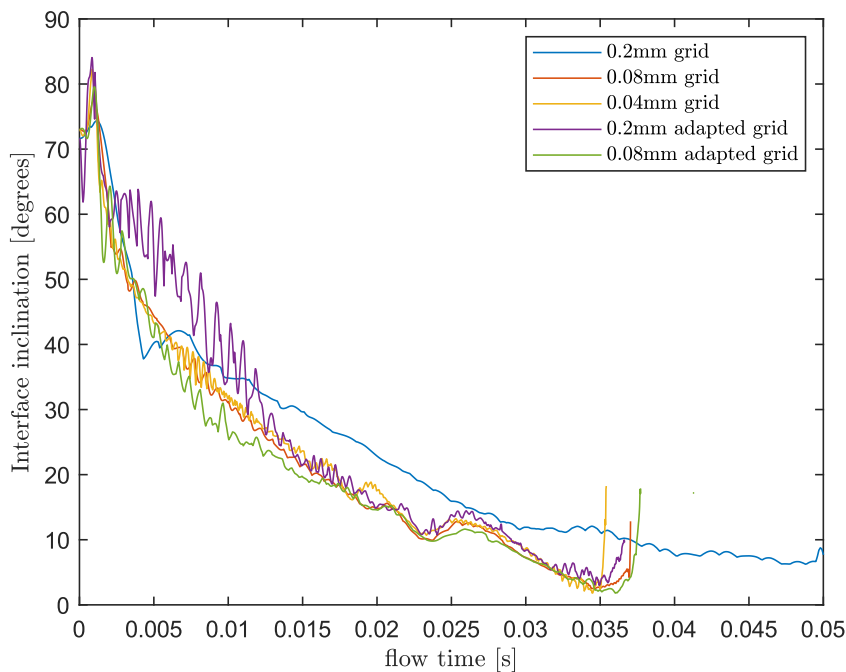
Figure 70: Angle at $x = 0.65$ mm

The angle obtained by the two variants of the coarse 0.2 mm mesh differ strongly from the ones obtained with all the finer meshes at all three observed distances from the wall. In the region close to the wall, the adapted 0.08 mm grid gives basically the same results as the 0.04 mm grid, while further away from the wall at $x = 0.65$ mm their values tend to differ more. The relative error between the two referring to the fines 0.04 mm mesh as baseline is expressed in the following Figure 71 and is low enough to be acceptable.
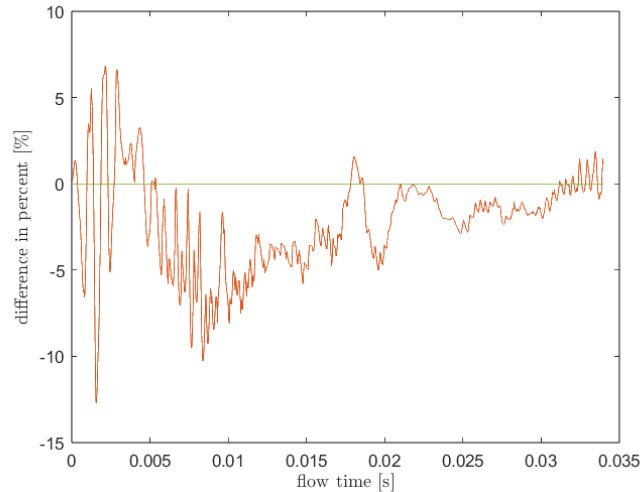
Figure 71: Relative difference between the full 0.04 mm mesh (c) and the 0.08 mm mesh adapted to 0.04 mm cells close to the wall (e) at $x = 0.65$ mm
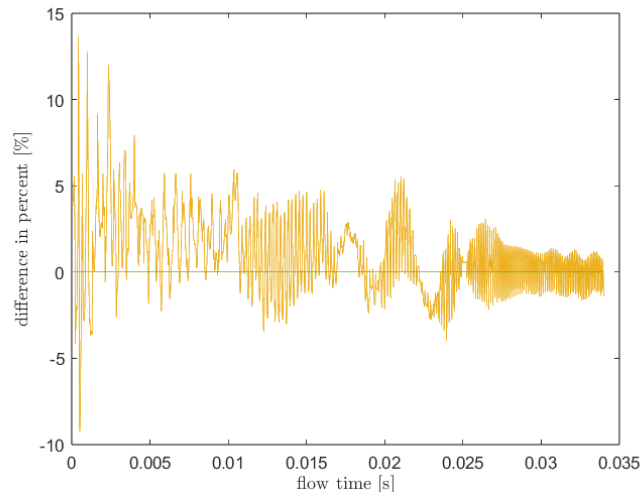
Figure 72: Relative difference between the full 0.04 mm mesh (c) and the 0.08 mm mesh adapted to 0.04 mm cells close to the wall (e) at $x = 0.15$ mm

Summarizing the results it is possible to state that the finest mesh leads to a representation of the fluid film closest to the one seen in literature, has the liquid front detaching the latest and produces the thinnest liquid layer. Other scientists witnessed films as thin as 15 µm for ethanol on glass [20], making us believe that choosing even the finest refinement with cell sizes of 40 µm might still not be enough to fully represent the real phenomena. As the provided computational power is very limited, choosing the 0.08 mm mesh adapted to 40 µm close to the wall seems like the most suitable option, since it produced much of the same results with only one third of the cells.

This finally chosen mesh (e) has a total cell count of 24342, and due to the central section consisting solely of perfect squares, has ideal mesh metrics (skewness, aspect ratio, orthogonal quality) in the zone most relevant for the simulations.

2.4.3. Residuals

The last and very important factor for judging convergence is checking the residuals. As already explained in the chapter 1.1.2 under solver settings, Fluent keeps track of the scaled residuals of the continuum, momentum and swirl-equation. By outputting and formatting the console output correctly, it is possible to plot these values over the course of the whole simulation.

It must be made sure that the solution iteratively converges to the set tolerance of 1e-5 lying two whole orders of magnitude below the standard proposed by Fluent within the maximum of 40 iterations per time step imposed by us. If this were not to be the case, either the time step would have to be decreased or the number of iterations per time step increased. In the following figures, the evolution of the residuals over the first initial 1300 time iterations, as well as other 300 iterations in the middle of the simulation, are reported.
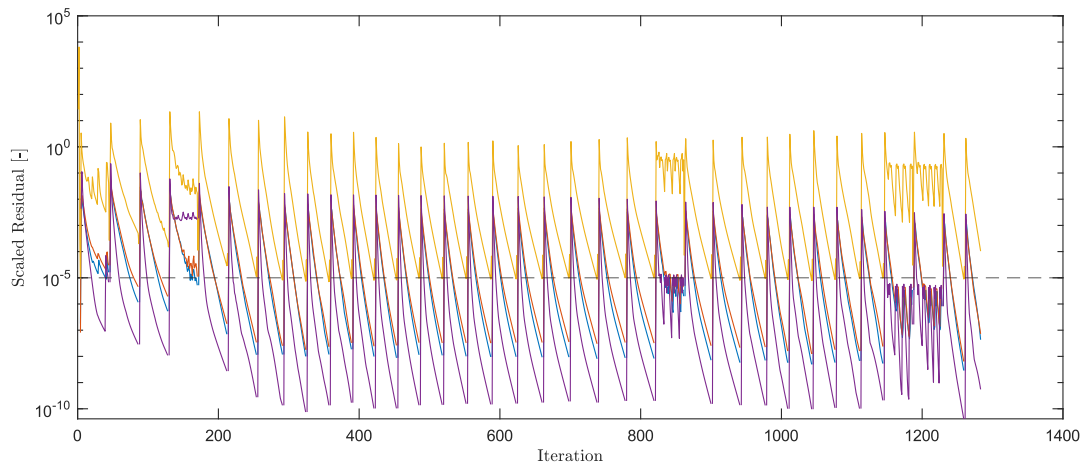
Figure 73: Residuals over the first 1300 iterations
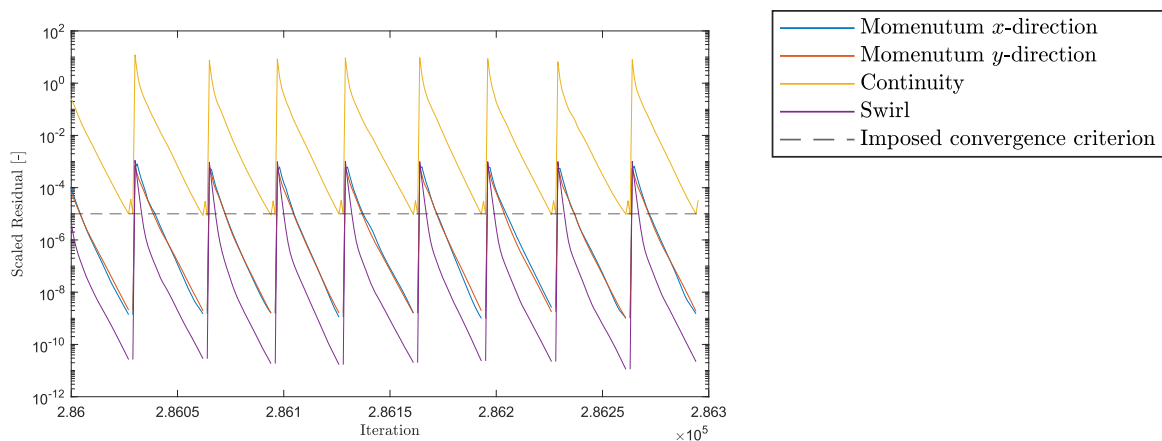
Figure 74: Residuals between the iterations 286000 and 286300

We can see that the residual of the solution becomes small enough within the imposed iterations and limits, and apart from some minor fluctuations at the beginning the general behaviour of the curve is what one would expect from a well executed simulation result.

2.5. Determination of the initial profiles

The initial profile of the sessile droplet will be depending on the fluid properties relevant for the calculation of the surface tension as well as the imposed wall adhesion angle. For this reason, it is not possible to simply assign an initial shape to the droplet in a stationary state, but is has to be calculated by the simulation itself. Figure 75 shows the evolution starting from an initial round droplet shape with radius R_0, ideal for setting a fixed liquid volume and assuring relatively rapid convergence. It shall be noted that as the simulation was setup as axisymmetric, wherever mirroring the phase contours at the x-axis does not substantially enhance the understanding of the solution, this wasn't done to keep the figures more concise.
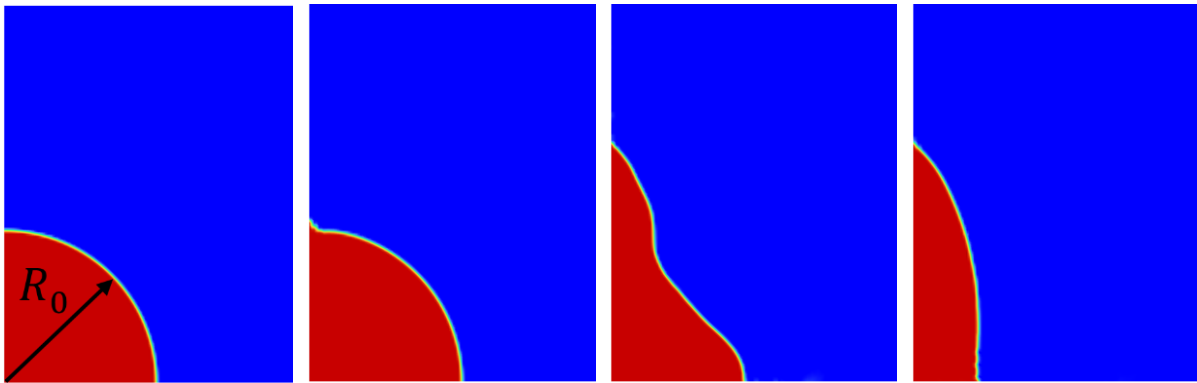
Figure 75: Evolution of the liquid profile over the course of two seconds leading to an almost stationary solution

After two seconds all the three liquids come to a pretty stationary solution. The part close to the symmetric boundary condition continues to fluctuate a bit, but the fluid further out the radial direction and in contact with the wall boundary condition does not move significantly anymore. In order to be able to quantify a point where the solution has reached a steady state, plotting the evolution of the radially furthest out point over time can be done. Doing this requires a short algorithm in MATLAB and the implementation of macros in Fluent and is hence not trivial, but will be explained more in detail in the following chapters.
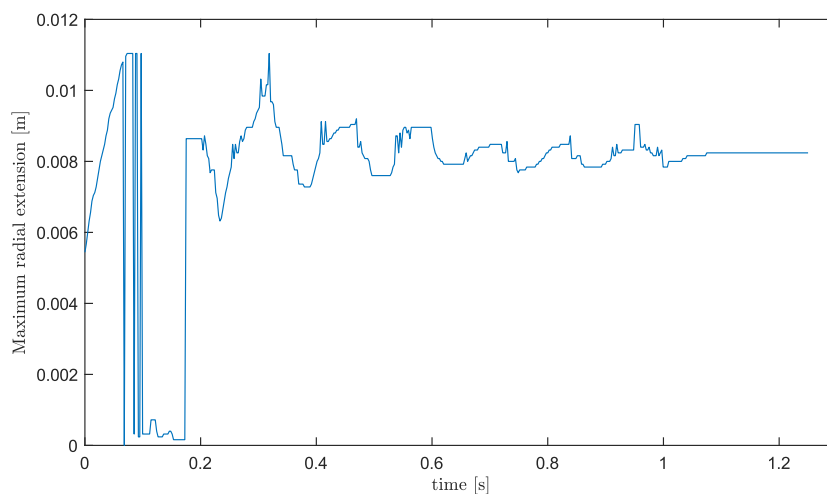
Figure 76: Evolution of the liquid front over time for a R = 5 mm Water droplet

It becomes evident that after around 5000 iterations corresponding to more or less $t = 1.3$ s, the front portion in contact with the wall crucial for the simulation does not fluctuate any longer. This analysis was done with the initial profiles of all three examined liquids and led to satisfying results which can be checked in Appendix 7 and Appendix 8 for the cases of Ethanol and Oil.

2.6. Implementation of automatic adaptive meshing

As shortly mentioned before, VOF approaches are textbook examples for the implementation of automated adaptive meshing techniques. As computational power is always a major concern, figuring out additional ways to speed up the calculation process while possibly even enhancing the accuracy of the solution was a very welcome tactic. Fluent's automatic mesh adaptation lets the user set a minimum edge length up to which the algorithm can refine the cells if deemed necessary, the frequency in time steps at which the refinement is carried out, as well as the coarsening and refinement criteria based on the volume fraction α_{liquid} present in the cells. It is also possible to set the number of cells closest to the wall as additional refinement/coarsening criteria, in an effort to always capture the interface as well as the wall region as precisely as possible.
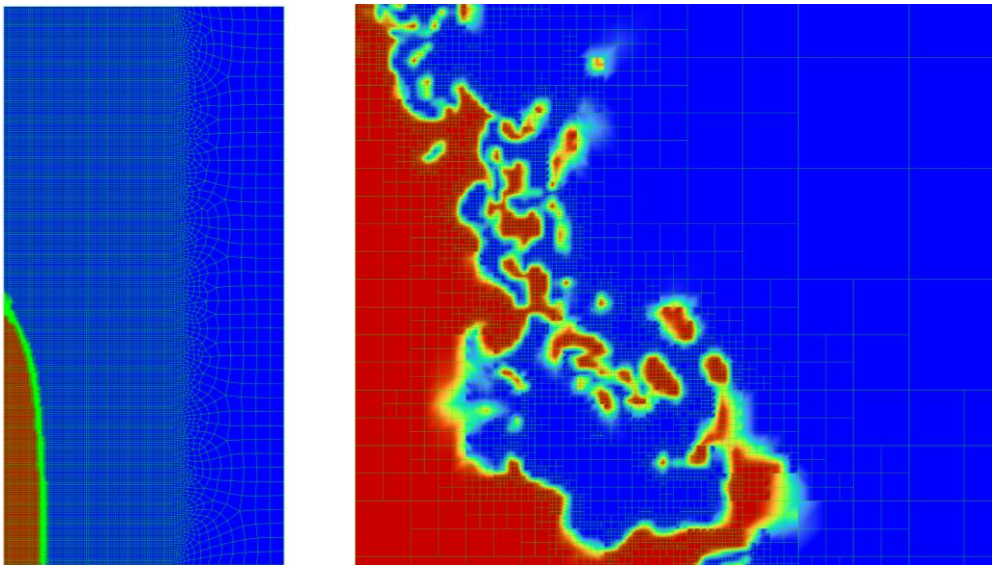
Figure 77: Contour of the two phases with a zoom to the part close to the wall where the high swirl speeds occur for the case of oil on the glass surface spinning at $\omega = 250$ rad/s

The local courant number for the VOF specific interface treatment was still kept at 0.25, leading to adapted time steps which should be small enough to assure a stable solution, but for all three analysed liquids it was simply not achievable. Adding the stabilization mechanisms described in 1.4.3 was also tried, but the solution still diverged in the first instants. A look at the swirl velocities revealed a similar behaviour as already experienced during the analysis of the capillary tube
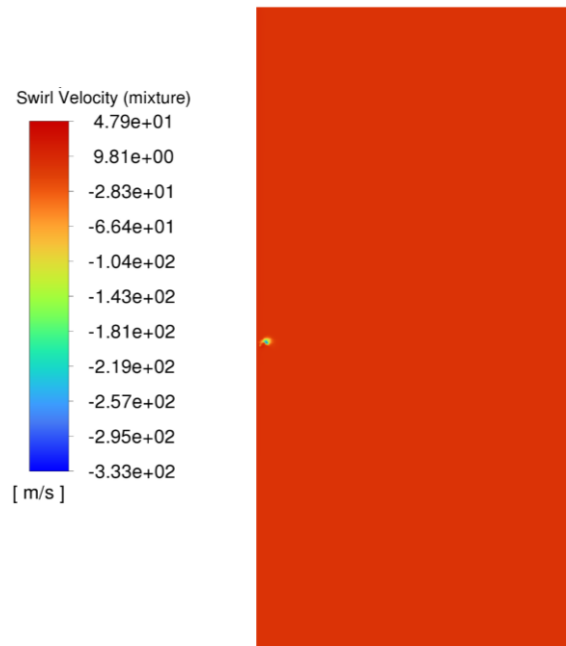
Figure 78: Contour of the swirl velocities at the instant of divergence for the case of oil on the glass surface spinning at $\omega = $ 250 rad/s

A possible solution could be to allow the solver to go even further down with the adaptive time steps, but at this point the drawback in computational time would not be able to outweigh benefits of a potentially more precise result anymore. An additional factor ruling out the continuation of this path were the stability issues encountered in the analysis of the capillary tube in the first part, possibly connected to numerical issues with swirl speed calculations in two-phase flows with fluids that exhibit big viscosity ratios. Due to these reasons, adaptive meshing was ruled out and all the calculations were performed with the previously decided on, constant grid (e) with an a priori performed refinement in the region close to the wall that added about +20 % to the total cell count with respect to the non-adapted 0.08 mm cell length case.

2.7. Results at constant Bo_r

With a set mesh and initial profiles for the stationary sessile droplets established simulations with the glass surface actually rotating can be carried out. One interesting metric is the previously explained rotational Bond number

$$Bo_r = \frac{\varrho V \omega^2}{\sigma} \qquad (19)$$

Solving the simulations for three different liquids while implying the same rotational bond number requires to impose the correct corresponding rotational speeds, as all the other parameters are material properties. The material properties are resumed in Table 7

Table 7: Properties of the liquids, data from Perry's Engineering Handbook at 20 °C [10]

	Kinematic Viscosity [kg m^{-1} s^{-1}]	Surface tension [N m^{-1}]	Density [kg m^{-3}]
Ethanol	0.001074	0.022	789
Water	0.001003	0.072	998.2
Oil [35]	0.287	0.037	870

The values for oil have been taken from another source, as the higher level of asphaltenes used in the study to determine the contact angle usually point towards higher densities.

Given that the three compared droplets all have a radius of $R = 5$ mm and the angular speed for the case of water is set to $\omega = 400$ rad/s being around $\omega_{rpm} = 3816$ rpm, Bo_r will be

$$Bo_{r,\text{Water}} = \frac{\varrho_{Water} \, V \, \omega^2}{\sigma_{Water}}$$

$$= \frac{998.2 \frac{\text{kg}}{\text{m}^3} \cdot \left(400 \frac{\text{rad}}{\text{s}^2}\right) \cdot (0.005\text{m})^3 \cdot \frac{2\pi}{3}}{0.072 \frac{\text{N}}{\text{m}}} = Bo_{r,Ethanol} = Bo_{r,oil} \approx 580$$

Please note that only half of the sphere's volume was considered, as the initial droplet laid onto the surface is characterized precisely as such. By doing a quick algebraic manipulation, it is now possible to impose the angular speed required to get the same dimensionless number with the other liquids

$$\omega_{\text{Ethanol}} = \sqrt{\frac{Bo_r \sigma_{Ethanol}}{\varrho_{Ethanol} V}} = 248 \text{ rad/s}$$

$$\omega_{\text{Oil}} = \sqrt{\frac{Bo_r \sigma_{Oil}}{\varrho_{Oil} V}} = 307 \text{ rad/s}$$

These numbers were specifically chosen to all lie within the normal range of angular speeds used in spin coating processes.

One interesting quantity to plot is how the maximum radius over time for three different liquids depends on Bo_r.

At this point, it must be explained how the maximum radius being the furthest radial extension of the interface is computed. There is no such command as "output the coordinates of the radially most outward VOF cell with an $\alpha_{liquid} = 1$ value" in Fluent, so a reliable and automated solution had to be developed. The thought process is similar to the one applied for the determination of the surface inclination earlier.
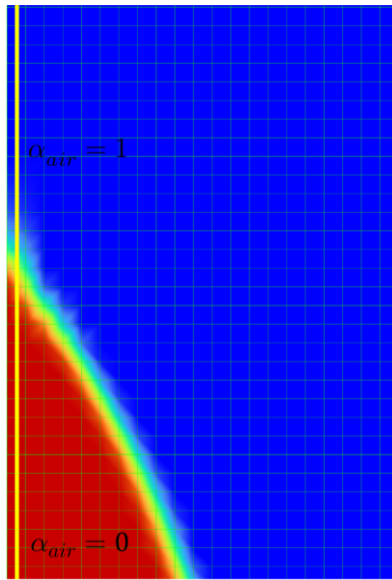
Figure 79: Line through first cell
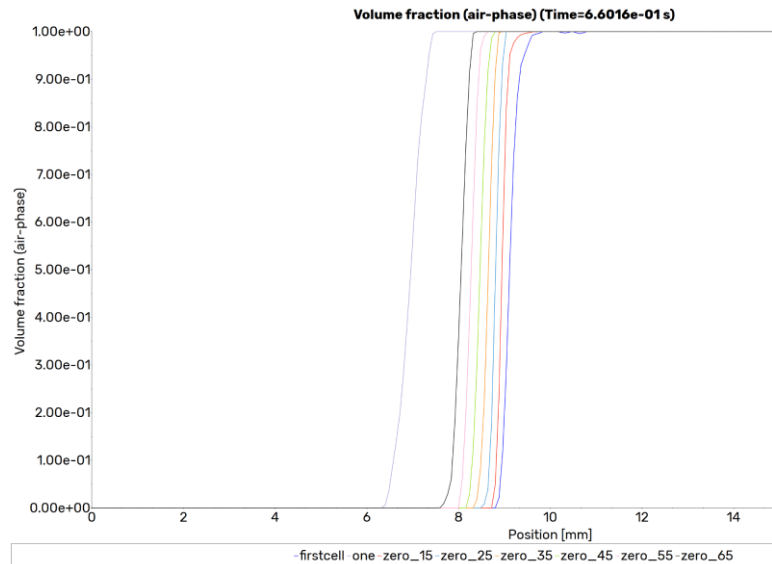
Figure 80: Volume fraction over y-coordinate for different x-values

Remembering the concept of the VOF theory, each cell has a volume fraction assigned to it that lies between one and zero. It is possible to set a line through the first cell, and then output the volume fraction at every coordinate of that line for every time step. The cutoff has to be chosen as the distribution on the interface follows a trend as shown in Figure 80 and was set to $\alpha_{liquid} = 0.5$ for the purpose of this work. By setting up an algorithm in MATLAB that reads the file Fluent output containing a coordinate and associated α_{air} value every tenth time step starting from $y = 0$, the progression over time can be plotted. The way the algorithm is set up is that is reads the y-position of the cell (the x-position is intrinsically given and is simply the first cell touching the wall) at the first value of $\alpha_{liquid} < 0.5$ starting from $y = 0$. Setting it up this way around assures that the island droplets don't lead to false results for the maximum extension of the actual liquid front. For the sake of easier replicability of this work, the TUI command creating the macro to output the correct data as well as the MATLAB code used to elaborate this are added to the Appendix 6.

The results for the three liquids listed above at their respective Bond numbers can be seen in the subsequent Figures.
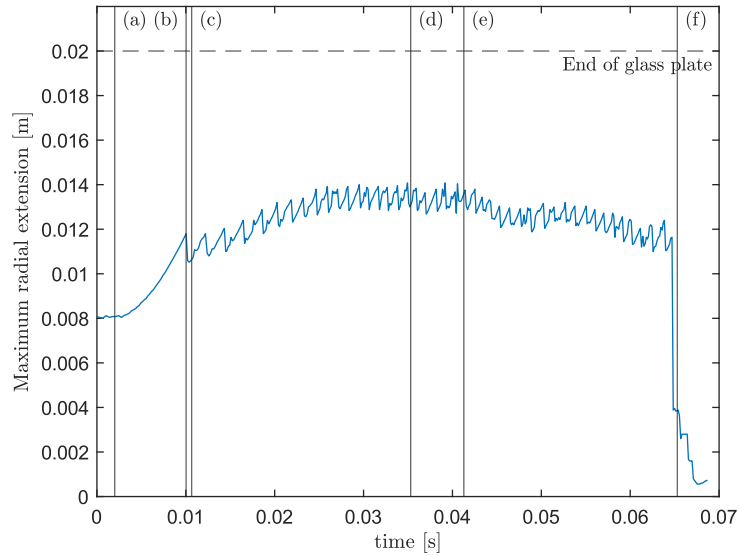
Figure 81: Progression of the diameter for a 5 mm Water droplet at $Bo_r = 580$
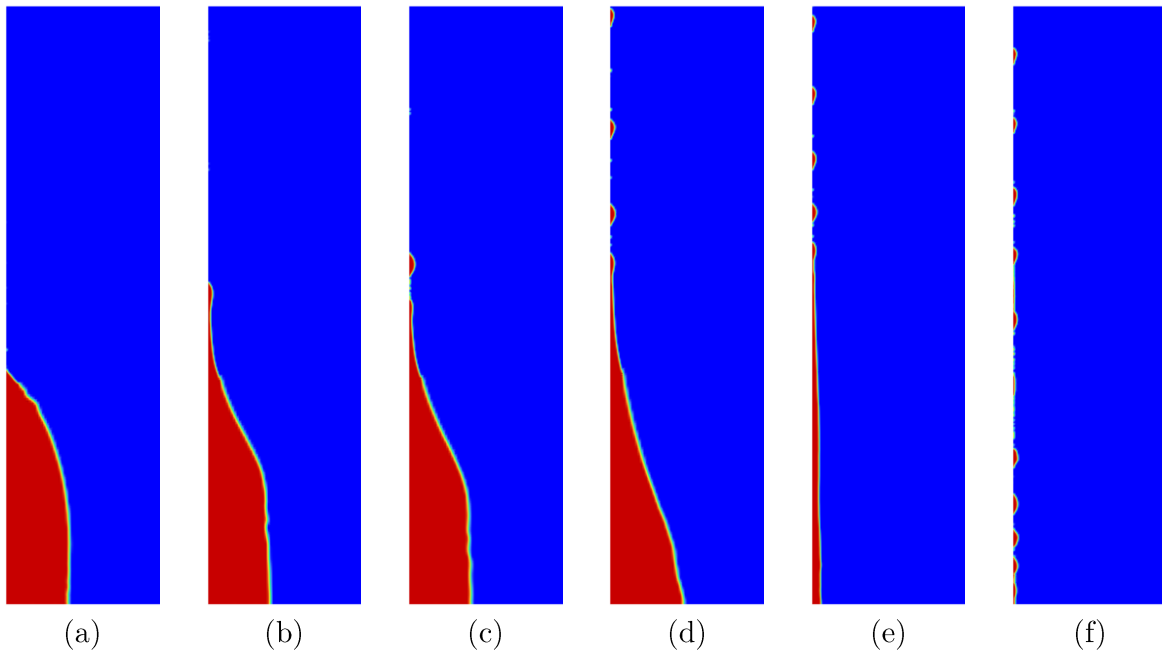
Figure 82: Progression of the Water droplet over time on the rotating surface at $Bo_r = 580$

Looking at the phase contours next to the automated radius detection algorithm, it becomes clear that it is capable of depicting the transient evolution of the liquid front accurately and efficiently. The at first stationary water front moves radially outwards due to the centripetal force and drags liquid along with it, reducing the total amount of liquid left at the centre. The form of the liquid front best seen in (b) is coherent with results from literature [20]. Over time, all of the liquid starts being dragged off the surface, ultimately leaving the clean glass slate without a layer of water on top. The coherence of this results with empirical values will be further discussed in the conclusion.
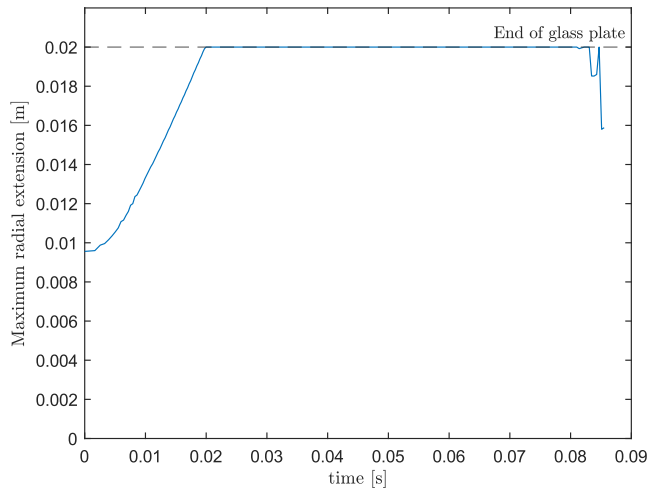
Figure 83: Progression of the diameter for a 5mm Oil droplet at $Bo_r = 580$
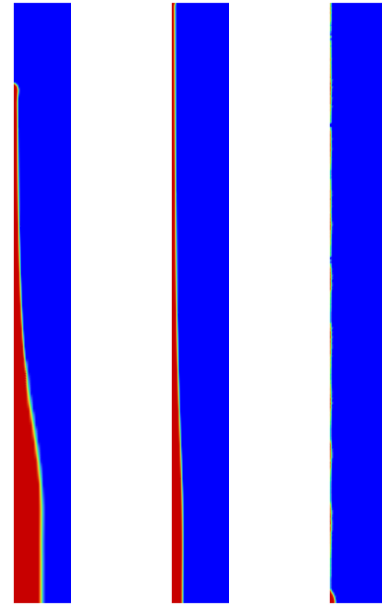
The Oil droplet is capable of expanding further than the Water and Ethanol and in the range of up to 20 mm does not show any fingering instability. In the final instants, the surface will still get rid of its coating entirely.
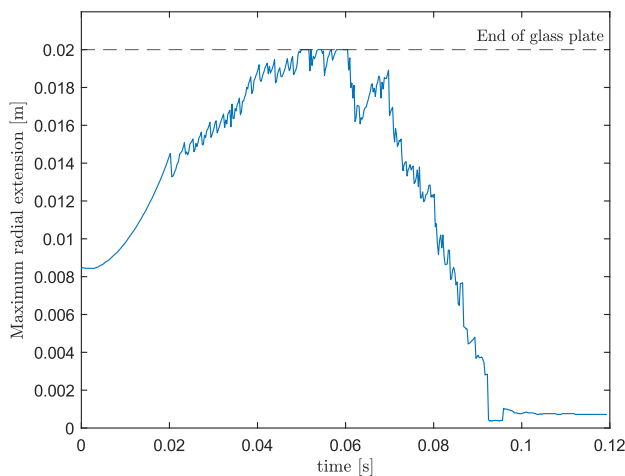
Figure 84: Progression of the diameter for a 5 mm Ethanol droplet at $Bo_r = 580$
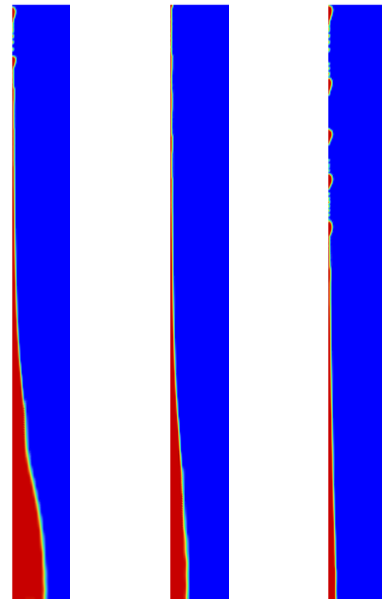
The Ethanol droplet reaches the end of the glass plate too, but also exhibits fingering instability throughout almost the whole simulation. The biggest radial extension of Ethanol starts retracting at around 55 ms, compared to around 80 ms for Oil and 63 ms for Water. At the same Bo_r the maximum radius before fingering instability occurs at the following values, when the approach presented in Table 8 is applied:

Table 8: Maximum radii before island detachment for the three 5 mm droplets

	$R_{\max}$ [mm]	R_{adim} [-]
Ethanol	14.07	2.81
Water	11.53	2.31
Oil	>20	>4

2.8. Comparison of different liquids at constant Oh

Another way to compare the different fluids is to look at their spreading behaviour at a constant Oh during for example three different rotational speeds leading to a change in Bo_r. The Ohnesorge number was defined as

$$Oh = \frac{\mu}{\sqrt{\varrho\sigma L}} \equiv \frac{\mu}{\sqrt{\varrho\sigma R_0}} \qquad (20)$$

Where the characteristic length is defined by the initial radius of the droplet. By doing a few calculations with the algebraically modified equation

$$Oh = \frac{\mu}{\sqrt{\varrho\sigma R_0}} \rightarrow R_{0,\text{equivalent}} = \frac{\mu^2}{\varrho\sigma Oh^2} \qquad (32)$$

it becomes clear that considering the viscosities, surface tensions and densities of the three fluids Oil will always have the largest equivalent diameter and Water the smallest one.

Setting a diameter of $R_{\text{Ethanol}} = 5$ mm leads to Oh ≈ 0.036456, and this number to equivalent diameters of $R_{\text{Water}} = 1.05$ mm and $R_{\text{Oil}} = 14.8$ mm. The problem here is that for the fluids previously chosen in this work, the diameters differ so vastly that it is not possible to simulate the three within the same calculation domain. For this reason, it was not possible to include the Oil droplet in this part of the simulation. Regarding the Water droplet the determination of the initial profile had to be carried out again first. The scheduled simulations for the comparison can be summarised in the following Table 9.

Table 9: Simulation schedule for $Oh \approx 0.036456 = \text{const}$

	$\omega = 200$ rad/s	$\omega = 300$ rad/s	$\omega = 400$ rad/s
Water (1.05mm)	(I)	(II)	(III)
Ethanol (5mm)	(IV)	(V)	(VI)
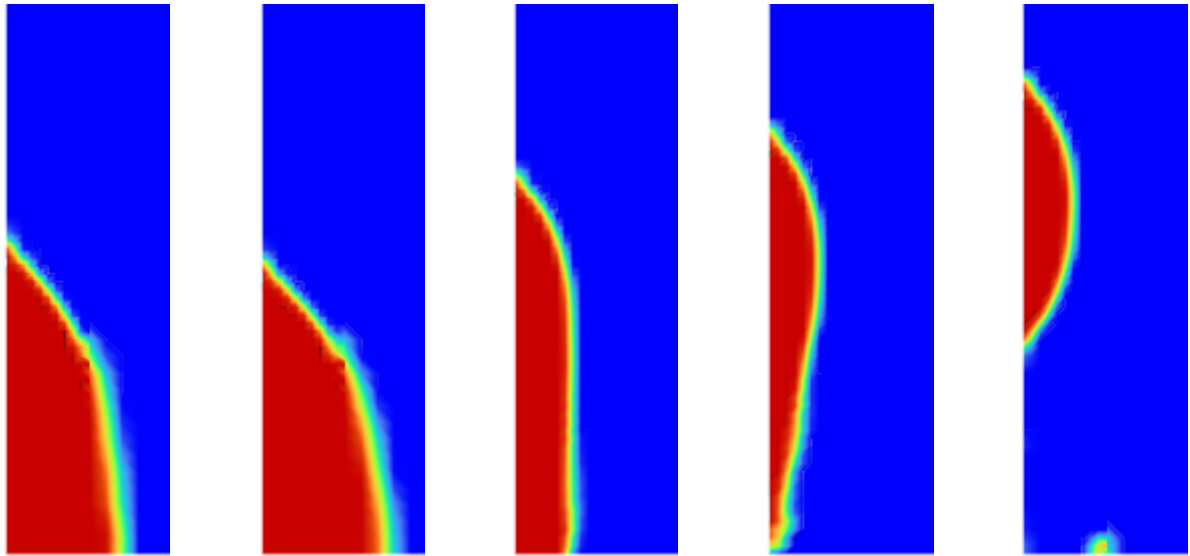
Figure 85: Stationary profile

Figure 86: After 0.1 s, $\omega = 200$ rad/s

Figure 87: After 0.08 s, $\omega = 400$ rad/s

Figure 88: After 0.82 s, $\omega = 400$ rad/s

Figure 89: After 0.86 s, $\omega = 400$ rad/s

Shortly after the instant represented in Figure 89 the simulation with $\omega = 400$ rad/s diverges, the simulation result presented in Figure 86 with $\omega = 200$ rad/s seems to not change significantly from its initial shape and does not move out radially at all. The Water droplet in Figure 89 has lost a considerable amount of volume, a droplet leaving towards positive x-direction is visible on the frame. For the sake of comparison, the simulated time in these cases was longer than for the complete evolution of the $R_{\mathrm{Water}} = 5$ mm droplet analysed in the previous chapter portrayed in Figure 81 and Figure 82.

The centripetal force decreases towards the centre of rotation with the power of two, making at least the numerical result more understandable, but the calculations are still too far away from a physical result that could've been compared to the $R_{\mathrm{Ethanol}} = 5$ mm case. As increasing the size of the Water droplet would have made the Ethanol droplet too big for the domain as well, this comparison had to be dropped. The approach of adimensionalizing R_{max} and plotting it for constant Oh will be attempted with another setup in the next chapter.

2.9. Results of Ethanol at different Oh and ω

Fingering instability is a phenomenon well known to spin coating that needs to be avoided for the sake of lower liquid consumption. To predict correct operational points of a real application it can be useful to determine the maximum achievable radius $R_{\max}$ without islands released from fingers. As $R_{\max}$ physically somehow depends on the amount of liquid being put on the surface, this parameter will be adimensionalized by dividing it by the initial droplet diameter R_0.

$$R_{\mathrm{adim}} = \frac{R_{\max}}{R_0} \tag{33}$$

Other ways of adimensionalizing will be discussed later with some literature. The simulation schedule looks as follows

Table 10: Simulation schedule for five changing Oh

	$\omega = 150$ rad/s	$\omega = 250$ rad/s	$\omega = 350$ rad/s	Oh
$R_0 = 5$mm	5A	5B	5C	0.00365
$R_0 = 4$mm	4A	4B	4C	0.00408
$R_0 = 3$mm	3A	3B	3C	0.00471
$R_0 = 2$mm	2A	2B	2C	0.00576
$R_0 = 1$mm	1A	1B	1C	0.00815

For each radius the determination of the initial profile had to be carried out again. Each case will be characterized by a specific Bo_r that increases from left to right, but within each row Oh is constant. Omitting the cases for $R_0 = 1$ mm which led to non-usable results for the same reasons already discussed above twelve simulation results can be summarized in the following scatterplot.
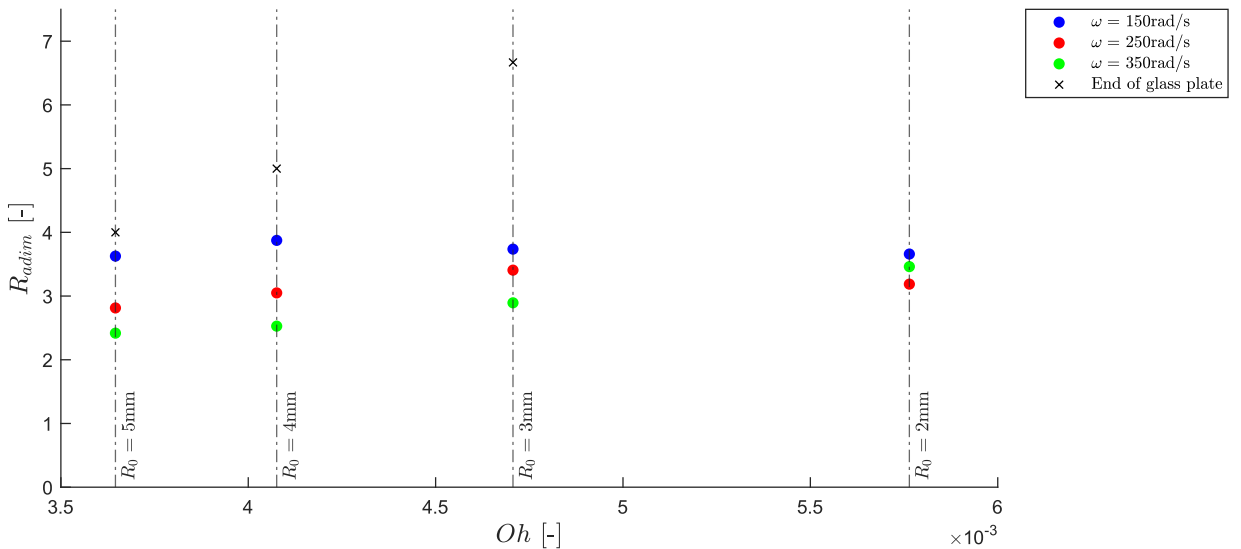

Figure 90: R_{adim} over Oh for three different angular speeds

The maximum reached radius before a fingering instability with island creation remains unchanged with increasing Oh. At $Oh =$ const an increasing angular speed means an increasing Bo_r, and in this direction it is possible to see a decrease in R_{adim}. The percentage of this decrease becomes lower when moving towards higher Oh.

To further interpret and assess these results, they will be compared to literature. A 2001 article by Wang & Chou [21] specifically analysing fingering instability studied the influence of various factors including the Bo_r on silicone oil droplets of varying viscosity. One of the conclusions from their study is the following diagram, to which the operating zone of the experiments carried out in this work have been visualized with the blue dashed lines.
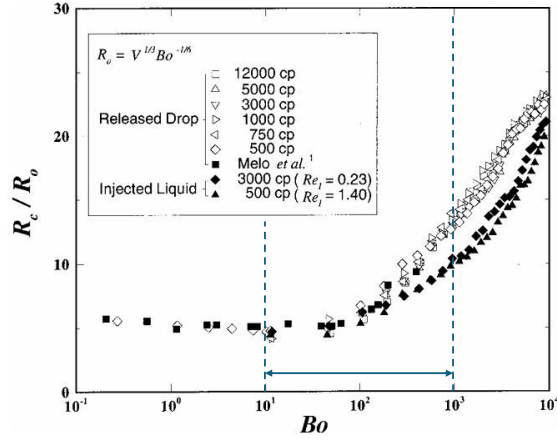
Figure 91: Dimensionless critical radius R_c/R_0 as a function of $Bo = \varrho\omega^2 V/\sigma$ [21]

Here cp stands for "centipoise", indicating that different droplets have different viscosities. It is worth indicating that the analysis by Wang & Chou was performed at $\omega =$ const for liquids of relatively high viscosities, as even the lowest analysed case of a silicon oil presented a viscosity of 500 centipoise equal to a kinematic viscosity of $0.05 \frac{\text{kg}}{\text{ms}}$, which is around fifty times higher than the one of Ethanol. The radius is adimensionalized by setting $R_0 = V^{1/3} Bo^{-1/6}$ as already done my Melo et al. [36], as this length scale leads to a better prediction at low Bo_r which is one of the key findings of the study, but it can also be done using a more intuitive length scale as shown in Figure 92.
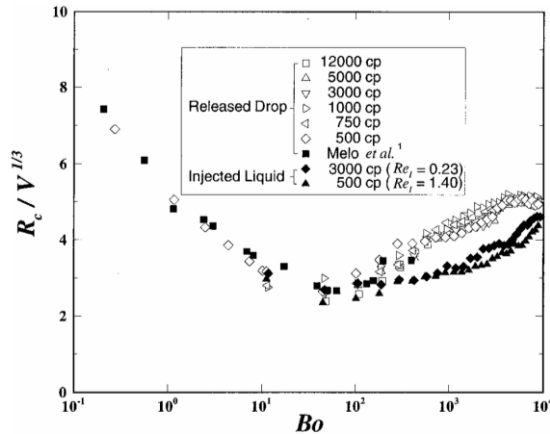
Figure 92: Dimensionless critical radius $R_c/V^{1/3}$ as a function of Bo for the injected liquid and released drop
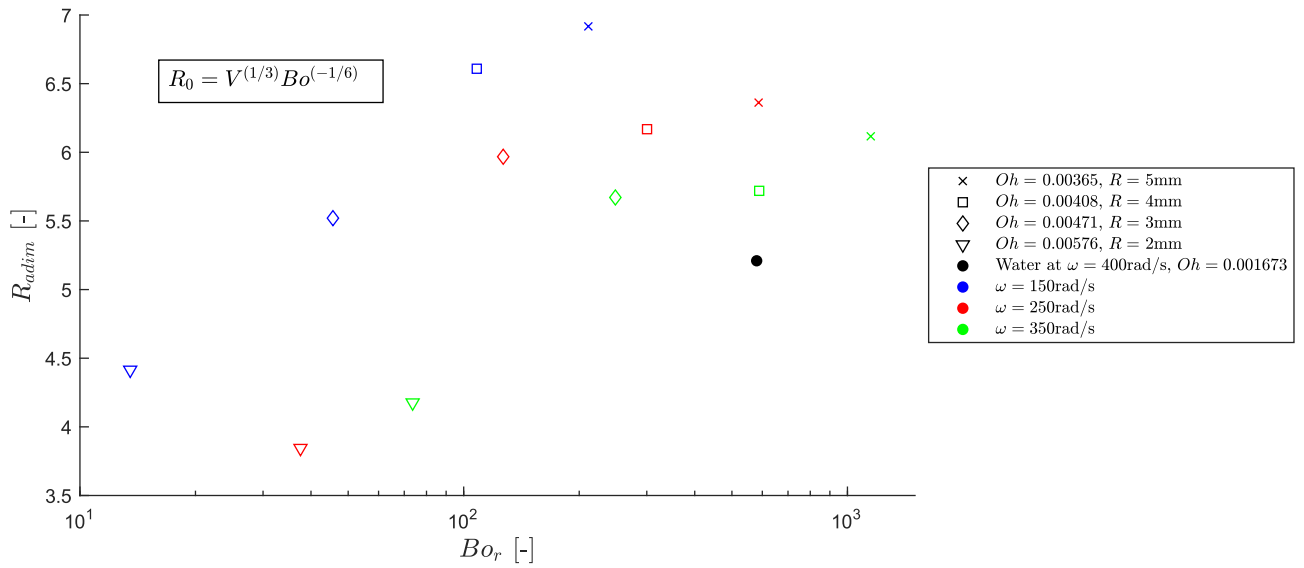
Figure 93: Simulated results using the same length scale to adimensionalize as used in [21], [36], Water droplet has same liquid volume as Ethanol droplet

Plotting the obtained results like this leads to a similar behaviour and values as seen in Figure 91 for the case of different silicone oils. Increasing Oh always leads to a decrease in the dimensionless radius. In the two cases with the highest Oh it seems like an increase in Bo_r does not consistently lead to a decrease in $R_{\max}$, but this effect is at least partially due to the y-axis depending on Bo_r too. Plotting the curves by normalizing with the length scale $V^{1/3}$ leads to
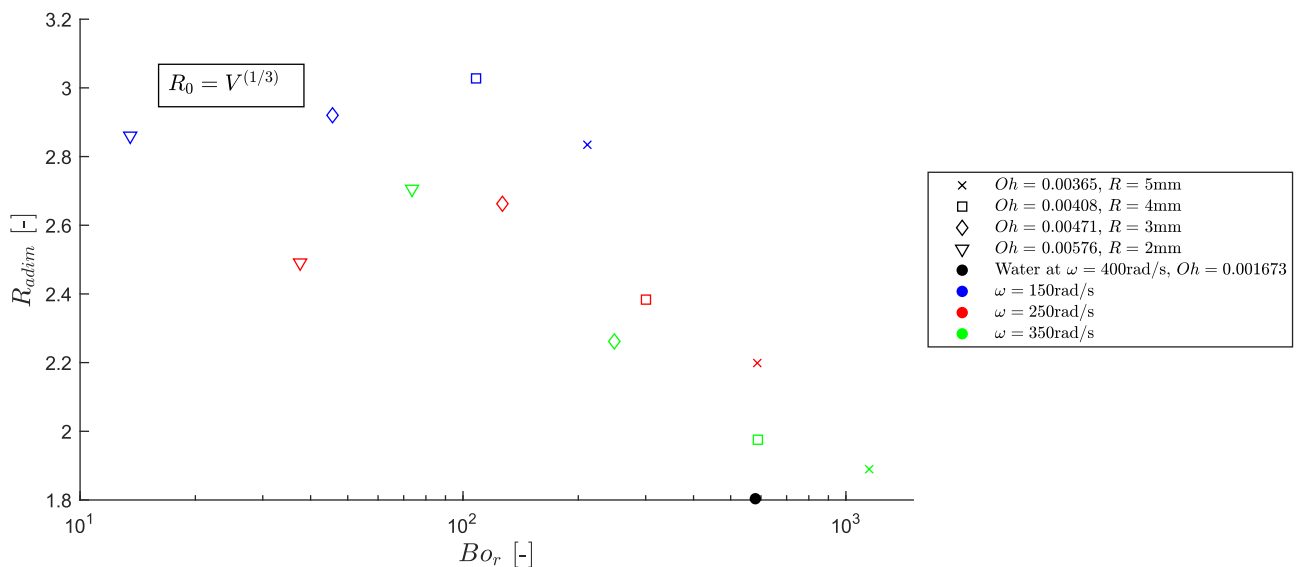
Figure 94: Simulated results using a length scale of $V^{1/3}$

Disregarding the $R = 2$ mm case the solution shows the same behaviour as seen in Figure 90, where at $Oh = $ const an increase in Bo_r leads to a reduction of the maximum achievable radius before fingering instability occurs.

2.10.   Impacting droplet: Effect of We

Another interesting experiment is the investigation of the droplets' behaviour when they are being let go from a predefined height, turning the problem into so-called dynamic spin coating. This leads to the liquid phase having a certain amount of x-velocity upon impact and will change the spreading behaviour. This part has to be considered as an addition to the previous analysis, as the dynamics change considerably. To assure consistency and comparability within the results, the non-sessile droplets will be defined to have the same liquid volume as their sessile counterparts. By keeping the angular speed of the glass substrate $\omega =$ constant this will lead to $Bo_r =$ constant, the changing parameter will be

$$We = \frac{\varrho v^2 L}{\sigma} \equiv \frac{\varrho v^2 R_0}{\sigma} \tag{34}$$

Where v^2 is the squared x-velocity upon impact and R_0 again the initial radius set for the droplet. It is to note that to assure $V_{\text{sessile}} = V_{\text{falling}}$ the initial radius of the falling droplet will have to be smaller compared to the sessile counterpart. Applying this condition leads to a $R_{0,\text{flying}} = 3.97$ mm compared to the sessile $R_{0,\text{sessile}} = 5$ mm. It is fair to assume the droplets form as spherical even though at this size they could lie closer to an oblate spheroid [37], as previous studies in similar size ranges showed "negligible" effects on the spreading radius for changing aspect ratios [20]. As a rough estimate not accounting for drag, the speed of impact of a $R_{0,\text{flying}} = 3.97$ mm droplet falling from a height h_0 of 30 mm would correspond to $v_{\text{impact}} = 0.76$ m/s, leading to $We \approx 85$. The different investigated impact speeds and resulting We are summarised in the following table

Table 11: Impact speeds and corresponding We

We [-]	v_{impact} [m/s]
2	0.1185
10	0.2650
30	0.4590
65	0.6757
85	0.7635
120	0.9181

The biggest number at $We = 120$ was chosen as previous research on water droplets found the speed of around $v_{\text{Droplet,Water}} \approx 0.919$ m/s to a 4 mm diameter to be firstly the terminal velocity of the droplet, and secondly the biggest possible radius before it breaks and splits into two minor droplets [37]. While these results cannot be directly copied for Ethanol, they are still useful to pose at least some kind of upper bound.

The initial velocities can be patched onto the spherical Ethanol droplet and the simulation begun. The results' phase contours as well as the plots portraying the evolution of the radially most outwards radius are summarised on the following diagrams and figures.
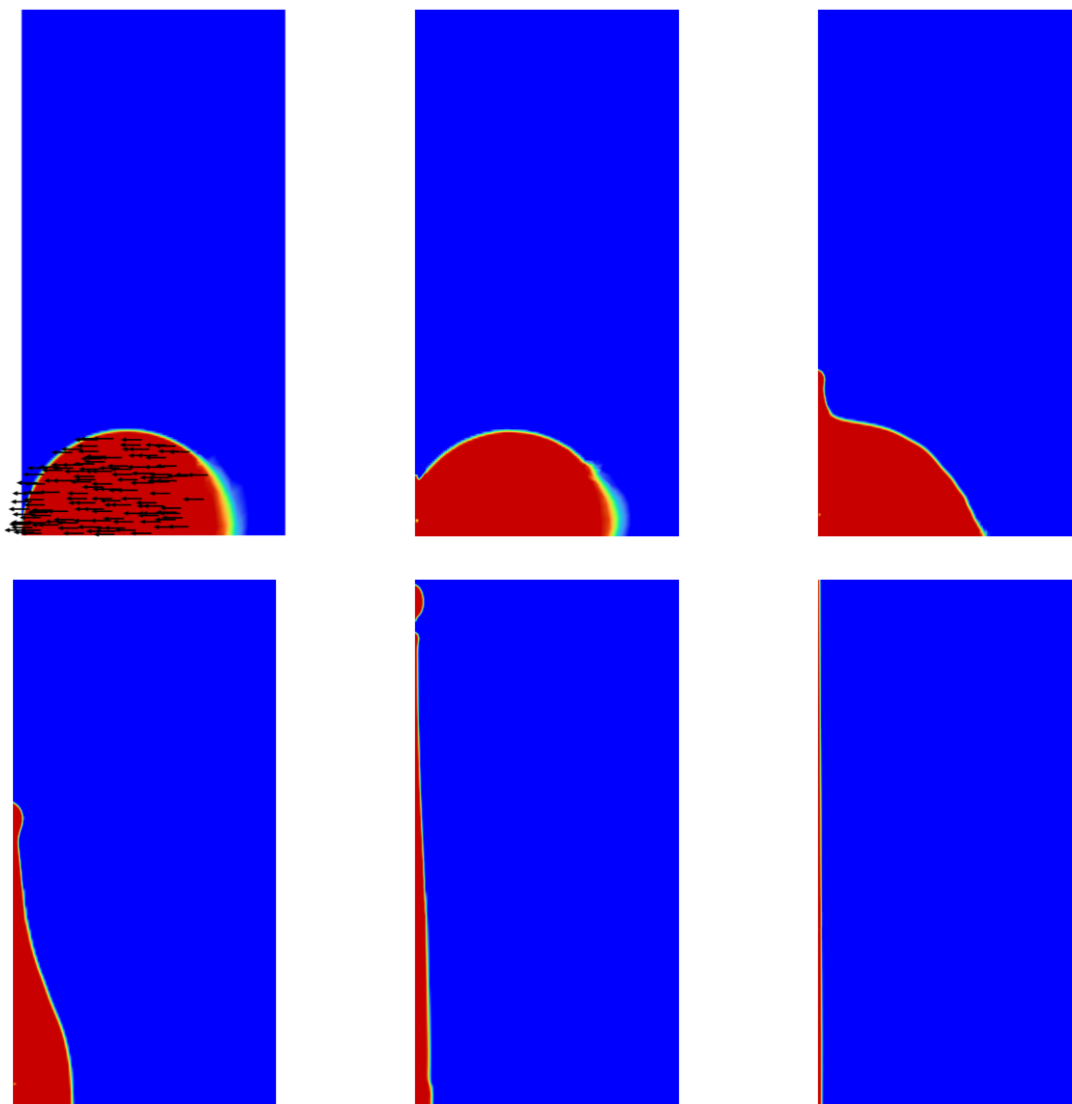
Figure 95: Evolution of the impacting liquid droplet over the course of around 50 ms, $We = 30$ and $\omega = 250$ rad/s; phase contours with velocity vector overlay in the initial time step
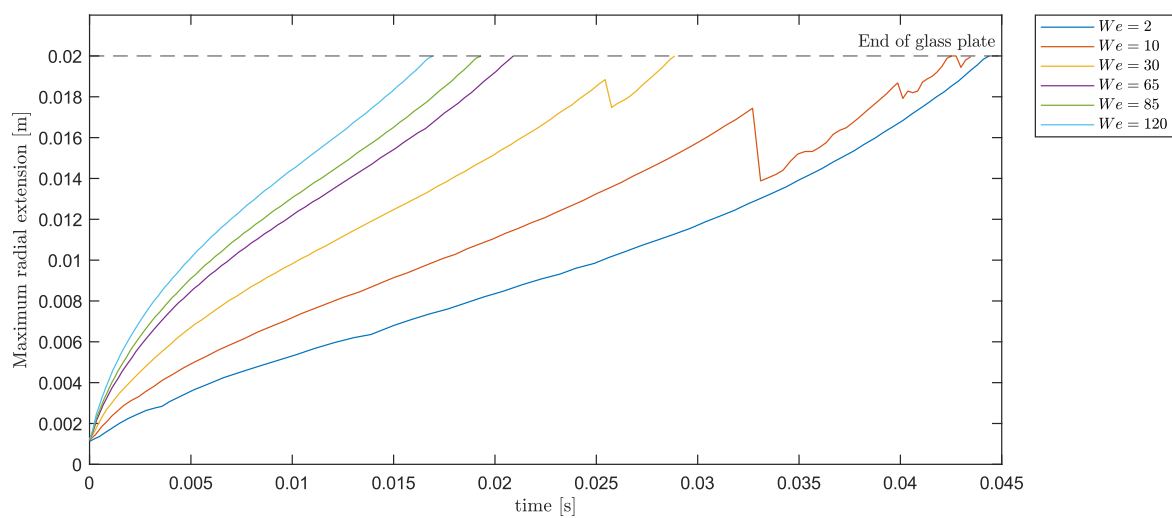

Figure 96: Spreading of Ethanol over time at $Bo_r = 587$ ($\omega = 250$ rad/s) for different We, $R_{0,\text{flying}} = 3.97$ mm

For the analysed cases an increase in *We* leads to reaching the maximum radial extension being the substrate's edge earlier. Depending on the imposed velocity the fluid's fingering behaviour also seems to change. While no islands are detached for the three cases with the highest and the one with the lowest *We*, the two cases in between show visible island detachment as also portrayed in the contour plots in Figure 95. This points towards a possible optimization problem. For comparison, the case of a sessile Water droplet at equal volume is added to the Appendix 9.

A final interesting analysis is to compare the spreading behaviour of Ethanol at a constant $We = 30$ with changing Bo_r as also done by Yuming et al. [20]. Their analysis lacks a proper characterization of the island creation though and thus still needs to be extended, as they chose a domain small enough to assure that fingering instabilities simply never occur. The results are summarized in the following Figure 97.
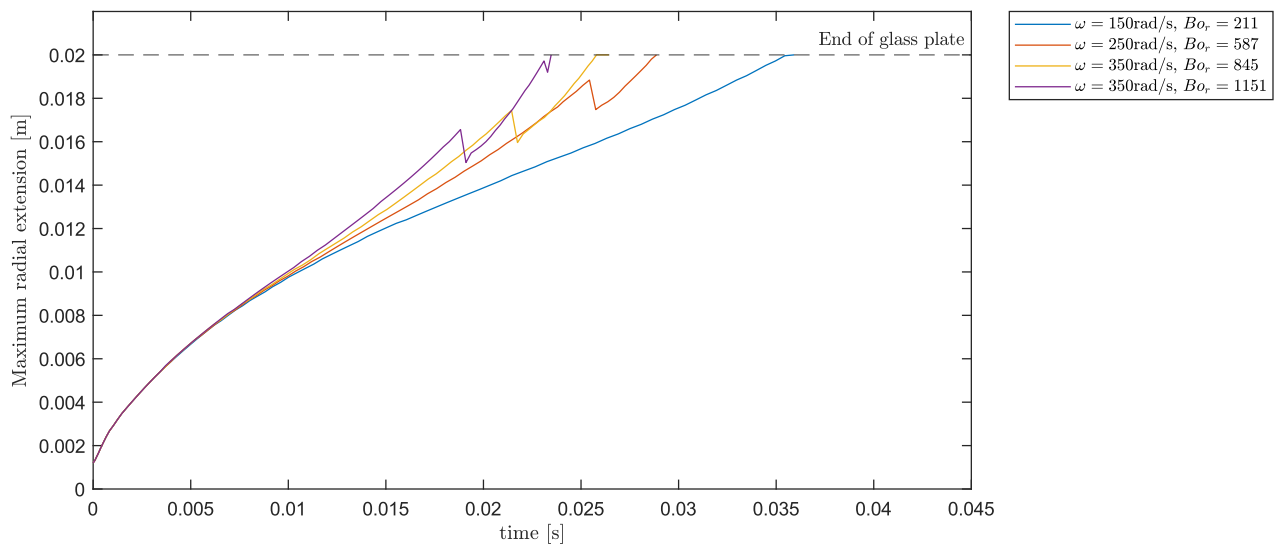
Figure 97: Spreading of Ethanol at different Bo_r, $We = 30$ at $R_{0,\text{flying}} = 3.97$ mm

The case with the lowest $Bo_r \sim \omega^2$ presents the biggest time to fully cover the substrate and does not have detaching islands, while the cases with higher angular speeds reach the end quicker, but also tend to have detaching islands sooner the faster the angular speed.

The initial phase results being independent from the substrate's angular speed and solely controlled by the impact velocity of the droplet.

2.11.   Conclusions and Outlook

An optimized mesh was attained and validated which provided a minimum cell height right next to the wall of 40 µm. The overall produced phase contours are in line with other results obtained by ADSA or numerical methods in the literature. When rotating the substrate long enough without having activated evaporation models, in the end there is no liquid left on the substrate, which does not reflect the reality of spin coating and tends to make believe that a finer resolution close to the wall would have been favourable. The assumption of laminar flow which mostly influences drying and evaporation behaviour seems to be unproblematic given the short times required for the whole spreading process. With the provided computational power it was not possible to refine the mesh even further to see how the liquid and the connected breakup processes would act, making it hard to estimate the accuracy as a whole. The determination of the initial profiles used for the simulations of the sessile droplets was a success, the only big variable lies within the careful election of the apparent contact angle. Surface treatments of the glass surface will significantly alter this value, meaning that for a correct comparison it would've been necessary to obtain the angles measured with the same method on the identical substrate. Automatic adaptive meshing had to be discarded as it led to stability issues. By setting $Bo_r = 580 = \text{const}$ at $R_0 = 5$ mm Oil was able to build up a non-fingering liquid layer over the whole substrate, while Ethanol took a lot longer and suffered from fingering instabilities, and for a single Water droplet it was not possible to fully cover the 20 mm long domain at all. While the substantially higher viscosity of Oil favours the liquid staying together, the lower density of Ethanol compared to Water makes it less prone to being drawn apart by inertia, as both liquids present comparable viscosities. Comparing different liquids at $Oh = \text{const}$ was not possible due to limitations in the size and resolution of the computational domain.

The detailed analysis of Ethanol as often applied organic solvent led to the conclusion that higher Bo_r may lead to significantly lower critical radii, while the change of Oh has no visible impact. By adimensionalizing in a suitable manner presented in the literature it was possible to partially recreate experimentally validated curves. The results in Figure 93 lie within the same dimensionless size range as the experimental results of previous research [21], [36] and expand their results by being evaluated at different rotational speeds. The Bo_r of a given fluid remains a function of the employed volume and the angular speed of the substrate, which leads to the key result of curves being shifted towards lower critical radii for higher angular speeds, but still following a similar pattern for changing volumes. To characterize this even further and expand the plotted range, more droplet sizes computed with finer meshes at different angular speeds would have to be analysed.

The implementation of dynamic spin coating shows optimization potential in terms of ideal combinations of *We* and Bo_r to minimize issues related to fingering instabilities and therefore minimize liquid usage. Higher *We* and Bo_r will always lead to a quicker coating, but certain combinations will lead to fingering instabilities. Judging from the phase contours, this method led to a more uniform liquid film with generally less island detachment involved.

Results with bigger droplets seemed more physical and followed the expected patterns better, with the 1mm cases not working at all. This could be again related to a non-sufficient mesh resolution close to the wall and liquid-air interface.

Future works could consist of a characterization of how exactly angular speeds high enough to be used in real applications change or shift the Bo_r-R_{adim} curve of Ethanol, and how these curves vary for different organic and inorganic fluids. This analysis could then be expanded by adding cases of dynamic spin coating, where for a specific application an optimum between *We* and Bo_r could be found to e.g. decrease the waste of toxic and expensive liquids like highly purified photoresist compounds used in the semiconductor industry. Prior to the actual simulations a method for the characterization of the apparent contact angle would have to be set, preferably through specialized equipment utilizing the previously described ADSA methods.
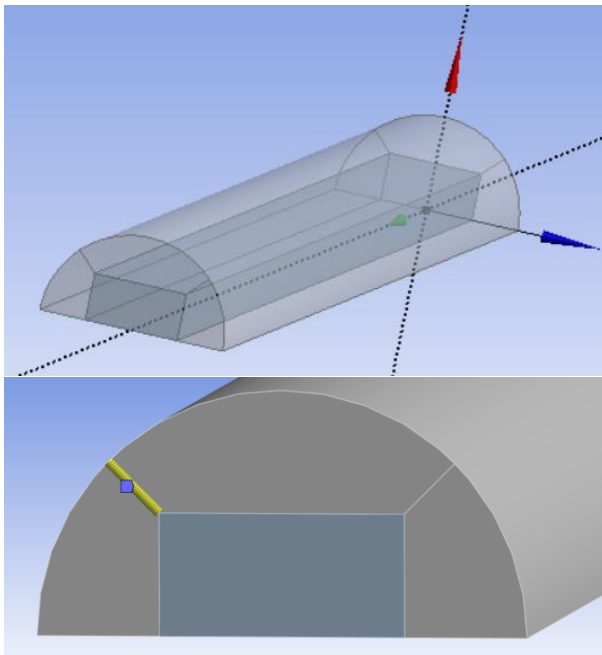
<center>**APPENDIX**</center>

i.   Appendix A

Appendix 1: Overview of changed settings when applying stability controls
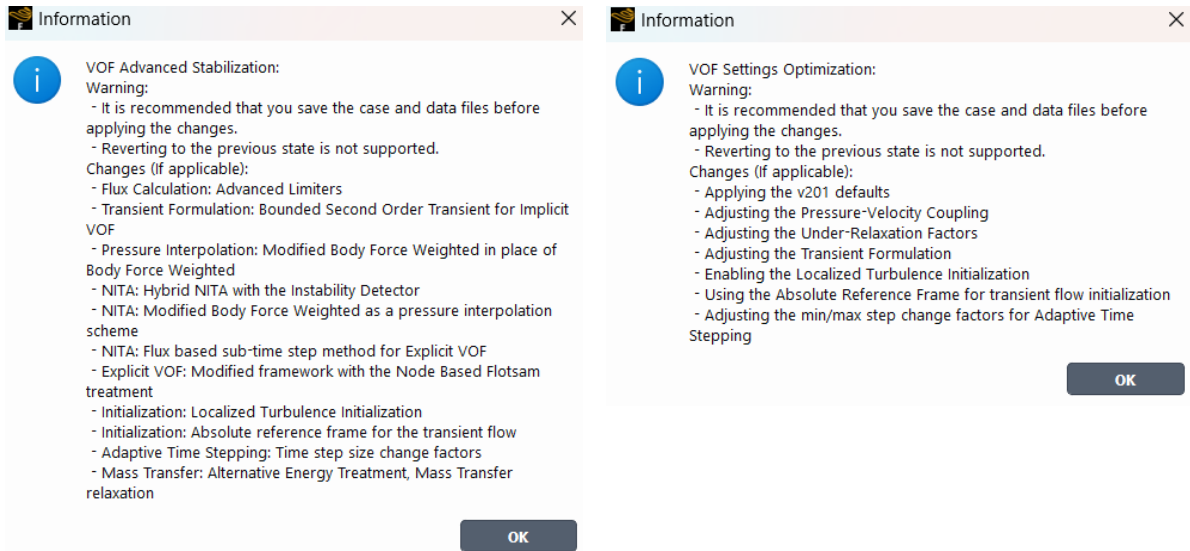
Appendix 2: Manual setup of 3D "butterfly" mesh on a symmetric 3D halftube

Appendix 3: Results of the 2D simulation with $\omega = 0 \frac{\text{rad}}{\text{s}}$ at Δt_s =3e-5s before divergence using the CICSAM Scheme
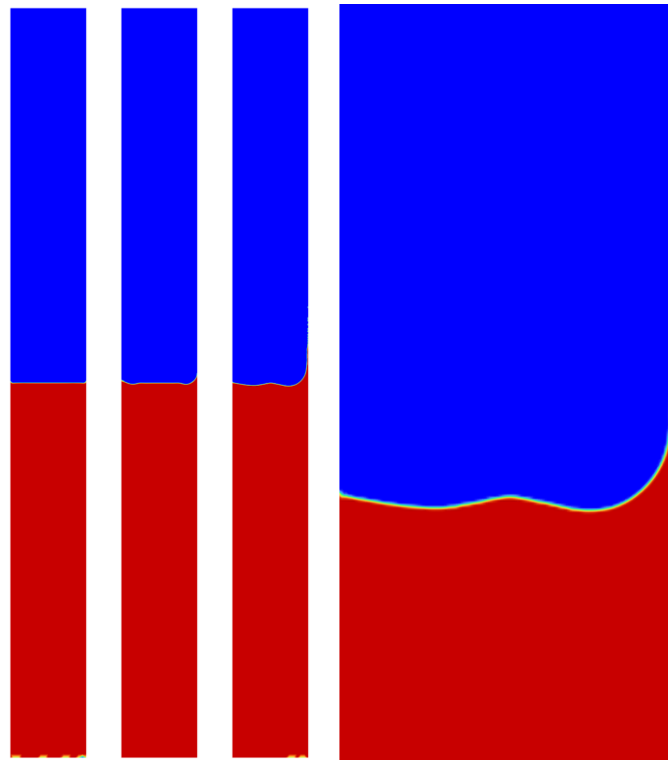
Appendix 4: Evolution of the interface with the capillary tube spinning at $\omega = 7000\text{rad/s}$ in positive z-direction to show that Fluent does indeed consider the rotation somehow

no optimization   with optimization   optimization + velocity
                                                     limiting to 50 m/s
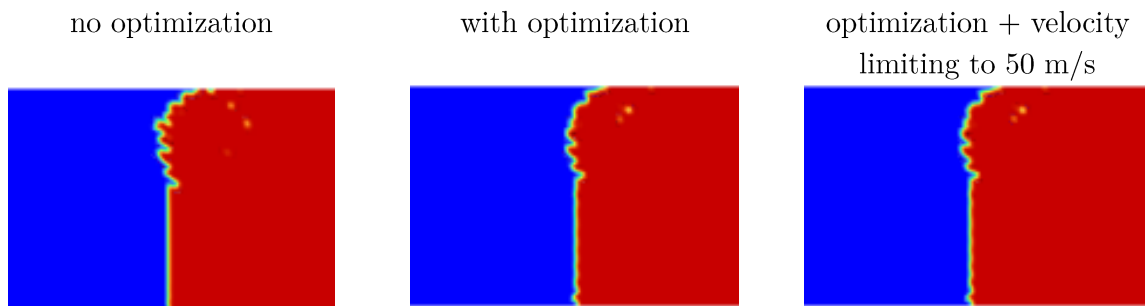
Appendix 5: Comparison of different mechanisms to counter divergence at t=3e-4s

ii.   Appendix B

Fluent TUI Command to set the macro outputting the volume fractions at each tenth time step for a given line: "**plot plot y vof-%t y n n air-phase vof yes 0 1 14 13 12 6 9 8 7 10 11 ()**"

Appendix 6: Example code for the automation of the post-processing of the macro results

```matlab
%% INITIAL VALUES

first_timestep= 6990;
last_timestep = 11470;
length_vof_vector=504;
offset=1.25029014265984;

%% EXCEL

% !!! CHANGE RANGE
data_water=readmatrix('reports_pp.xlsx','Sheet','water_report','Range','A5:R4497');
% !!!
time_water_full=data_water(:,4);
time_water_range= time_water_full(1:10:end);
time_water_range_set= time_water_range-offset;


%% DATA ELABORATION

for this_x = first_timestep:10:last_timestep

  this_file=sprintf('vof-%04d', this_x);
allData = readmatrix(this_file);
numbers = allData(1:length_vof_vector,:);
x=numbers(:,1);
vof=numbers(:,2);

 if isempty(find(vof>=0.5, 1, 'first'))
        I(this_x) = length_vof_vector;
 else
I(this_x) = find(vof>=0.5, 1, 'first');
    end
R(this_x) = x(I(this_x));

end

positions= first_timestep:10:last_timestep;
R_real=R(positions);

%% PLOT

figure(1)
plot(time_water_range_set(1:length(R_real)),R_real);
xlabel('time [s]','Interpreter','latex')
ylabel('Maximum radial extension [m]','Interpreter','latex')
ylim([0, 0.022]);
yline(0.02,'--','End of glass plate','Interpreter','latex')
```
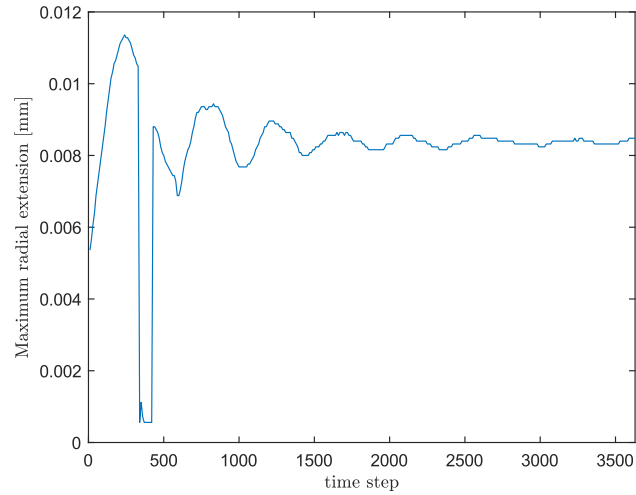
Appendix 7: Initial profile determination of Ethanol
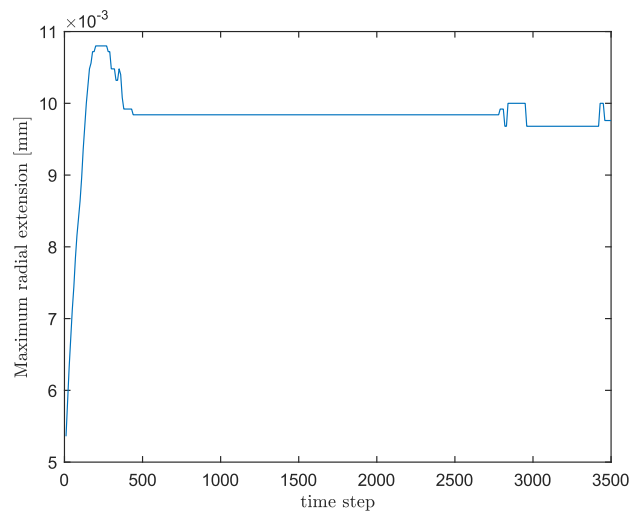
Appendix 8: Initial profile determination of Oil

Appendix 9: Sessile droplet has a $Bo_r = 1500$ compared to the $Bo_r = 580$ of the other cases

Even with the almost three times as high Bo_r the substrate edge is reached considerably later and is connected to a lot of fingering instability from early on.

3. Literature

[1] F. Cruz Mazo, *Internal Comunication,* Madrid, 2024.

[2] ANSYS, "Ansys Fluent Theory Guide," ANSYS, Inc., Canonsburg, PA, 2022.
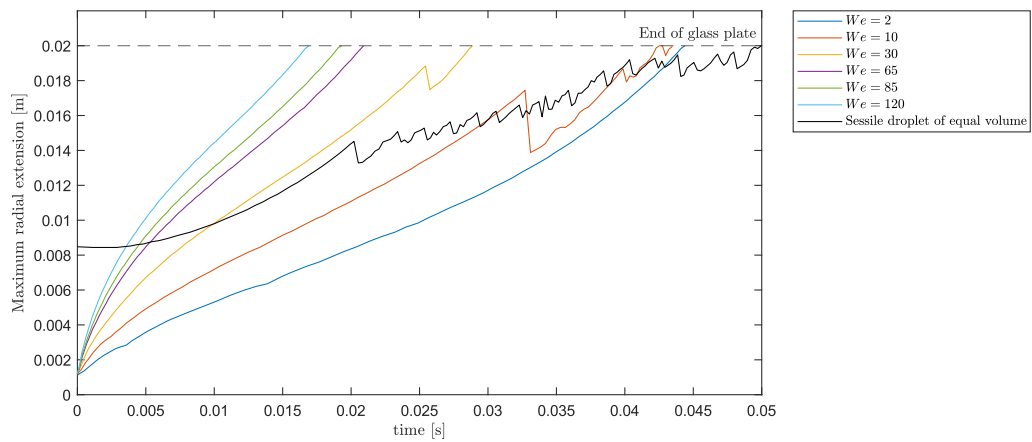
[3] ANSYS, "Ansys Fluent User's Guide," ANSYS Inc., Canonsburg, PA, 2022.

[4] R. Helmig and H. Class, "Fluidmechanik II," Institut fur Wasser- und Umweltsystemmodellierung, Stuttgart, 2021.

[5] Ansys Inc., "Ansys," September 2020. [Online]. Available: https://innovationspace.ansys.com/courses/wp-content/uploads/sites/5/2020/09/Basics-of-Turbulent-Flows-Lesson-5-Handout.pdf. [Accessed 21 6 2024].

[6] D. L. Youngs, "Time-Dependent Multi-Material Flow with Large Fluid Distortion," in *Numerical Methods for Fluid Dynamics*, Reading (UK), 1982.

[7] R. Courant, K. Friedrichs and H. Lewy, "Über die partiellen Differenzengleichungen der mathematischen Physik," *Mathematische Annalen,* vol. 100, 1928.

[8] S. Dahua, Y. Lin and F. Jintu, "The fastest capillary flow under gravity," *Appl. Phys. Lett. 9,* p. 104, June 2014.

[9] E. W. Washburn, "The dynamics of capillary flow," *Physical review 17.3,* 1921.

[10] D. W. Green and R. H. Perry, Perry's Chemical Engineers Handbook, McGraw-Hill, 2008.

[11] N. Vargaftik, B. Volkov and L. Voljak, "International tables of the surface tension of water," *J. Phys. Chem. Ref. Data 12,* pp. p. 817-820, 1983.

[12] J. R. Thome and A. Cioncolini, "Chapter Four - Flow Boiling in Microchannels," in *Advances in Heat Transfer*, 2017, pp. 157-244.

[13] Dharamendra and M. K. Awasthi, "Temporal instability of Walter's B viscoelastic fluid film," *Journal of Physics: Conference series,* 2021.

[14] B. Derby, "Inkjet Printing of Functional and Structural Materials: Fluid Property Requirements, Feature Stability, and Resolution," *Annual review of materials research,* 2010.

[15] L. Mösch, "Multiphase VOF simulation of a rotating capillary tube," https://innovationspace.ansys.com/forum/forums/topic/multiphase-vof-simulation-of-a-rotating-capillary-tube/#post-370986, Madrid, 2024.

[16] V. Hernandez-Perez, M. Abdulkadir and B. J. Azzopardi, "Grid generation issue in the CFD modelling of two-phase flow in a pipe," *Journal of computational multiphase flows,* p. 14, 2017.

[17] D. Arabali and F. Peters, "Interfacial tension between oil and water measured with a modified contour method," *Colloids and Surfaces A: Physiochem. Eng. Aspects 426,* vol. 3, 2013.

[18] F.-C. Chou and K.-H. Huang, "Reduction of Amount of Dye during Spin Coating," *Japanese Journal of Applied Physics,* no. 45, 2006.

[19] G. H. McKinley, "Dimensionless Groups For Understanding Free Sruface Flows of Complex Fluids," *SOR Rehology Bulletin,* 2005.

[20] P. Yuming, W. Zhibei, Z. Xinyan, D. Weiwei and X. Huihui, "On axisymmetric dynamic spin coating with a single drop of ethanol," *Journal on Fluid Mechanics,* vol. 951, 2022.

[21] M.-W. Wang and F.-C. Chou, "Fingering Instability and Maximum Radius at High Rotational Bond Number," *Journal of The Electrochemical Society,* no. 148, 2001.

[22] H. Guo, Kaoping Song and R. Hilfer, "A Brief Review of Capillary Number and its Use in Capillary Desaturation Curves," *Transport in Porous Media,* no. 144, pp. 3-31, 2022.

[23] W. Ohnesorge, "Die Bildung von Tropfen an Düsen und die Auflösung flüssiger Strahlen," *Zeitschrift für Angewandte Mathematik und Mechanik,* no. 16, pp. 355-358, 1936.

[24] M. Hoorfar and A. W. Neumann, "Recent Progress in Axisymmetric Drop Shape Analysis (ADSA)," *Advances in Colloid and Interface Science,* no. 121, pp. 25-49, 2006.

[25] R. V. Zucker, "Capillary-Driven Shape Evolution in Solid-State Micro- and Nano-Scale Systems," June 2015. [Online]. Available: https://dspace.mit.edu/handle/1721.1/98575?show=full. [Accessed August 2024].

[26] U. o. Louisville, "University of Louisville," [Online]. Available: https://louisville.edu/micronano/files/documents/standard-operating-procedures/SpinTheory.pdf. [Accessed August 2024].

[27] A. Öztekin, D. E. Bornside, A. B. Robert and P. K. Seidel, "The connection between hydrodynamic stability of gas flow in spin coating and coated film uniformity," *Journal of Applied Physics,* no. 77, 1995.

[28] T. Gambarayan-Roisman and V. Starov, "Editorial overview: recent progress in studies of complex wetting and spreading phenomena," *Current opinion in colloid & interface science,* 2021.

[29] A. Marmur, "Surface tension of an ideal solid: What does it mean?," *Current Opinion in Colloid & Interface Science,* 2021.

[30] A. Marmur and D. Valal, "Correlating interfacial tensions with surface tensions: a Gibbsian approach," *Langmuir,* pp. 5568-5575, 2010.

[31] H. Mohsin, U. Sultan, Y. Joya and S. Ahmed, "Development and characterization of cobalt based nanostructured super hydrophobic coating," *IOP Conf. Ser.: Mater. Sci. Eng.,* 2013.

[32] M. Sahid, P. Götze, D. Kessel and W. Dornow, "Adsorption of crude oil colloids on glass plates: measurements of contact angles and the factors influencing glass surface properties," *Colloids and Surfaces A: Physiochemical and Engineering Aspects,* pp. 25-32, 1996.

[33] M. Miyama, Y. Yang, T. Yasuda, T. Okuno and H. Yasuka, "Static and Dynamic Contact Angles of Water on Polymeric Surfaces," *Langmuir,* no. 13, pp. 5494-5503, 1997.

[34] R. K. Dwivedi, J. Vandana and R. Muralidhar, "Dynamic contact angle model for resolving low-viscosity droplet oscillations during spreading over a surface with varying wettability," *Physical Review Fluids,* no. 7, 2022.

[35] G. Taylor, "Disintegration of Water Droplets in an Electric Field," *Proceedings of the Royal Society,* no. 280, pp. 383-397, 1964.

[36] F. Melo, S. Suave and J. F. Joanny, "Fingering instability of spinning drops," vol. 63, no. 1958, 1989.

[37] H. R. Pruppacher and R. L. Pitter, "A Semi-Empirical Determination of the Shape of Cloud and Rain Drops," *Journal of the Atmospheric Sciences,* no. 28, pp. 86-94, 1970.

The adopted citation scheme is the one proposed by the IEEE.

Declaration of Academic Integrity

I hereby declare that I have written this work independently and have not used any sources other than those indicated. All statements that are quoted or paraphrased from other works are clearly marked as such. The submitted work has neither been fully nor substantially part of any other examination process and has not been published, either in whole or in part.

Furthermore, I assure that the electronic version is consistent with the physical copy.

Madrid, September 26th, 2024